



**JIMMA UNIVERSITY
INSTITUTE OF TECHNOLOGY
FACULTY OF MECHANICAL ENGINEERING**

**DESIGN AND PERFORMANCE ANALYSIS OF SOLAR TUNNEL
DRYER FOR CHARCOAL DUST BRIQUETTE OF VERDE AFRICA
Lda. IN MOZAMBIQUE**

*A thesis submitted to the School of Graduate Studies of Jimma University Institute
of Technology in partial fulfillment for the Degree of Masters of Science in
Sustainable Energy Engineering*

By: Fauzia Argentina Guibunda

Advisor: Prof. Dr. A. Venkata Ramayya (Ph.D.)

Co-Advisor: Getachew Shunki Tibba (Dr.-Ing.)

Dec, 2021

Jimma,

Ethiopia

CERTIFICATION

I, the undersigned, certify that I read and hear by recommending for acceptance by Jimma University Institute of Technology Mechanical Engineering Facility, a thesis entitled “Design and Performance Analysis of Solar Tunnel Dryer for Charcoal Dust Briquette of Verde Africa Lda in Mozambique.” This certificate is used as in partial fulfillment of the requirements for the degree of Masters of Science in Sustainable Energy Engineering.

Signature: _____

Signature: 

Date: _____

Date: _____

Prof. Dr. A. Venkata Ramayya (Ph.D.)
(Main Supervisor)

Dr.-Ing. Getachew Shunki Tibba
(Co-Supervisor)

DECLARATION

I, Fauzia Argentina Guibunda, First, I declare that this thesis is the result of my work and that all sources or materials used for this thesis have been duly acknowledged. This thesis is submitted in partial fulfillment of the requirements for a Master's Degree in Sustainable Energy Engineering at Jimma Institute of Technology and to be made available at the University's Library under the rule of the Library. I confidently declare that this thesis has not been submitted to any other institutions anywhere for the award of any academic degree, diploma, or certificate.

Signature: _____

Date: _____

Fauzia Argentina Guibunda



Jimma University

Jimma Institute of Technology

Faculty of Mechanical Engineering

**Design and Performance Analysis of Solar Tunnel Dryer for Charcoal Dust
Briquette of Verde Africa Lda in Mozambique**

By: Fauzia Argentina Guibunda

Approved by Board of Examiners

_____	_____	_____
(Advisor)	Signature	Date
_____	_____	_____
(Internal Examiner)	Signature	Date
_____	_____	_____
(External Examiner)	Signature	Date
_____	_____	_____
(Chairman)	Signature	Date

ACKNOWLEDGMENT

First of all, I give thanks saying “Muito obrigada” to Almighty God for the protection and straights to stand and continue.

I am so thankful to the **MOUNAF Project** (Mobilité Universitaire en Afrique) under the Intra Africa Academic Mobility Scheme scholarship and the Faculty of Mechanical Engineering at Jimma University – Ethiopia for making it possible to accomplish this degree. I give profound appreciation to the Professors and lecturers at the Sustainable Energy Engineering program, the librarians, and other workers of the faculty. My distinct and heartily thanks go to my Supervisor, Prof. Dr. **Venkata Ramayya** who encouraged and directed me throughout my stay at the University. His daily challenges brought this project towards completion. Furthermore, I am glad to acknowledge Eduardo Mondlane University in Mozambique - Maputo (Cooperation Office) for linking me with this Academic Mobility to pursue my studies in Ethiopia.

Lastly but not least, I would like to thank my family who encouraged and prayed for me throughout the time of my research. This Master Thesis is heartily dedicated to my Mum **Teresinha Pascoal** who made everything possible and impossible to see this dream come true.

TABLE OF CONTENTS

CERTIFICATION	i
DECLARATION	ii
ACKNOWLEDGMENT.....	iv
LIST OF FIGURES	viii
LIST OF TABLES.....	x
ABBREVIATION.....	xi
NOMENCLATURE	xii
ABSTRACT.....	xv
CHAPTER 1	1
INTRODUCTION	1
1.1 Statement of the Problem	2
1.2 Research Gap.....	3
1.3 Objectives of the Study	5
1.4 Scope of the Study.....	5
1.5 Beneficiaries and Impacts	5
1.6 Description of the Study Area.....	6
CHAPTER 2	8
LITERATURE REVIEW	8
2.1 Solar Energy Potential of Mozambique	8
2.2 Solar Briquette Drying Technology	9
2.3 Effect of Drying on Briquette Quality.....	10
2.4 Types of Solar Dryers	11
2.5 Drying Theory	14
2.6 Factors Affecting the Rate of Drying the Briquettes.....	16
2.7 Computational Fluid Dynamics in Solar Drying Systems	18
2.8 Previous Studies on Solar Tunnel Greenhouse Dryer.....	19
CHAPTER 3	21
SOLAR DRYING SYSTEM DESIGN	21
3.1 Main Systems of SDS	21
3.2 Working Principle of SDS.....	22
3.3 Material Selection	24
3.4 Design Criteria and Assumptions.....	25
3.5 Solar Tunnel Drier Design	26

3.6 Area Optimization of Solar Tunnel Dryer.....	31
3.7 Psychometric Analysis of Drying Chamber.....	36
3.8 Estimation of Air Mass Flow Rate.....	40
3.9 Useful Energy Output.....	42
3.10 Description of the Drying Chamber.....	43
3.11 Design Dimensions.....	47
CHAPTER 4.....	49
MATHEMATICAL MODELING AND ANSYS SIMULATION.....	49
Part 1: Mathematical Modeling of SAH.....	49
4.1.1 Energy Balance of Glass Cover.....	49
4.1.2 Energy Balance on Absorber Plate.....	50
4.1.3 Energy Balance on Air Stream.....	51
4.1.4 The Heat Transfer Correlations.....	52
4.1.5 Useful Energy Output of SAH.....	55
4.1.6 Collection Efficiency of SAH.....	55
Part 2: ANSYS Fluent Simulation of STD.....	55
4.2.1 Geometry Creation.....	55
4.2.2 Meshing.....	57
4.2.3 Analysis Setup.....	59
4.2.4 Solution Method.....	62
CHAPTER 5.....	63
RESULT DISCUSSION.....	63
Part 1: Solar Radiation and Ambient Temperature.....	63
5.1.1 Ambient Temperature.....	63
5.1.2 Estimated Hourly Solar Radiation.....	64
Part 2: Result of MatLab Simulation of SAH.....	65
5.2.1 Hourly Temperature Variation.....	66
5.2.2 Hourly Variation of Useful Energy Output.....	67
5.2.3 Hourly Variation of Thermal Efficiency.....	68
Part 3: Result of ANSYS Fluent Simulation of STD.....	69
5.3.1 Simulation Result of Model 1.....	69
5.3.2 Simulation Result of Model 2.....	78
5.3.3 Simulation Result of Model 3.....	82

CHAPTER 6	85
CONCLUSION AND RECOMMENDATION	85
6.1 Conclusion	85
6.2 Recommendation	86
REFERENCE	87
APPENDIX	91
ANNEX A: MATLAB PROGRAM CODE	91
ANNEX B: PROPERTIES OF VARIOUS MATERIALS	95
ANNEX C: VERDE AFRICA Lda BRIQUETTE PRODUCT	97
ANNEX D: PSYCHROMETRIC CHART	97

LIST OF FIGURES

Figure 1.1: Location of Mozambique (B) on the African continent (A)	6
Figure 2.1. Monthly averages of insolation kWh/(m ² day) in Tanzania and Mozambique derived from interpolation of SSE data.	8
Figure 2.2: Drying briquette under the sun in Mozambique.....	10
Figure 2.3: Classification of dryer and drying mode.	12
Figure 2.4: Illustration of a drying schedule.....	15
Figure 2.5: Effect of airflow rate on drying time of moist agricultural products	17
Figure 3.1: Schematic Diagram of Overall Solar Drying System	21
Figure 3.2: Schematic Diagram of Working Principle of STD	23
Figure 3.3: Front View of Selected Solar Tunnel Dryer.....	31
Figure 3.4: Face Surface of STD (Front View)	33
Figure 3.5: The Size of Charcoal Briquette of Verde Africa LDA.....	35
Figure 3.6: A Schematic Diagram of Drying Chamber with each Process involved	37
Figure 3.7: Psychrometric Chart of Adiabatic Humidification.....	38
Figure 3.8: Psychrometric Chart of Non-Adiabatic Humidification	39
Figure 3.9: Schematic Diagram of Energy Balance of STD.....	41
Figure 3.10: Schematic Diagram of the Designed Drying Chamber.....	43
Figure 3.11: (a) Model Diagram of Drying Bed and (b) Layout of Drying Bed	45
Figure 3.12: Arrangement of Charcoal Briquette	46
Figure 4.1: Heat Energy Balance of Glass Cover.....	49
Figure 4.2: Heat Energy Balance of Absorber Plate.....	50
Figure 4.3: Energy balance of the working fluid in flat-plate solar collector.....	51
Figure 4.4: Thermal Resistance Networks of a Flat-Plate Collector	52
Figure 4.5: Model of the Drying Chamber	56
Figure 4.6: Meshing of Model 1	57
Figure 4.7: Meshing of Model 3	58
Figure 4.8: Meshing of Model 3	59
Figure 5.1: Hourly Ambient Temperature Variation	64
Figure 5.2: Hourly Global Radiation Variation	65

Figure 5.3: Hourly Global Radiation Variation	66
Figure 5.4: Hourly Variation of Useful Energy Gain	67
Figure 5.5: Hourly Variation of Thermal Efficiency of SAH.....	68
Figure 5.6: Hourly Variation of Outlet Air Temperature	70
Figure 5.7: Hourly Temperature Variation of Air	71
Figure 5.8: Simulation Result of Temperature on <i>a) November 14</i> and <i>b) June 11</i>	72
Figure 5.9: Graph of Temperature Variation inside STD on November 14	73
Figure 5.10: Contour Profile of (a) Velocity and (b) Pressure	74
Figure 5.11: Velocity Streamline of Model 1	75
Figure 5.12: Velocity Vector of Model 1	76
Figure 5.13: Hourly Variation of Useful Energy Gain of STD	77
Figure 5.14: Hourly Variation of Thermal Efficiency of STD	78
Figure 5.15: Temperature Profile of (a) Briquette Wall and (b, c and d) Drying Chamber	79
Figure 5.16: Temperature distribution on the Surface of Briquette Wall.....	80
Figure 5.17: Contour Profile of (a) Velocity and (b) Pressure	81
Figure 5.18: Velocity Streamline and Vector of Model 2	81
Figure 5.19: Temperature Contour of a) Model 3 and b) Front, c) Middle and d) Back Rows...	83
Figure 5.20: Temperature Contour on Upper Front Row of Briquette	83
Figure 5.21: Velocity Vector of Model 3	83
Figure (C-1): Charcoal Duct Briquette of Verde Africa Lda	97
Figure (D-1): Psychrometric Chart	97

LIST OF TABLES

Table 1.1: Solar Drying Technology and their Study Outcome	4
Table 2.1: Classification, advantages and disadvantages of the four types of solar driers	13
Table 3.1: Design Conditions and Assumptions.....	25
Table 3.2: Summary of Weight and Moisture Content Analysis	29
Table 3.3: Dimension Specification of Verde Africa LDA	34
Table 3.4: Summary of Design Dimensions	47
Table 4.1: Final Dimension of Drying Chamber and Drying Product.....	57
Table 4.2: The Summary of Operating Conditions.....	60
Table 4.3: Summary of Boundary Conditions	61
Table 4.4: The Type of Scheme, Gradient and Initialization of each Model.....	62
Table 5.1: Hot Air Inlet Temperature and Diffuse Radiation on November 14	69
Table (B-1): Thermal Conductivities of Absorber Materials.....	95
Table (B-2): Properties of Cover Materials	95
Table (B-3): Properties of Sealing Materials	95
Table (B-4): Properties of Insulation Materials	96
Table (B-5): Lists Properties of Some Selective Coatings	96

ABBREVIATION

AM	Anti-Meridian
CDB	Charcoal Dust Briquette
CFD	Computational Fluid Dynamics
CV	Control Volume
DBT	Dry Bulb Temperature
DO	Discrete Ordinate
E	East
GMT	Greenwich Mean Time
Lda	Limitada (Portuguese)
NACA	National Advisory Committee for Aeronautics
N	North
PM	Anti-Meridian
PV	Photovoltaic
RH	Relative Humidity
RTE	Radiative Transfer Equation
S	South
SAH	Solar Air Heater
SDS	Solar Drying System
SSA	Sub-Saharan Africa
SSE	Solar Energy Estimations
STD	Solar Tunnel Dryer
UV	Ultra Violet
Vs	Verses
W	West
WBT	Wet Bulb Temperature

NOMENCLATURE

Notations

A_{bt}	Top Surface Area of Briquette
A_c	Collector Area
A_{floor}	Floor Area
A_{fs}	Face Surface Area
A_{fsb}	Face Surface Area of Briquette
A_{hsb}	Circular-Hole Surface Area of Briquette
A_{lsb}	Lateral Surface Area of Briquette
A_{osb}	Overall Outer Surface Area of Briquette
C_{pa}	Specific Heat of Air
C_{pb}	Specific Heat of Briquette
C_{pw}	Specific Heat of Water
d_c	Collector Diameter
D_{hl}	Hole Diameter
h	Convective Heat Transfer Coefficient
h_{fg}	Latent Heat of Vaporization of Water
I	Solar Insolation
L_b	Length of Briquette
L_{cs}	Length of Collector Surface
$M_{f,db}$	Final Moisture Content in Dry Base
$M_{f,wb}$	Final Moisture Content in Wet Base
$M_{i,db}$	Initial Moisture Content in Dry Base
$M_{i,wb}$	Initial Moisture Content in Wet Base
$M_{r,db}$	Removed Moisture Content in Dry Base
$M_{r,wb}$	Removed Moisture Content in Wet Base
\dot{m}_a	Air Mass Flow Rate
m_{bf}	Final Mass of Briquette
m_{bi}	Initial Mass of Briquette
\dot{m}_f	Constant Drying Rate

m_s	Mass of Solid Briquette
m_{wf}	Final Mass of Water
m_{wi}	Initial Mass of Water
m_{wr}	Mass of Water to be Removed
\dot{m}_{wv}	Water Vapor Mass Flow Rate
n_t	Total Number of Briquette
$Q_{l,w}$	Latent Heat of Water
\dot{Q}_r	Rate of Thermal Energy Required
$Q_{s,b}$	Sensible Heat of Briquette
$Q_{s,w}$	Sensible Heat of Water
Q_t	Total Amount of Heat Required
T_b	Final Temperature of Briquette
T_{bi}	Initial Temperature of Briquette
T_f	Final Temperature
T_i	Initial Temperature
T_w	Final Temperature of Water
T_{wi}	Initial Temperature of Water
t_d	Drying Time
W_b	Width of Briquette
W_{cs}	Width of Collector Surface
w	Specific Humidity

Greek Symbols

ε	Emissivity
α	Absorptivity
τ	Transitivity
η	Efficiency
π	Pi
μ	Dynamic Viscosity
ϑ	Kinematic Viscosity
σ	Steven Boltzmann Constant

Units

$^{\circ}\text{C}$	Degree Celsius
h	Hour
J	Joule
K	Kelvin
K_g	Kilogram
KJ	Kilo Joule
KWh	Kilo Watt Hour
m	Meter
min	Minute
cm	Centimeter
MWh	Mega Watt Hour
P_a	Pascal
s	Second
W	Watt

ABSTRACT

In Mozambique, the attraction toward biomass briquette production is highly enhanced due to the increment of energy demand in the country and the high cost of charcoal and firewood with their high environmental, health, and economic impact. Among briquette production processes, drying is the most energy-intensive, where moisture content is reduced from 50% up to 10%. In the country, briquette producers use the open sun drying technique which takes 5 to 7 days depending on the weather condition. Accordingly, the proposed system intended to answer these drying problems through the Design and Performance Analysis of Solar Tunnel Dryer for Charcoal Dust Briquette of Verde Africa Lda factory.

The proposed model includes a solar tunnel greenhouse dryer (STD) as a drying chamber and a solar air heater (SAH) as an additional heat source. The design and size optimization of the chamber was done based on the total amount of daily production, the quantity of water to be removed, drying period, the thermal energy required, available solar radiation, and operating temperature. SAH was selected based on the analysis of numerical modeling, to observe temperature variation of the air at the collector exit, which was used as an input parameter for the chamber. A 3D Computational Fluid Dynamics (CFD) analysis of unloaded and 2 loaded models of STD had been performed based on heat transfer analysis and radiation model to study the uniform distribution of temperature inside the chamber.

It was found that the overall size of the drying chamber is $17.5\text{ m} \times 4\text{ m} \times 2\text{ m}$ and the surface area of the SAH collector is 10 m^2 . Hot air flowing through the outlet of SAH at 1.3572 Kg/s and an average of 58.8°C had been provided at the inlet of STD to heat the air stream and briquette in the chamber. The daily average thermal efficiency of the drying system is 47.54%. The average temperature of the air inside the chamber is above 50°C around 6 hours of the day and uniformly distributed except June and July which are below 50°C throughout the day. The value of daily total useful energy received from the drying air is greater than the amount of thermal energy required for the drying process, from this it can be concluded that one batch of briquette can dry within one day. Compared to the open sun drying method the drying period will reduce from 5 to 1 day using the proposed solar tunnel dryer.

Keywords: Solar energy; Solar drying; Biomass briquette; Greenhouse solar tunnel dryer.

CHAPTER 1

INTRODUCTION

In rural areas of Sub-Saharan Africa (SSA), solid bioenergy is still the main source of energy for cooking and heating for more than 90 % of the population, or around 3 billion people [1, 3]. In developing countries like Mozambique, access to modern energy services remains very low, with around 80% of the population depending completely on traditional biomass to meet their energy demand, making it worse, these materials are used inadequately in their raw form, thus wasting much of the energy available and contributing to the unhealthy environment [2].

Each year, around 1.6 million people globally, of which 400,000 are from Sub-Saharan Africa, die prematurely, mostly women and children due to the exposure to indoor air pollution from wood fuel combustion [3]. The contaminants emitted reduce the quality of the air, causing numerous illnesses related to the inhalation of smoke from solid fuels, such as higher blood pressure, serious respiratory infections, cataracts, blindness, adverse effects on pregnancy, low birth weight, infant mortality and, particularly, chronic obstructive pulmonary diseases [4,5]. In addition to that, valuable time and efforts are expended during the day walking very long distances on fuel collection which leads to deforestation.

Many developing countries such as Nairobi (Kenya), Kigali (Rwanda), and Tanga (Tanzania), have been successfully applying various innovative briquette technologies to produce and distribute renewable bioenergy, from agriculture, forestry, industry, and pastoral waste promoting the sustainable use of these locally available resources to meet the growing energy demand without exposing the environment [6]. Briquetting is considered the process of converting low bulk density biomass into high density and energy concentrated fuel. Despite clear benefits of charcoal made through briquetting that comprise low price, long burning time compared to conventional charcoal, improve health problems, environmental sustainability and potential for product standardization, their acceptance as a substitute for wood charcoal in SSA remain very limited.

In Mozambique for instance the awareness of biomass briquette production and consumption is very low compared to other eastern and southern African countries. However, the opportunities of briquettes production are very high due to the large potential of biomass resources, higher charcoal demand in and around the cities, the favorable policy of the country toward sustainable biomass

energy production, lower production capacity because of the number of producers are very few and the effects of firewood and charcoal production as well as consumption [7,8]. Currently, there are few briquette producers in the country with lower production capacity (20t per month). In general, the reliance on the importation of machines and spare parts limits the scale at which briquette production can happen and, to a large scope explains the reasons for few large-scales briquette factories in the region [6, 7].

Apart from the difficulties on factory installation, drying space appears to be the shared challenge for all briquette producers not only around Mozambique but other Sub-Saharan African countries [6]. All producers mention insufficiency of drying space and difficulty with drying in the rainy season as factories limiting the scale and regularity of production to answer the demand of their customers. Applying drying technology to densified biomass is advisable to use solar energy to sustain low production costs and carbon neutrality of this renewable fuel source [9]. Bhattacharya states that biomass briquette is more costly than wood and this contributes to the reduced acceptance of biomass as an alternative fuel source, particularly in developing countries [10].

Accordingly, this work intended to design a solar tunnel dryer to dry the charcoal dust briquette of the Verde Africa Lda factory in Mozambique. To achieve this general goal and meet the drying requirements of the biomass fuel briquette, size optimization of the dryer, numerical analysis of SAH will be done, determining the hourly variation of air temperature at the outlet of the collector. Finally, simulation of heat transfer and flow distribution of the drying air inside STD to evaluate the changes of the operating parameters inside the chamber.

1.1 Statement of the Problem

The drying process is one of the most energy-intensive procedures and accounts for around 70% of the total energy used in the biomass densification process. The produced charcoal briquettes before drying have a moisture content of 50 % immediately after pressing. The moisture content of charcoal briquettes is a quality feature and influences directly the customer's decision to buy. If the moisture content is above 10 %, the charcoal briquettes burn slower and lighting up takes longer, which implies poor quality to the customers. In Mozambique briquette producers, to achieve these recommended levels of moisture for combustion, the companies spread the wet briquettes directly under the sun. This process takes from 4 days under sunny weather conditions

and up to 7 days during rainy seasons, apart from this it requires large spaces to accommodate the briquettes.

In short, all briquette producers in the country cite scarcity of drying space and difficulties with drying in the rainy season as factors limiting the scale and consistency of production. Furthermore, besides the lower radiation, movements to protect the briquettes from the rain increase the drying time. These movements also cause an increased number of broken briquettes which have to be recycled again. It makes the drying process also labor intensive because the whole production has to be moved or covered morning, every evening (due to humidity) before and after every rain pour.

These aspects limit the production output to very low levels due to dependency on weather conditions resulting in an even higher financial loss because fixed costs still have to be covered, making charcoal briquette not affordable alternative renewable energy for the conventional charcoal and firewood. To overcome these challenges is now being proposed to design and simulate a solar tunnel dryer for biomass fuel briquette under Mozambique climatic conditions.

1.2 Research Gap

According to the literature, around Sub-Saharan Africa (SSA) all fuel briquette producers mention the shortage of drying space and difficulties with drying in the rainy season as causes limiting the scale and consistency of production [6, 9, 11, 12]. And Mozambique is one among these countries, that briquette factories are totally dependent on weather conditions to reduce the moisture content of the wet briquette after production. Few researches were conducted on drying briquette technologies using solar tunnel dryers, most of the papers focus on preservation, improvising the lifespan and quality of the agricultural products. The table 1.1 below shows briefly some examples of articles highlighting the performance of solar tunnel dryers to reduce the moisture content of cultivated crops.

Furthermore, Monish *et al.*, [13] prepared a review on solar tunnel air dryer, the author investigated the flow path design with the temperature distribution. According to the review, a computational fluid dynamics (CFD) analysis had been performed to study the distribution of temperature at the outlets of the pipeline using the ANSYS-Fluent v16. 2.

Table 1.1: Solar Drying Technology and their Study Outcome

Solar Drying Technology and their Study Outcome		
Drying Technology	Raw Material	Study Outcome
Solar Tunnel	Copra	Reduced drying time from 5-7 days to 2 days with improved quality of copra [14].
Solar Tunnel	Crops	Better performance under low moisture content [15].
Solar Tunnel	Coconuts	Moisture was reduced from 53.84% to 7.4% in 56 hours – open sun could take 147 hours [16].
Solar Tunnel	Silkworm pupae	Moisture content was reduced from 3.70 kg to 0.20kg in 570 min, drying time was not only dependent on the flow rate but also on drying air temperature [17].
Solar Tunnel	Tomatoes	Moisture content of sliced tomatoes was reduced from 94.09% to 20.50% on dry basis over a period of 15 hours [18].
Cabinet	Biomass briquette	Found that 13 kg of water was removed from 420 briquettes over 16 hours of sunlight [9].
Solar Tunnel	Tomato	The result showed a considerable decrease in drying rate and higher moisture diffusivity than open sun drying [56].
Solar Tunnel	Ginger	The active drying mode with and without sensible heat storage has the fastest moisture removal rate than passive drying [57].

A comparative CFD analysis for the conventional and the proposed new pipeline configuration by the application of both convection and radiation heat transfer modelling had been done. The result of Monish *et al.*, [13] found that the proposed new pipeline configuration reduced the drop in temperature across the pipeline so that the hot air existing at every outlet has a fairly uniform temperature whose magnitude is close to that of the inlet temperature. However, these simulation does not incorporate the type of crop or any other kind of product with moisture content for a specific geographical conditions.

It is now being proposed to apply the designed new configuration which reduced the variation in temperature across the tunnel dryer on Monish *et al.*, [13] research, to simulate the drying process for biomass briquettes produced in one factory (*Verde Africa Lda*) located in Southern East part Africa – Mozambique, using briquettes made of charcoal dust as raw material under similar model.

1.3 Objectives of the Study

1.3.1 General Objective

The general objective of this research is designing and performance analysis of a solar tunnel dryer for low temperature regions system to dry charcoal dust briquette production of Verde Africa Company based on Mozambique weather conditions.

1.3.2 Specific Objective

To achieve the general objective of this project the following specific objectives are performed:

- i.* To design and size optimization of solar tunnel dryer to meet the drying requirements of the biomass fuel briquette.
- ii.* To simulate numerical analysis of solar air heater to determine the hourly variation of air temperature at the outlet of the collector using MatLab programming software.
- iii.* To perform simulation of heat transfer and flow parameters distribution of drying air inside solar tunnel dryer based on discrete ordinate (DO) radiation model on ANSYS-Fluent software.

1.4 Scope of the Study

The study focus on the design and simulation of a solar tunnel drier system for low temperature hot air supply to dry wet biomass charcoal dust briquette of Verde Africa Factory, under Maputo-Mozambique weather conditions. The work tries to find an appropriate design configuration which reduce the variation in temperature across the tunnel drier and meet the required air temperature to dry the briquette. To achieve this goals it was considered only the heat transfer analysis to observe the distribution of drying air parameters inside the solar tunnel dryer. Solar air heater was included in the system to increase the inlet air temperature of the proposed dryer design.

1.5 Beneficiaries and Impacts

Different benefits can be accommodated from this project with the perspectives of clean and affordable energy, health, agriculture, socio-economic development and environment. After manufacturing the proper design of a low cost solar tunnel dryer for biomass briquette suitable for the weather condition of Mozambique will benefit all actors of the process namely: *Briquette*

producers factories can be a great achievement for these group when the scarcity of drying space and difficulties with drying in the rainy season becomes no longer a problem, reducing also the long drying time contributing to the low price of briquettes. *Women and children* can save their precious time and efforts that are spent during the day walking very long distances on fuel collection which leads to deforestation, instead of education or other incomes generation. *Unemployment*, the briquette factories with this technology can increase the briquette production and employ more people to answer the demand of the market. *Waste management*, the increase of briquette production implies an increase on the raw material collection that is considered as solid residues around the cities. *Environmentally*, the introduction of the proposed technology not only will make the briquette an affordable source of energy but will also motivate people to shift to these clean and renewable option *reducing the levels of deforestation*.

1.6 Description of the Study Area

Mozambique is a country situated in the southeast part of the African continent (A), and on the eastern coast of Southern Africa, georeferenced between the latitude 10°27'S & 26°52'S and longitude 30° 12'W & 40°51'W (B). It is bordered by Tanzania to the north, to the west by Malawi, Zambia, Zimbabwe, South Africa and Swaziland, has a coastline of 2,500km, occupying an area of 799,380 km².

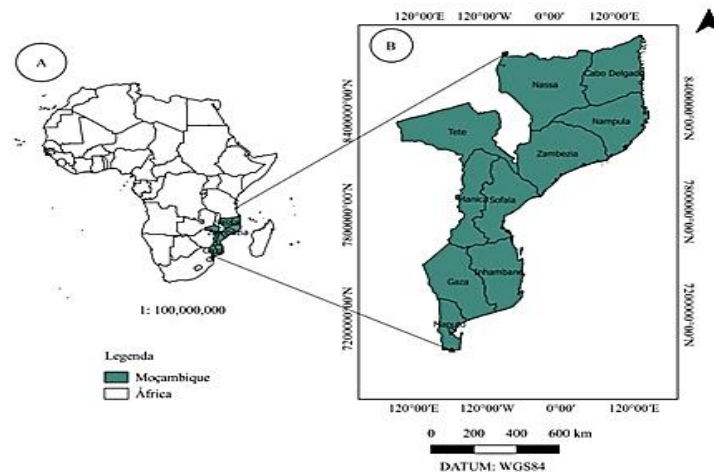


Figure 1.1: Location of Mozambique (B) on the African continent (A)

Administratively the country is divided into four levels namely, provinces, district, administrative post and locality. It has eleven provinces distributed in the three regions. It presents a humid

tropical climate with a cool and dry season (between the months of April and September) and a hot and humid one (from October to March) with an average annual temperature in warmer regions of 20 to 27 °C and cooler regions from 15 to 25°C. The average daily wind speed is around 7.3 km/h and the annual relative humidity of 63.4%. The location, topography and distribution of hydrographic networks are determining factors for the great ecological diversity and development of renewable energy technologies in Mozambique [19].

CHAPTER 2

LITERATURE REVIEW

2.1 Solar Energy Potential of Mozambique

The electrification in Mozambique is still very limited with only around 18 % of the population connected to the national grid. On top of this, there are high losses approximately 25 % due to transmission and distribution technologies [20, 21]. Therefore, solar thermal energy is considered a promising alternative source for electrical energy in the country, to answer these energy demands specifically in sectors such as agricultural and fish preservation industry that huge amount of electricity is needed to dry the products.

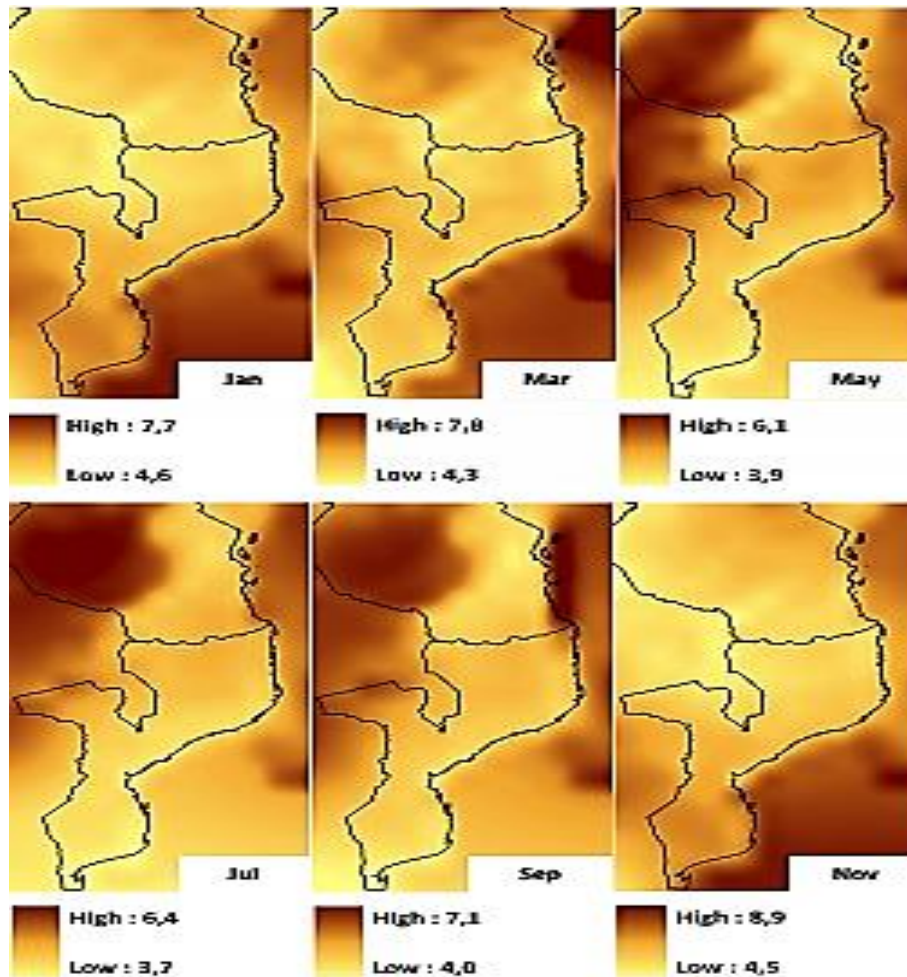


Figure 2.1. Monthly averages of insolation kWh/(m² day) in Tanzania and Mozambique derived from interpolation of SSE data [22].

As Mozambique is a tropical country in the southern hemisphere, it receives a consequent amount of solar radiation. Figure 2.2. Shows the annual averages of insolation in Mozambique and Tanzania given in kWh/m²/day, it was collected from ground measurements and interpolation found in Hammar [22]. The annual means of global solar radiation varies from 4.5 to 6.0 kWh/(m² day) according to ground measurements, and reaches 6.3 kWh/(m² day) according to interpolation of NASA Surface Meteorology and Solar Energy (SSE) estimations. This reveals a good potential for solar energy conversion all through the region. For small-scale use of solar photovoltaic technologies is projected to be adequate from approximately 4 kWh/(m² day) while larger installations such as solar thermal power plants require about 5 kWh/(m² day) [21, 23]. According to SSE data, the seasonal deviations are high in western Tanzania. In this region the highest insolation occurs during May–September, while most other areas including most of Mozambique peaks during November–March and the lowest insolation occur during the southern hemisphere winter [22].

2.2 Solar Briquette Drying Technology

The use of solar energy for drying purposes, is not a new technology, it has been widely applied in agriculture mostly for drying crops and fruits [24]. Solar drying uses the sun as the main source of energy. These dryers are frequently made of a simple construction increasing the percentage of radiation captured, compared to direct sun drying. This is done by concentrating the solar energy collected to the drying object by using the green-house-effect, airflow or reflectors [25]. Compared to sun drying, solar dryers can generate higher air temperatures, reducing drying time and space needed. Limited number of studies were conducted on drying biomass fuel briquette, many articles about drying technologies emphasis mostly on preservation of agricultural products and sea food. Briquetting is considered as a process where low bulk density biomass is converted into high density and energy concentrated fuel.

Biomass briquettes are solid fuels that can be made from carbonized biomass or densified biomass that is subsequently carbonized or not [6]. The first step producing these charcoal briquettes is to crush and mix the raw material with a binder then submit it to high pressure compaction to agglomerate the particles. Immediately after pressing, the produced wet briquettes have a moisture content of 50% while if the moisture content is more than 10% the charcoal briquette burns slower, with a lot of smoke and lighting up takes longer, these characteristics can be seen as an indicator

of poor quality of the product from the customers [12]. Therefore, to reduce the amount of moisture to acceptable levels for complete combustion, briquette producers spread these fuels under the sun (Figure 2.3) for around 4 to 7 days depending on the weather conditions of the region.



Figure 2.2: Drying briquette under the sun in Mozambique [26]

Mozambican briquette producers and other Sub-Saharan African countries point to the scarcity of drying space and challenges with drying in the rainy season as factors limiting the production scale and its consistency [6, 26]. Moreover, these producers are dependent on weather conditions automatically it implies very low productivity or even temporary closure of their operations, therefore, solar drying technology can be seen as an alternative solution to overcome the restrictions mentioned above.

2.3 Effect of Drying on Briquette Quality

2.3.1 Temperature and Drying Time

Briquettes made from carbonized biomass can take about 5 to 7 days to dry under open sun drying depending on the weather conditions additionally, it is stated that temperatures of around 25 to 40 °C are considered suitable for the fuel. The drying periods also depend on the size and type of material used for producing the briquettes. Moreover, this drying period allows a safe store and transport of the fuel to the users avoiding it breaking during the journey. After drying, briquettes can also be stored at room temperature usually about 20 °C, this is because storage at higher temperatures can make briquettes too dry and result in difficulty to ignite, while low temperature would make the briquettes soft and not durable during burning [27].

Fuel briquettes should be protected from direct rain and dried well to about 10% moisture content and drying undercover is recommended also because drying them under direct sunlight makes

them break. These recommendations can only be achieved if applied solar drying equipment to faster the drying process.

2.3.2 Moisture Content

The moisture content of charcoal fuel briquettes is a quality feature and affects directly the decision of the customer to buy. If the moisture content is overhead 10 % the charcoal briquettes burn slower and lighting takes longer, which suggests reduced quality to the clients. Poor briquette quality means that the customers are likely to be discouraged due to the performance of the product. To increase the quality of charcoal the moisture content has to be reduced from around 50% to less than 10% before for sale in the market. Investigations made on briquetting making process in Nairobi Kenya show that the sun-drying system is commonly used to dry carbonized briquettes from 5 up to 7 days [27]. During the dehydration process, it has to be taken into consideration the fact that biomass materials are heat sensitive but, it is possible to dry at a relatively high temperature exposing the fuel in a short drying period.

2.4 Types of Solar Dryers

Drying systems can be classified into two comprehensive categories fossil or conventional dryers and solar dryers. Fossil dryers use fossil fuels as their source of energy for operation. High prices and shortages of fossil fuels have increased the importance of using alternative renewable energy resources. Therefore, the usage of solar energy in drying applications is becoming an essential and feasible alternative since it reduces the consumption of conventional energy by 27–80% at an average solar collector system efficiency of 40% [28]. Hence, it is considered as one of the greatest promising sources of energy especially because it is environmentally clean, inexhaustible, plentiful, and freely available energy.

The main purpose of a dryer is to provide more heat to the product than what is available naturally under ambient conditions, hence increasing adequately the vapor pressure of the dried product moisture content, consequently, its migration from the product will also be improved. The dryer also considerably decreases the relative humidity of the drying air, and by doing so, its moisture-carrying capability increases, consequently ensuring sufficiently low equilibrium moisture content [29]. A classification diagram of drying equipment based on heat transfer is illustrated in Figure 2.4 beneath. This chart categorizes dryers as direct or indirect, with subclasses of continuous

operation. Overall, Megha and Salve [29] classified solar energy systems according to their heating modes and the method in which the solar heat is applied in two main divisions and these are passive or natural convection and active or forced convection solar driers.

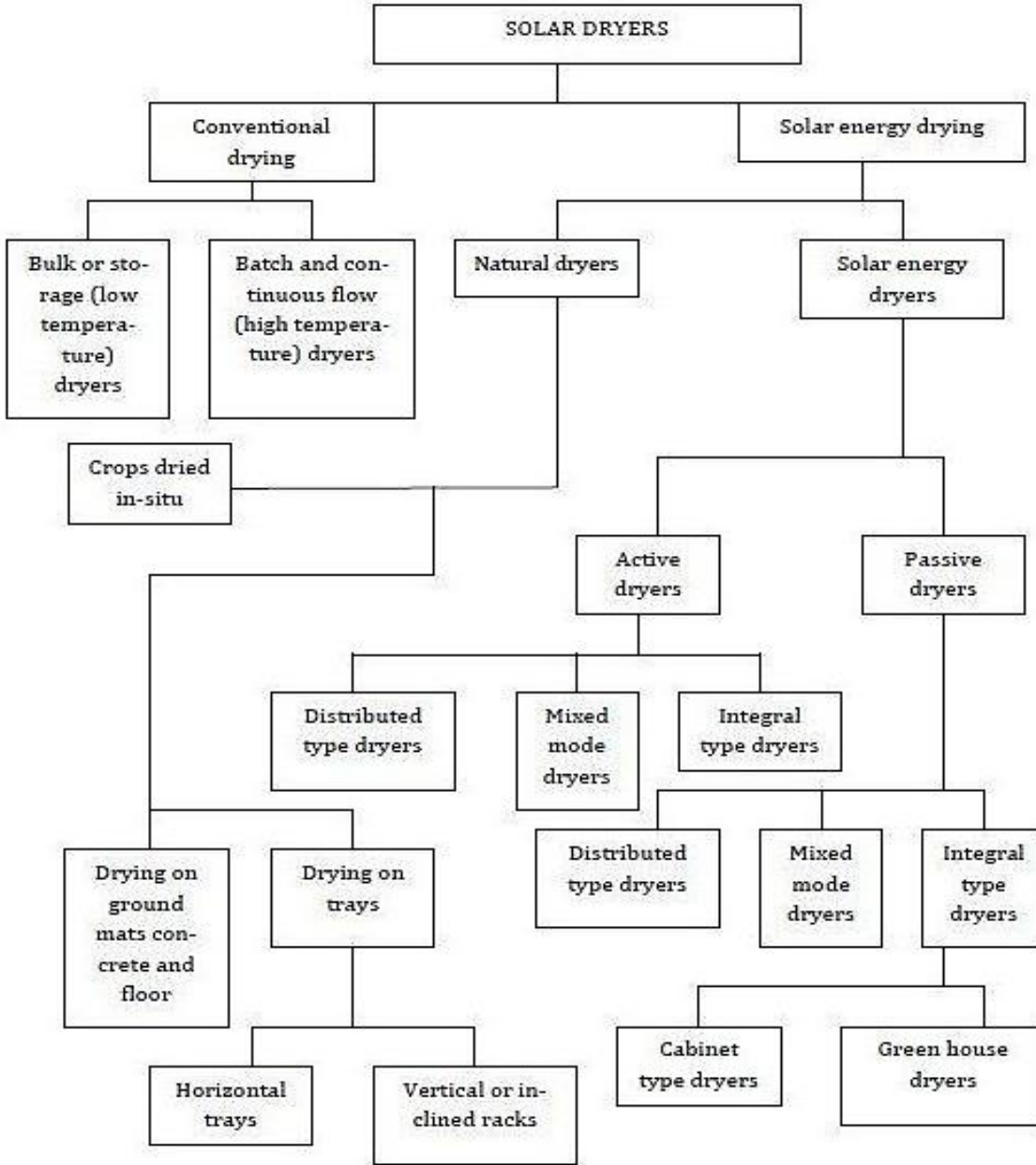
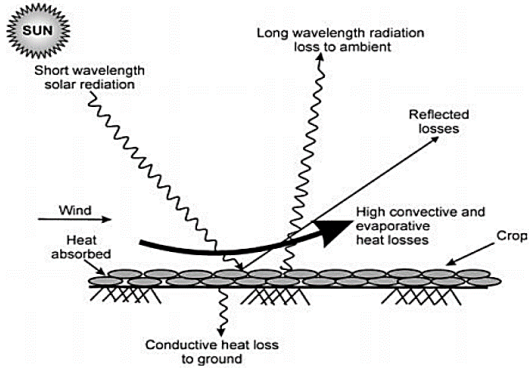
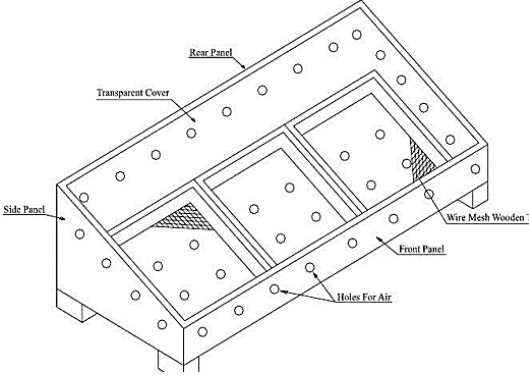
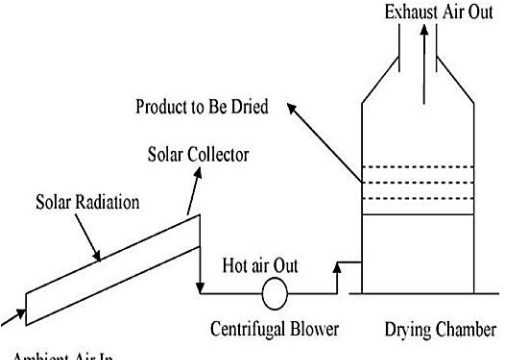


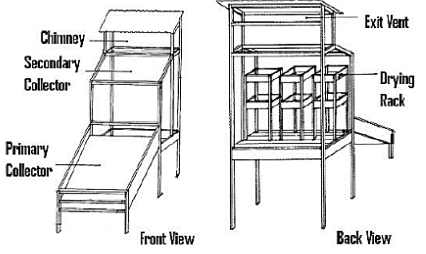
Figure 2.3: Classification of dryer and drying mode [30].

In the natural convection type of solar dryers buoyancy creates the airflow while in forced convection, a fan working with fossil fuel, electricity, or solar module provides the airflow. A huge advantage of natural convection solar dryers is that a minor investment is required principally due

to the low cost of the design process, maintenances as well as operation when compared to the forced convection type. Nevertheless, the natural convection solar dryers have had unsatisfactory realization so far, mostly due to the lower drying rates and trouble in managing, controlling the drying temperatures.

Table 2.1: Classification, Advantages, and Disadvantages of the Four Types of Solar Driers

Classification	Description	Advantages	Drawbacks
 <p>The diagram illustrates an open solar dryer. It shows the sun emitting short wavelength solar radiation towards a crop. Wind is shown blowing across the crop. Heat is absorbed by the crop, but there are several loss mechanisms: long wavelength radiation loss to the ambient, reflected losses, high convective and evaporative heat losses, and conductive heat loss to the ground.</p>	<p>Product placed on the ground open to the sun, which can reach higher temperatures in the open sun, and left there for some days to dry.</p>	<p>Simple Least expensive</p>	<p>Long drying time is required Output product quality is poor Contamination by dirt, dust, bacteria/ damage product Drying rate is poor</p>
 <p>The diagram shows a box solar dryer. It consists of a rear panel, a transparent cover, a side panel, a front panel, and a wire mesh wooden tray. Holes for air are present in the tray. The product is placed on the tray inside the box.</p>	<p>Product is enclosed in a container with a clear lid allowing sun to shine directly. Holes allow for air circulation.</p>	<p>Less contamination Higher quality Prod. than open sun dryer</p>	<p>Same time for drying natural drying UV radiation can damage product</p>
 <p>The diagram depicts a solar tunnel dryer. It features a solar collector that receives solar radiation and heats ambient air. A centrifugal blower circulates the hot air through a drying chamber where the product to be dried is placed. Exhaust air is then vented out.</p>	<p>Fresh air is heated in a solar heat collector, then passed through the product in the drier. The process is either passive or active. The material is not exposed to direct sunlight.</p>	<p>Less drying time for some product less damage from temperature extremes Product protected from UV</p>	<p>More complex and expensive than direct sun Maintenance after a particular period of time.</p>

	<p>Combines the direct and indirect types; a separate collector preheats air and direct sunlight adds heat to the food and air.</p>	<p>The rapid rate of drying with safe moisture level Drying time is less than other techniques</p>	<p>UV radiation can damage the product High capital and maintenance costs</p>
---	---	--	---

Researchers were consequently stimulated to develop the forced convection type of dryers. Moreover, this can further be divided into three modes depending on the mode of heat transfer from the sun to the product, which is direct, indirect, and mixed modes, summarized in Table 2.1 which describes the four categories of solar driers along with advantages and disadvantages of each [30, 31].

2.5 Drying Theory

Drying is the process of removal of moisture from the product to a quantified value due to the application of heat energy. In other words, drying is a combination of heat and mass transfer [32]. During sun drying heat is transferred by convection from the surrounding air and by absorption of direct and diffuse radiation on the top of the product. The converted heat is partly conducted to the interior increasing the temperature of the material and partly used for effecting migration of water and vapor from the interior to the surface. The remaining amount of energy is used for evaporation of water at the surface or lost to the ambient via convection and radiation. The evaporated water has to be removed from the surrounding by natural convection supported by wind forces [33, 34].

Under ambient conditions, these processes continue until the vapor pressure of the moisture held in the product equals that held in the atmosphere. Consequently, the rate of moisture desorption from the product to the environment and absorption from the environment are in equilibrium, and the crop moisture at this condition is known as the equilibrium moisture content. Water may be found in various forms. Free or loose held moisture is observed as unbound and bound moisture is trapped in closed capillaries of the material. In most products, there is a mixture of free or unbound and bound moisture. Free moisture is water that can move through the product in an unobstructed way, its movement is not dependent on the internal structure of the product [35].

The vaporization process is at a maximum when there is enough free water in the product to substitute that evaporated at its surface. As this moisture evaporates, the moisture content of the

product decreases and the product temperature is near to the wet bulb temperature of the drying air. This period in the drying process is usually known as the constant rate drying period and is shown in Figure 2.5. The factors that regulate the drying rate in this period are essentially external parameters such as air temperature, velocity, and the product surface area [34, 36].

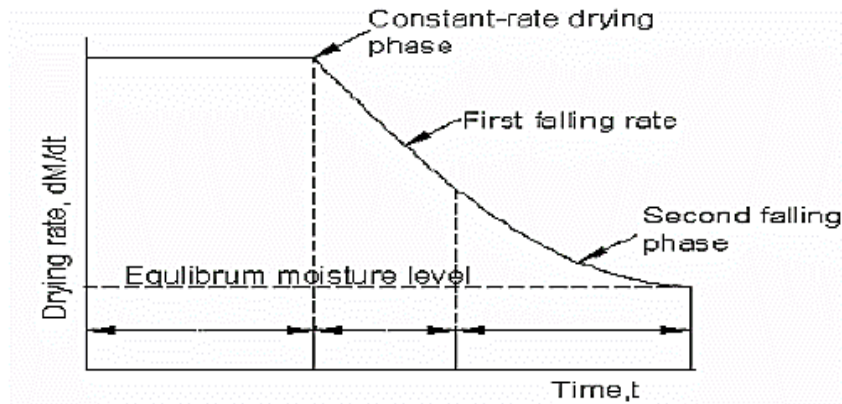


Figure 2.4: Illustration of a drying schedule [34].

Products with hygroscopic properties, during sun drying the crop, can either be dried or rewetted depending on the environmental conditions that are exposed. Specifically, during night time when the ambient temperature, in general, is decreasing, causing a simultaneous increase of the humidity, remoistening effects can occur either by conduction of dew or vapor diffusion. For a controlled environment, a dryer can be applied with the purpose of supplying the product with more heat than what is available under atmospheric conditions, in that way increasing sufficiently the vapor pressure of the moisture held within the crop and decreasing considerably the relative humidity of the drying air and so increasing its moisture carrying capacity and sufficiently low equilibrium moisture content [35].

The moisture content of a product can be expressed in two different manners, either as a percentage wet basis (% wb) or as a percentage in dry basis (% db). The moisture content of a product expressed as a percentage dry basis is the ratio of the amount of water in the product at any time compared to the amount of dry matter in the product and the wet basis moisture is the ratio of the mass of water in a sample to wet mass of the sample. Producers commonly use the wet basis moisture content whereas researchers and academic professionals use the dry basis moisture content. It is essential when results are expressed in those percentages to show the moisture content basis that is being applied [34]. Whichever basis is considered, there are two moisture content levels, which are of the main interest. These are the initial moisture content, which is the amount

of moisture in the sample before drying, and final moisture content that is the moisture content of the product that has to be achieved by drying and is usually known as the safe moisture content.

2.6 Factors Affecting the Rate of Drying the Briquettes

The air drying rate of various materials depends on different process parameters, of which the most important are temperature, airflow and velocity of drying air, relative humidity, initial and final air and product temperature, and the material size with shape. Following are some descriptions of the parameters that affect the performance of the dryer [37]:

2.6.1 Effect of Temperature

Temperature is considered as an essential factor during the product drying operation. The drying rate increases with the temperature and the total drying time can be significantly reduced by using high temperature drying air, leading to improved capacity of the drying system. Though, there seems to be a boundary to which the drying air temperature can be increased, since disproportionately high temperature may undesirably affect the quality concerning the crack formation, poor quality, and even burning of the dried product. An appropriate balance between the rate of heat and mass transfer is consequently essential for maintaining good product quality.

When a moist solid is heated to an appropriate temperature, moisture vaporizes at or near the solid surface, and the heat required for evaporating moisture from the drying product is supplied by the external drying medium, usually air or hot gas. This transport of moisture within a solid takes place by a variety of mechanisms (capillary action, pressure induced transport, gravity) depending upon the nature and type of the solid and its state of aggregation. The mechanism that dominates depends on the nature of the solid, its pore structure and the rate of drying. Different mechanisms may come into play and dominate at different stages of drying of the same material.

2.6.2 Effect of Air Velocity

Air is typically used as a medium for heat and mass transfer during drying operations. Preferably, the air velocity or flow rate should be such that when the air exists in the product bed, it should give up all its sensible heat and become saturated with moisture. If the air velocity is very low, the air temperature may drop quickly to the ambient level and may become saturated with moisture before it reaches the top of the bed, if the hot air temperature falls below its dew point before exiting the bed, the moisture will condense in the upper layers of the bed. On the other side, if a

too high velocity of air is used for drying, its heat and mass transfer potential would be under-utilized. At higher airflow rates, there is a logarithmic decrease in drying time (Figure 2.6).

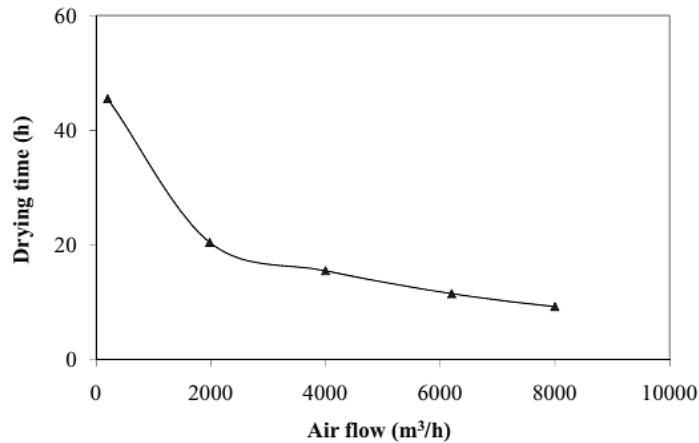


Figure 2.5: Effect of airflow rate on drying time of moist agricultural products [37]

The leaving air may still possess significant heat transfer potential and may exit the bed unsaturated. Another important aspect to be considered is pressure along with air velocity and has an impact in the design of blowers for drying systems concerning pressure drop. It is also necessary to highlight the influence of the drying bed of solids in the process saying that it offers resistance to airflow. The kinetic energy of the entering drying air falls continuously as it attacks upon the particles in the bed and rises from the bottom to the top of the particulates bed. If the incoming air has given up all its kinetic energy before it reaches the upper layer, it will stop flowing and only trickle into the bed.

The drying rate grows with the velocity of drying air during the constant rate period when enough moisture is existent at the material surface to be evaporated and carried away by passing air. Nevertheless, during the falling rate period, the rate of drying is limited by the availability of moisture at the surface, and air velocity does not affect the drying rate beyond a certain limit. In these circumstances, increasing the air velocity (or the flow rate) does not rise the drying rate, and the heat and mass transfer potential of the air would be under-utilized.

2.6.3 Effect of Briquette Shape and Thickness

Size reduction (length and thickness) increases the total surface area available for heat and mass transfer. The drying rate consequently increases with the reduced size of drying material resulting in a shorter drying time. The small size of the materials may hence be dried fully, while huge

portions should be cut into smaller pieces to succeed to get faster rates of drying, reducing the total drying time, and maintenance of quality. Different experiments on the production of biomass briquette state that is not recommended to break into smaller parts this fuel to achieve a fast drying rate because, during combustion, the aggregated particles may spread [6, 27]. The literature also says that working on the shape using molds with holes can increase the contact surface area of the briquette.

2.6.4 Effect of Relative Humidity

The relative humidity is an indication of the amount of water vapor contained in a certain amount of air divided by the maximum amount of water vapor the air could hold at that temperature and it is expressed as a percentage value. The drying rate rises and drying time decreases, with the reduction in RH of the drying air, so wet air prolongs the drying time. Though, a comparatively higher RH of drying air is recommended in combination with high temperature because a high RH contributes to maintaining the capillary pores and consequently minimizes the chances of case hardening. In practice, the RH of the drying air is not regulated. At high humidity levels, the drying conditions become less intense and as a consequence, the product has to be treated for longer periods in the dryer [38, 39].

2.7 Computational Fluid Dynamics in Solar Drying Systems

Computational Fluid Dynamics (CFD) is a remarkable modelling method that is applied for precisely predicting and solving complex fluid flow regimes. It is used in numerous engineering applications including analysis of solar drying systems. Since at least 1976 various designs of dryers, mostly those incorporating solar energy, have been investigated by different researchers to assess their performance [40, 41]. Studies confirm that solar dryer performance is considerably affected by ambient weather conditions. This brings a challenge in measuring important parameters of dryers such as thermal efficiency, drying rate, and drying capacity. To overcome these barriers, one of the technological methods employed in solar drying is the usage of Computational Fluid Dynamics (CFD) tools to model and simulate the drying kinetics of agricultural products, seafood, and biomass in general.

CFD is a great and innovative computational technique that uses numerical calculations and algorithms to solve and analyze problems associated with fluid flow in specified regions of interest

[40, 42]. Using a modern tool such as CFD impedes the problem of needing to run several experimental drying trials in order to select an appropriate design. In addition to the weather effects on drying, the performance of solar dryers also depends on product moisture because this also influences the drying rate. This suggests that for consistency, any comparisons of drying trials need to have products with the same moisture content at the beginning of each test. Though, with the use of CFD, products in a solar dryer can be simulated at the same or different moisture content to account for non-uniformity in drying and improve performance as well as product quality. Rosli et al. [43] highlight that with variable information regarding drying conditions, it is more helpful and economical to model and simulate the drying process of products than conduct experiments. Jamaledine et al. [44] also indicated that with rapid development in technology, CFD is demonstrating to provide a real solution in predicting drying phenomenon and can be used in optimization, development of equipment, and drying strategies for a diversity of dryers.

2.8 Previous Studies on Solar Tunnel Greenhouse Dryer

A tunnel is an enclosed duct except at the entry and exit end and used for heating of air in numerous applications including drying. However, a greenhouse is a structure used for the production of vegetables/flowers along with effective drying of a large number of agro-commodities. Hence greenhouse structure can be used all over the year making it more reasonable and having low operating cost [30]. The dual function of greenhouse and dryer improves the return rate of investment [32]. Kumar et al. [45] and Janjai Serm [46] give the detailed types of greenhouse and suggested the even span, Quonset shape and parabolic roof type of greenhouse for maximum utilization of solar energy.

Several investigators have explored the solar tunnel and greenhouse dryers for drying various agricultural products. Numerals of studies have been presented on greenhouse tunnel dryers by Janjai Serm from 2003 through 2012. A PV-ventilated greenhouse dryer with a concrete floor for drying of chilies was developed by Janjai et al. [47] in 2007. The parabolic shape of greenhouse was covered with polycarbonate sheet. A solar PV module of 53 W was used to operate three fans to aerate the dryer. To study its performance, the greenhouse was used to dry 4 batches of chilies in December 2003–March 2004. They reported a maximum air temperature of 65 °C in the dryer and found that drying time in the dryer for drying of 100–150 kg of chilies was considerably less than the traditional open sun drying method.

Janjai et al. [48] summarize a detailed review of research and development work on performance evaluation of roof-integrated solar dryer for drying of rosella flower and chilly under forced convection mode. The dryer consists of two arrays solar collector (one at the south and the other at the north), drying bin, and electric powered fan to force the air over the product bed. The dryer has three compartments: first for the drying bin, second for preparation of products to be dried, and third for storage of dried product.

The polycarbonate sheet was used to cover the roof of the dryer. Field-level experiments confirmed that drying in the roof-integrated solar dryer results in a major reduction in drying time compared to the traditional drying method and a quality dry produce is obtained. The dryer has been found cost-efficient with a payback period of 5 years.

Janjai et al. [49] also proposed a PV greenhouse dryer under active mode to dry longan as well as banana and at the same time, the sample of the above products were also dried in open sun. The experimental data was validated by developing partial differential equations. During 10 full-scale investigational runs, drying air temperature changes in the range of 31–58 °C in drying of longan while a temperature change from 30 to 60 °C during drying of banana was observed. Experiments have revealed that longan and banana can be effectively dehydrated in 3–4 days, while it took 5–6 days for the traditional method under similar conditions.

Solar drying experiments for seedless grapes were conducted at Udaipur, India. For this purpose Rathore and Panwar [50] designed and developed a walk-in type hemicylindrical solar tunnel dryer. It consists of a hemispherical metallic structure covered with a polythene sheet. To generate a natural current of air inside the dryer, four chimneys were provided on the top of the dryer. During experimentation, the maximum heat loss was found in the northern side of the tunnel; hence a heat-protective wall was placed on the north side. The seedless grapes of 320 kg were dried from initial moisture content of 85% (w.b) to final moisture content of 16% (w.b) in seven days, while open sun drying took 11 days for the same moisture level. Results showed that air temperature inside the dryer increases rapidly and attains the maximum value of 65 °C.

CHAPTER 3

SOLAR DRYING SYSTEM DESIGN

Drying is the way of removing moisture from a given product through the utilization of thermal energy and they are the most energy-intensive process for effective vaporization of the water content of the product [52]. Among different types of drying systems, solar drying is the most known method, which consumes solar energy as a heating source. Solar drying systems are an improved form of sun drying, which is excused in a closed structure under relatively controlled conditions and they have been developed as an alternative to conventional drying methods [52]. Currently, different types of solar drying systems have been developed and the most widely used are solar dryers and solar greenhouse effect or solar tunnel dryer.

The proposed solar drying system is the integration of a solar tunnel dryer and solar air heater to maximize the drying efficiency and optimize drying time. This section presents the design, sub-system, and working principle of solar drying system for charcoal dust briquette drying. Also, includes the designing criteria, assumption and conditions, material selection, solar tunnel dryer design, solar air heater design, ductworks design, selection of blower and selection of fans.

3.1 Main Systems of SDS

The proposed solar drying system (SDS) is a combination of sub-systems with different operating principle. Schematic diagram of the overall SDS with sub-systems is presented by figure 3.1.

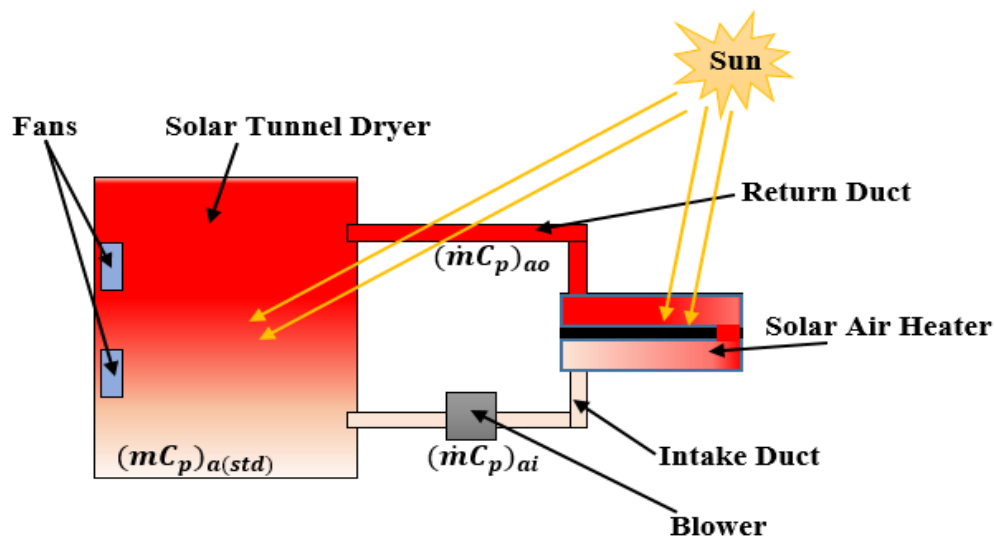


Figure 3.1: Schematic Diagram of Overall Solar Drying System

The main sub-systems included in the design of solar drying model are: *Solar Tunnel Dryer (STD)*, *Solar Air Heater (SAH)*, *Blower, Fan and Air Duct Lines*. The main function of each sub-systems will be discussed as follows:

Solar Tunnel Dryer: is a tunnel-like structure used as a drying chamber and its main function is drying the product by trapping the thermal energy supplied from solar radiation and solar air heater.

Solar Air Heater: is a flat plate-like collector which uses as an air heating device and its main function is heating and supplying hot air to the STD with desired temperature and flow rate by absorbing incidence solar radiation.

Blower: is a device that increases the pressure of air and its main function is increasing the pressure of air stream to circulate between the STD and SAH sub-systems through the intake and return duct lines.

Fan: is a device that increases the kinetic energy of air and its main function is regulating air mass flow rate and circulation inside the STD.

Air Duct Lines: this is a rectangular box structure which uses as an air transport device and its main function is to transport air from STD toward SAH through the intake duct and from SAH toward STD through the return duct.

3.2 Working Principle of SDS

The main purpose of the proposed SDS is drying charcoal duct briquette by utilizing thermal energy of the sun through STD and flat plate SAH collectors. The overall working principle of the system is removing moisture content of the product through forced convection, by gaining thermal energy from the air stream in the drying chamber which is heated by solar energy received by STD and SAH. The overall working principle and processes discussion of the proposed SDS will be presented by the schematic diagram shown in figure 3.2.

The working principle of the proposed method has three main units:

Unit 1: Solar Air Heater: under this unit, the solar radiation utilized by the collector is converted to useful thermal energy to heat the air stream. The main process of SAH is increasing the temperature of the air stream up to desired degree Celsius. The incoming air stream is heated by the absorber plate and duct material through convection modes of heat transfer. SAH unit has

different systems: *Air compression system*: is a blower used to increase the kinetic energy of air stream to flow through the SAH and ductworks (delivery and return). *Air delivery system*: is a duct line used to deliver the air stream with low temperature from the STD unit to the SAH unit. *Air return system*: is a duct line used to return the hot air stream from the SAH unit to the STD unit. The delivery duct lines must be insulated to prevent heat loss to the ambient.

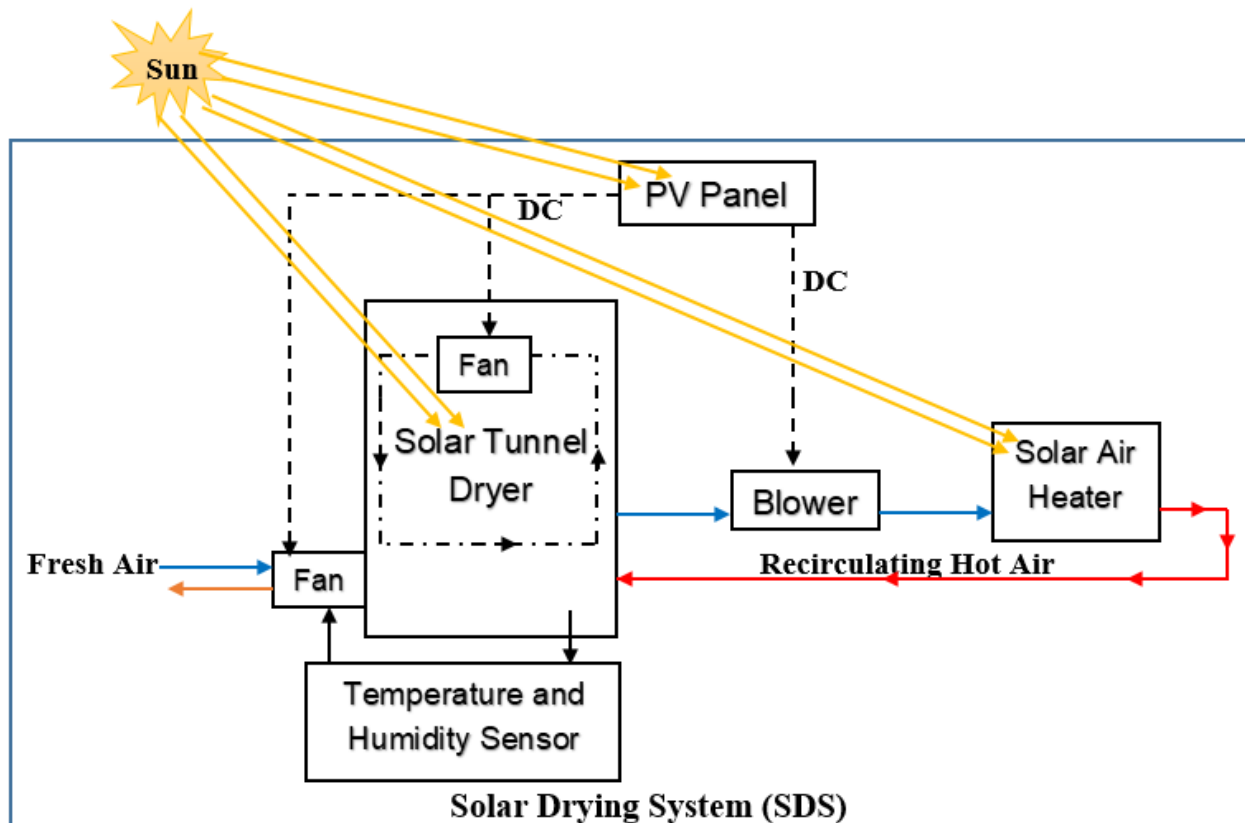


Figure 3.2: Schematic Diagram of Working Principle of STD

Unit 2: Solar Tunnel Dryer: under this unit, the temperature of the air inside the chamber is increased by utilizing thermal energy of sun radiation trapped inside the chamber and supplied from the SAH to heat the wet charcoal briquette. The chain of thermal energy flow inside the chamber is; from both the energy source to the air stream and finally from the air stream to the product. Therefore, the processes inside the STD unit can be categories into two main stages:

Stage 1: Sensible Heating: This is where the air stream is heated sensibly by the thermal energy sources inside the chamber. Airstream is heated by solar radiation through convection and by SAH

through directly mixing the cold air inside the chamber with the incoming hot air stream. Then, the product is heated sensibly by the hot air stream.

Stage 2: Latent Heating: This is where evaporation of moisture in the product starts by gaining latent heat from the air stream inside the chamber and solar radiation. The product is heated by the air stream through convection and by solar radiation through absorption of thermal energy. Finally, the water vapor is removed from the surface of the product by the flowing air stream. The circulation of the air stream inside the chamber is regulated by using fans.

Unit 3: Controlling: under this unit, the amount of temperature and humidity level of the air stream inside the STD unit is regulated by controlling devices (Temperature and Humidity Sensors).

3.3 Material Selection

Optimum material selection for the solar thermal system will maximize the thermal efficiency, absorption of incident solar radiation, useful heat gain, operation period and minimize drying rate, cost of drying, the energy required for drying, heat loss from drying chamber, total area required. In this analysis, optimum material will be selected for *STD and air duct lines sub-systems*.

3.3.1 Cover Material

In this study: for STD **Polythene Sheet** material is selected, due to the following reasons: *higher mechanical strength, lower failure rates, higher safety during usage, higher transmittance, availability, and affordability with reasonable cost (ANNEX B: Table B-2)*.

3.3.2 Air Duct Lines Material

Galvanized steel and aluminum are the most common *air duct lines material* for sheet metal ducts. In this study: for SAH Intake and Return Duct lines; **Aluminium (Al) sheet duct** is selected, due to the following reasons: *higher thermal and corrosion resistance, durability, strength, availability, manufacturing flexibility, affordability (lower cost per heat energy transfer rate), relatively light and easy to install. (ANNEX B: Table B-1)*

3.3.3 Insulation Material

Insulation Material should have resistant up to the maximum stagnation temperature of the collector usually about 150°C in and about 200°C when selectively coated absorbers are used. In this study, **Rockwool** insulation material is selected due to the following reasons: higher thermal

and water resistance, higher durability in the presence of moisture, *strength, availability, manufacturing flexibility, affordability (lower cost per heat energy resistance) and lower thermal conductivity.* (ANNEX B: Table B-4)

3.4 Design Criteria and Assumptions

The main criteria followed for design and analysis of the walk-in hemicylindrical with triangle structured solar tunnel dryer, flat plate solar air heating collector with riser and header ducts and air duct (intake and return lines) will be:

1. Incidence solar radiation and weather conditions (ambient temperature, humidity, and wind speed) are available around Maputo city in Mozambique.
2. Charcoal dust briquette as a drying product.
3. Moisture content of charcoal dust briquette product of Verde Africa LDA.
4. Thermal and physical properties of selected material

Additional, keeping in view of the following criteria.

1. **Durability:** of the drying system should be very high.
2. **Simplicity:** operation system as well as large scale loading and unloading of products for drying should be quite easy.
3. **Manufacturability:** it should be simple which can be manufactured using local materials and technologies.
4. **Flexibility:** it can be used for another type of biomass briquette product as well as for agricultural and industrial products with similar operation conditions or properties.
5. **Affordability:** the cost of manufacturing, installation, and operation should be affordable.

To carry out design calculation and size of the solar drying system, the following assumptions and conditions were made as summarized in Table 3.1.

Table 3.1: Design Conditions and Assumptions

Design Conditions and Assumptions	
Parameters	Specifications
Solar Tunnel Dryer	
Orientation	East – West Direction
Drying Product	Charcoal Dust Briquette

Loading Capacity		1120 kg
Dryer Efficiency		45%
Temperature of Air Stream		60°C
Temperature of Briquette		50°C
Diameter		4 m
Moisture Content	<i>Initial</i>	50%
	<i>Final</i>	10%
General Conditions		
Sunshine Hours		7.31 hrs
Global Solar Radiation		5.7 kWh/m²
Density of Ambient Air		1.225 kg/m³
Density of Water		997.77 kg/m³
Specific Heating Capacity of Water		4.2 kJ/kg K
Specific Heating Capacity of Charcoal Dust		1.002 kJ/kg K
Specific Heating Capacity of Air		1.005 kJ/kg K
Latent Heat of Vaporization of Water		2260 kJ/kg
Ambient Temperature		23°C
Heat Transfer Condition		Steady State

The conditions and assumptions are made based on the results of different related literatures and engineering properties (physical and chemical) of substance, to execute a theoretical design of a solar tunnel dryer and solar air heater.

3.5 Solar Tunnel Drier Design

The theoretical design of the proposed STD will be executed based on the above-mentioned criteria as well as conditions and assumptions summarized in table 3.1. Dimension calculation or sizing of the system will depend on the analysis result of the total amount of daily production of the company, the quantity of water content to be removed, the total amount of thermal energy required to achieve the desired moisture content, the amount of incident solar radiation on the horizontal surface, drying period and operating temperature of the product and air stream.

This section deals with the design and analysis of walk-in type hemicylindrical with a triangle shape solar tunnel drying system with a forced convection heat interaction between the air stream and drying product used to dry the wet charcoal dust briquette of Verde Africa LDA, in Mozambique. The design includes determining the effective collector area, the total quantity of

water content to be removed from the product, the total amount of heat energy required, the mass flow rate of air, and the overall dimension of the solar tunnel dryer.

3.5.1 Weight and Moisture Content Analysis

The total amount of daily wet charcoal dust briquette production capacity of Verde Africa LDA is equal to $m_{bi} = 1,120kg$, with the initial moisture content of $M_{i,wb} = 50\%$ in wet base. After, the drying process the amount of final desired moisture or water content of the product should be equals to $M_{f,wb} = 10\%$ in wet base.

⇒ *Wet Base Analysis of Mass and Moisture Content of Charcoal Dust Briquette*

The *amount of moisture content in wet base to be removed* ($M_{r,wb}$) from the product will be the difference of initial moisture ($M_{i,wb}$) and final moisture ($M_{f,wb}$) content and calculated as:

$$M_{r,wb} = M_{i,wb} - M_{f,wb} \text{ ----- (3.1)}$$

Where: $M_{i,wb}$ and $M_{f,wb}$ = is the initial and final moisture content of the product in a wet base.

$$M_{r,wb} = 50\% - 10\% = 40\%$$

The *initial mass of water content in the wet base* will be the product of total mass and initial moisture content of the daily production before drying and calculated as:

$$m_{wi} = m_{bi} * M_{i,wb} \text{ ----- (3.2)}$$

Where: m_{wi} = is the initial mass of water in the product, which is equal to:

$$m_{wi} = 1120kg * 0.5 = 560kg$$

The *total mass of solid (charcoal dust) in the product* will be the difference of total mass of the product and initial mass of water and calculated as:

$$m_s = m_{bi} - m_{wi} \text{ ----- (3.3)}$$

Where: m_s = is the total mass of solid in the product, which is equal to:

$$m_s = (1120 - 560)kg = 560kg$$

⇒ *Dry Base Analysis of Mass and Moisture Content of Charcoal Dust Briquette*

The *initial amount of moisture content in the dry base* will be determined as:

$$M_{i,db} = \frac{M_{i,wb}}{100 - M_{i,wb}} * 100\% \text{ ----- (3.4)}$$

Where: $M_{i,db}$ = is the initial moisture content in dry base, which is equal to:

$$M_{i,db} = \frac{50}{100 - 50} * 100\% = \mathbf{100\%}$$

The **final amount of moisture content in the dry base**, will be determined as:

$$M_{f,db} = \frac{M_{f,wb}}{100 - M_{f,wb}} * 100\% \text{ ----- (3.5)}$$

Where: $M_{f,db}$ = is the final moisture content in dry base, which is equal to:

$$M_{f,db} = \frac{10}{100 - 10} * 100\% = \mathbf{11.11\%}$$

The **amount of moisture content to be removed from the product in dry base**, will be the difference of the initial and final moisture content in dry base and determined as:

$$M_{r,db} = M_{f,db} - M_{i,db} \text{ ----- (3.6)}$$

Where: $M_{r,db}$ = is the amount of moisture to be removed in dry base, which is equal to:

$$M_{r,db} = (100 - 11.11)\% = \mathbf{88.89\% = 0.8889}$$

The **quantity of water to be removed** from the product during the drying period up to the desired amount of water content can be determined based on the amount of moisture content to be removed *in the dry base* and the total mass of solid matter, which is given by:

$$m_{wr} = m_s * M_{r,db} \text{ ----- (3.7)}$$

Where: m_{wr} = is the mass of water to be removed from the product, which is:

$$m_{wr} = 560kg * 0.8889 = \mathbf{497.8 kg}$$

The **final weight of charcoal briquette** after the drying process can be determined as:

$$m_{bf} = m_{bi} - m_{wr} \text{ ----- (3.8)}$$

Where: m_{bf} = is the final mass of the product after the end of the drying process.

$$m_{bf} = (1120 - 497.8)kg = \mathbf{622.2 kg}$$

The *final quantity of water* in the product after the end of the drying process can be determined as:

$$m_{wf} = m_s * M_{f,db} = m_{bf} - m_s \text{ ----- (3.9)}$$

Where: m_{wf} = is the final quantity of water in the dried product.

$$m_{wf} = 560kg * 0.1111 = (622.2 - 560)kg = \mathbf{62.2 kg}$$

The result of weight and moisture content analysis is summarized in table 3.2:

Table 3.2: Summary of Weight and Moisture Content Analysis

Weight and Moisture Content of Charcoal Briquette			
No	Property	Particles	Amount
Weight (kg)			
1.	Initial Mass	<i>Drying Product (m_{bi})</i>	1120
		<i>Water (m_{wi})</i>	560
		<i>Charcoal Dust (m_s)</i>	560
2.	Mass to be Removed	<i>Water (m_{wr})</i>	497.8
3.	Final Mass	<i>Dried Product (m_{bf})</i>	622.2
		<i>Water (m_{wf})</i>	62.2
		<i>Charcoal Dust (m_s)</i>	560
Moisture Content (%)			
4.	Moisture Content in Wet Base	<i>Initial ($M_{i,wb}$)</i>	50
		<i>Final ($M_{f,wb}$)</i>	10
		<i>To be Removed ($M_{r,wb}$)</i>	40
5.	Moisture Content in Dry Base	<i>Initial ($M_{i,db}$)</i>	100
		<i>Final ($M_{f,db}$)</i>	11.11
		<i>To be Removed ($M_{r,db}$)</i>	88.89

Essential parameters, which uses to design a solar tunnel dryer, such as: dimensions, thermal energy analysis, the mass flow rate of air, and collector area analysis will be calculated based on the data listed in table 3.2.

3.5.2 Thermal Energy Required for Drying

The total amount of heat energy required from the available solar radiation, to dry the wet charcoal briquette to the desired moisture content is the sum of the sensible heat of dry matter, the sensible heat of water, and the latent heat of the water.

Sensible heat ($Q_{s,b}$) required to heat charcoal dust in the product is:

$$Q_{s,b} = m_s C_{pb} (T_b - T_i) \text{ ----- (3.10)}$$

Sensible heat ($Q_{s,w}$) required to heat water in the product is given by:

$$Q_{s,w} = m_{wi} C_{pw} (T_w - T_i) \text{ ----- (3.11)}$$

Latent heat of water ($Q_{l,w}$) is given by:

$$Q_{l,w} = m_{wr} h_{fg} \text{ ----- (3.12)}$$

Where: C_{pb} = is the specific heating capacity of charcoal dust, C_{pw} = is the specific heating capacity of water, T_b = is the final temperature of charcoal dust in the product, T_w = is the final temperature of water in the drying product, T_i = is the initial temperature of the drying product and h_{fg} = is the latent heat of vaporization of water.

Temperature Assumption: the average daily room temperature of Maputo city is $T_i = 23^\circ\text{C}$ and assuming the drying temperature of the product $T_f = 50^\circ\text{C}$, based on different literature. Also, considering:

⇒ **Initial temperature** of charcoal dust and water is equal to the initial drying temperature of the product which is equal to the daily average ambient or room temperature of the location, $T_{bi} = T_{wi} = T_i = 23^\circ\text{C}$

⇒ **Final temperature** of charcoal dust and water is equal to the final drying temperature of the product, $T_b = T_w = T_f = 50^\circ\text{C}$

Therefore, the amount of heat energy required to dry the product up to desired moisture content is:

$$\text{Sensible heat of product} \dots \dots Q_{s,b} = [560 * 1.212 * (50 - 23)] \left(\frac{kg \cdot kJ \cdot K}{kg \cdot K} \right) = \mathbf{18.33 MJ}$$

$$\text{Sensible heat of water} \dots \dots \dots Q_{s,w} = [560 * 4.2 * (50 - 23)] \left(\frac{kg \cdot kJ \cdot K}{kg \cdot K} \right) = \mathbf{63.504 MJ}$$

$$\text{Latent heat of water} \dots \dots \dots Q_{l,w} = [497.8 * 2260] \left(\frac{kg \cdot kJ}{kg} \right) = \mathbf{1,125.028 MJ}$$

The *total amount of heat required to remove the water content from the product* will be calculated as:

$$Q_t = Q_{s,b} + Q_{s,w} + Q_{l,w} \text{ ----- (3.13)}$$

$$Q_t = (18.33 + 63.504 + 1,125.028)MJ = \mathbf{1,206.862 MJ}$$

The rate of thermal energy required during the drying period will be the ratio of total amount of heat required with drying time, and determined as:

$$\dot{Q}_r = \frac{Q_t}{t_d} \text{ ----- (3.14)}$$

Where: \dot{Q}_r = is the rate of thermal energy required and $t_d = \mathbf{7.31hr}$ is drying time,

$$\dot{Q}_r = \frac{1206.862 MJ}{(7.31 * 3600)sec} = \mathbf{45,860.3891 W = 45.8604 KW}$$

3.6 Area Optimization of Solar Tunnel Dryer

The size and shape of a given solar tunnel dryer mainly depend on the following criteria's: amount of available solar radiation, the mass of drying product, the amount of moisture content, the quantity of water to be removed, the amount of heat energy required to remove the moisture content, type of air circulation, type of convection heat transfer, the drying rate and weather conditions of the site location.

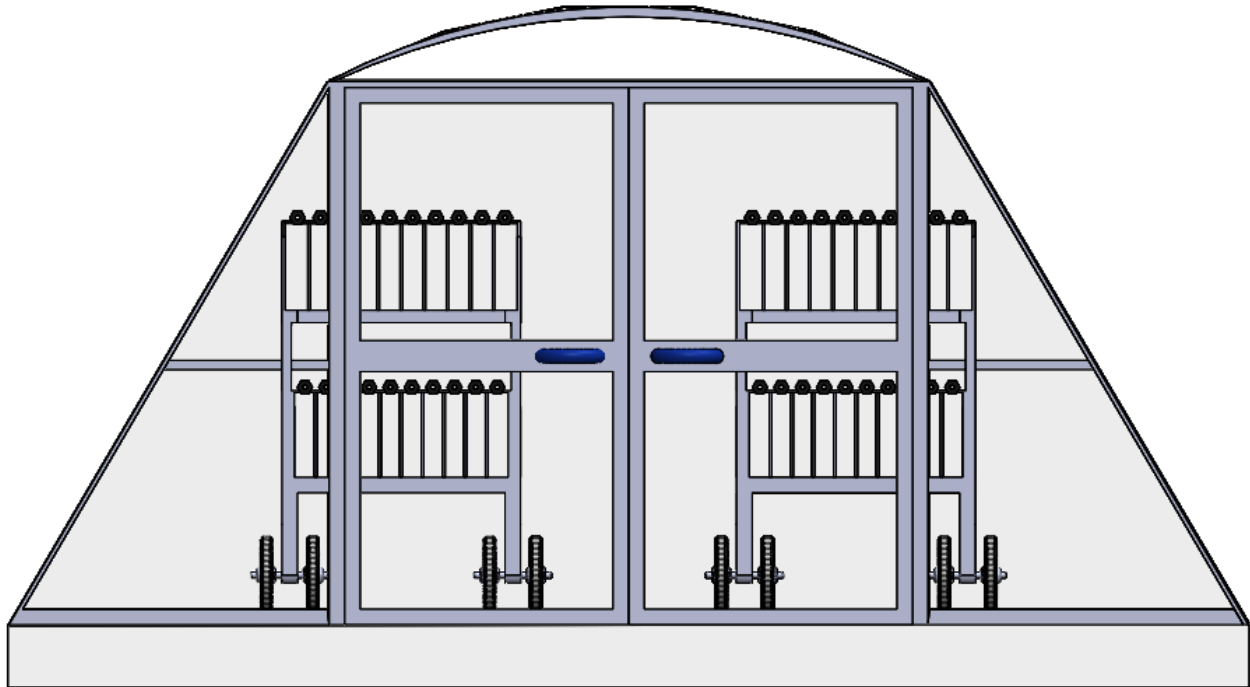


Figure 3.3: Front View of Selected Solar Tunnel Dryer

Under this project, the size and shape of the drying system will be analyzed based on above-mentioned criteria. Hemi-cylindrical shape with a pyramid-like structure is selected, to increase the area of solar radiation absorption by minimizing the effect of east-west orientation of hemicylindrical shape dryer (toward north 32% of sunlight is not able to receive) [52], where the selected shape is shown on figure 3.3.

3.6.1 Collector Surface Area (A_c)

Collector Surface Area (A_c): coverage can be determined based on the relation between the amount of thermal energy required, amount of incident solar radiation per unit area of location, and energy conversion efficiency of solar tunnel dryer. The required thermal energy will be supplied by two energy sources (solar radiation and SAH) and assuming the thermal energy supplied by solar radiation is 90%, while by SAH is 10% based on the cost of SAH and related literatures. Therefore, collector surface area will be calculated as:

$$A_c = \frac{0.9 * Q_{l,w}}{I * \eta} \text{----- (3.15)}$$

Where: A_c = is collector area of solar tunnel dryer, I = is the daily solar insolation of Maputo and η = is the efficiency of the system which is assumed 45%. Collector surface area coverage of the drying system will be:

$$A_c = \frac{0.9 * 1125.028 MJ}{(20.52 * 0.45) MJ/m^2} = 109.652 m^2 \approx 110 m^2$$

Face Surface Area (A_{fs}): of the drying system will be calculated based on the dimensions presented on figure 4.4, where the diameter (d_c) of the hemicylindrical shape is assumed as $d_c = 4m$ and it's kept as constant for easy entry and other convenience. The face surface area is the sum of the arc area, triangle 1 area and triangle 2 area, given as:

$$A_{fs} = A_{arc} + A_{t1} + A_{t2} \text{ ----- (3.16)}$$

Where: A_{fs} = is face surface area, A_{arc} , A_{t1} and A_{t2} = is the surface area of arc, triangle 1 and triangle 2.

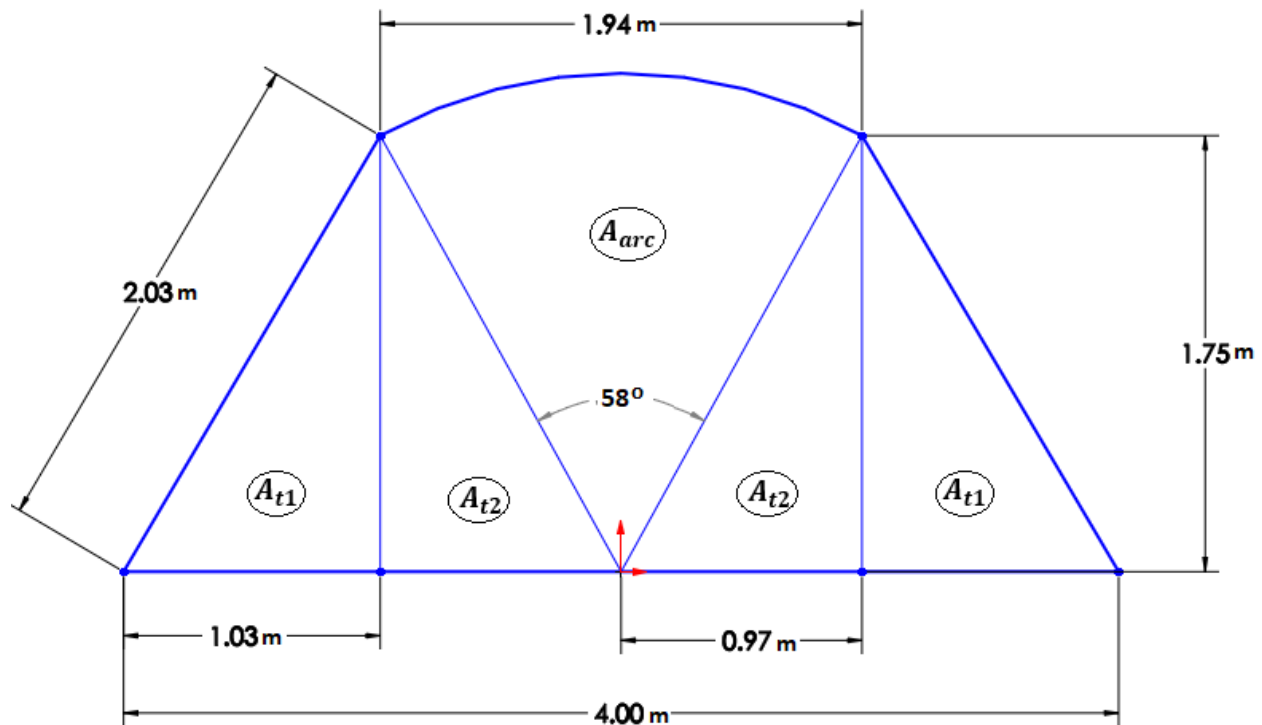


Figure 3.4: Face Surface of STD (Front View)

The area of arc, rectangle and triangle can be determined as determined as:

$$\text{Arc Area} \dots \dots \dots A_{arc} = \frac{\theta}{360} \pi r^2 = \frac{58}{360} * \pi * (2m)^2 = \mathbf{2.03 m^2}$$

$$\text{Triangle 1 Area} \dots \dots \dots A_{t1} = 2 * \left(\frac{1}{2}hb\right) = hb = 1.75m * 1.03m = \mathbf{1.803 m^2}$$

$$\text{Triangle 2 Area} \dots \dots \dots A_{t2} = 2 * \left(\frac{1}{2}hb\right) = hb = 1.75m * 0.97m = \mathbf{1.698 m^2}$$

Therefore, the face surface area of STD is equal to:

$$A_{fs} = (2.03 + 1.803 + 1.698)m^2 = \mathbf{5.531 m^2}$$

The **width of collector surface** (W_{cs}) is the sum of arc length (L_{arc}) and the hypotenuse length ($L_{t,h}$) of the two triangle, given by:

$$W_{cs} = L_{arc} + 2L_{t,h} \text{ ----- (3.17)}$$

Where: W_{cs} = is the width of collector surface, $L_{t,h} = \mathbf{2.03 m}$ is the length of the outer triangles hypotenuse surface and L_{arc} = is the length of arc surface, which is determined as:

$$\text{Arc Length} \dots \dots \dots L_{arc} = \frac{\theta}{180} \pi r = \frac{58}{180} * \pi * 2m = \mathbf{2.03 m}$$

Therefore, the total width of collector surface are of the STD is equal to:

$$W_{cs} = L_{arc} + 2L_{t,h} = (2.03 + (2 * 2.03))m = \mathbf{6.09 m}$$

The **length of collector** (L_{cs}) is equal to the ratio of total and face collector area and the total width coverage of collector, can be calculated as:

$$L_{cs} = \frac{A_c - A_{fs}}{W_{cs}} \text{ ----- (3.18)}$$

$$L_{cs} = \frac{(110 - 5.531)m^2}{(6.09)m} = \mathbf{17.1542 \approx 17.5 m}$$

The **floor surface area of the drying system** will be the product of collector length ($L_c = \mathbf{17.5 m}$) and floor width, which is equal to the diameter of hemi-cylindrical surface ($d_c = \mathbf{4 m}$), given by:

$$A_{floor} = L_c * d_c \text{ ----- (3.19)}$$

The total floor surface area of the STD system will be:

$$A_{floor} = 17.5 \text{ m} * 4\text{m} = 70 \text{ m}^2$$

3.6.2 Charcoal Dust Briquette Area

The *total area coverage of charcoal dust briquette* is depend on the size or dimension specification of a single briquette product of Verde Africa LDA Company, which is listed in table 3.3 and The shape and size of briquette produced by Verde Africa LDA Company is shown on (ANNEX C: Figure (C-1)) and a schematic diagram is shown on figure 3.5:

Table 3.3: Dimension Specification of Verde Africa LDA

No.	Dimension	Amount
1	Length (L)	0.15 m
2	One Side Width (S)	0.025 m
3	Width (W)	0.05 m
4	Height (h)	(0.04 m)
5	Hole Diameter (D_{hl})	0.015 m
6	Total Number of Briquette (n_t)	3200 pc

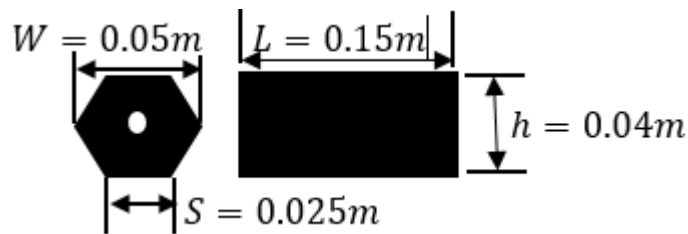


Figure 3.5: The Size of Charcoal Briquette of Verde Africa LDA

1) The *overall outer surface area of the CDB* will be the sum of face surface area, lateral (side) surface area and circular-hole surface area of a single CDB, multiplied by the total number of daily production, which is:

$$A_{osb} = n_t(A_{fsb} + A_{lsb} + A_{hsb}) \text{ --- (3.20)}$$

Where: A_{osb} = is the overall outer surface area of CDB, A_{fsb} , A_{lsb} and A_{hsb} = is the face, lateral and circular-hole surface area of a single briquette, which is calculated as:

⇒ The *face surface area of a single CDB*, will be the difference of the hexagonal shape and the circular shape geometry area, as:

$$A_{fsb} = A_h - A_c \text{ --- (3.21)}$$

Where: A_{fsb} , A_h and A_c = is the face surface area of a unit CDB, surface area of hexagon and surface area of circle respectively.

$$\text{Hexagonal Surface Area} \dots\dots A_h = \frac{3\sqrt{3}}{2} S^2 = \frac{3\sqrt{3}}{2} * (0.025m)^2 = \mathbf{0.001624 m^2}$$

$$\text{Circular Surface Area} \dots\dots\dots A_c = \pi \frac{D_{hl}^2}{4} = \pi * \frac{(0.015m)^2}{4} = \mathbf{0.0001767 m^2}$$

The *face surface area of a unit CDB*, will be:

$$A_{fsb} = (0.001624 - 0.0001767)m^2 = \mathbf{0.0014473 m^2}$$

⇒ The ***lateral surface area of a single CDB***, will be the product of length and face surface or hexagonal shape perimeter of a unit briquette, as:

$$A_{lsb} = L_b * P_{fsb} \text{-----}(3.22)$$

Where: P_{fsb} , = is the face (hexagonal) surface perimeter of a unit CDB, and calculated as:

$$P_h = 6 * S = 6 * 0.025m = \mathbf{0.15 m}$$

Where: S = is the width of each side, with equal dimension.

The *lateral surface area of a single CDB*, will be equals to:

$$A_{lsb} = 0.15m * 0.15m = \mathbf{0.0225 m^2}$$

⇒ The ***cylindrical-hole surface area of a single CDB***, will be the product of length and circular surface perimeter of a unit briquette, as:

$$A_{hsb} = P_{c,h} * L_b \text{-----}(3.23)$$

Where: A_{hsb} = is the cylindrical-hole surface area of CDB and P_c = is the perimeter of a circle, which is given by:

$$P_{c,h} = 2\pi r = 2 * \pi * 0.0075m = \mathbf{0.0471 m}$$

Where: $r = 0.0075 m$ is the radius of the hole, which is half of the circular-hole diameter.

The *cylindrical-hole surface area of a single CDB*, will be equals to:

$$A_{hsb} = 0.0471m * 0.15m = \mathbf{0.0071 m^2}$$

Therefore, the ***overall outer surface area of CDB***, will be equals to:

$$A_{osb} = 3200 * (0.0014473 + 0.0225 + 0.0071)m^2 = \mathbf{99.5 m^2}$$

2) The ***total area coverage of CDB*** inside the drying chamber will be determined based on the dimension showing on figure 3.5, as:

$$A_{bt} = n_t * L_b * W_b \text{ ----- (3.24)}$$

Where: A_{bt} = is overall top surface area, L_b = is length and W_b = is width of a single briquette and n_t = is total number of briquette production per day. Therefore,

$$A_{bt} = 3200 * (0.15m * 0.05m) = 24 m^2$$

3.7 Psychrometric Analysis of Drying Chamber

Psychrometry is the study of the thermodynamic properties of moist air (mixtures of air and water vapour) and it provides a picture of the way in which the state of moist air alters as the process takes place or a physical change occurs. The Psychrometric analysis of the drying system can be executed, by assuming the drying chamber as a control volume and based on the properties of moist air, like temperature (T), mass flow rate (\dot{m}_a), specific humidity (w) and relative humidity (w), which are involved at three major state (station) shown on Figure 3.6. The system included under the control volume (CV) mainly categorized into 2 major systems, *1) Air Heating System*, which are: *the hot air supplied by SAH and the thermal energy of solar radiation trapped inside the chamber* and *2) evaporation system*, where the water molecule inside the CDB evaporates by gaining heat from the hot air stream through convection. Among different types of important Psychrometric processes, only *sensible heating* and *adiabatic humidification processes* are involved under the drying chamber.

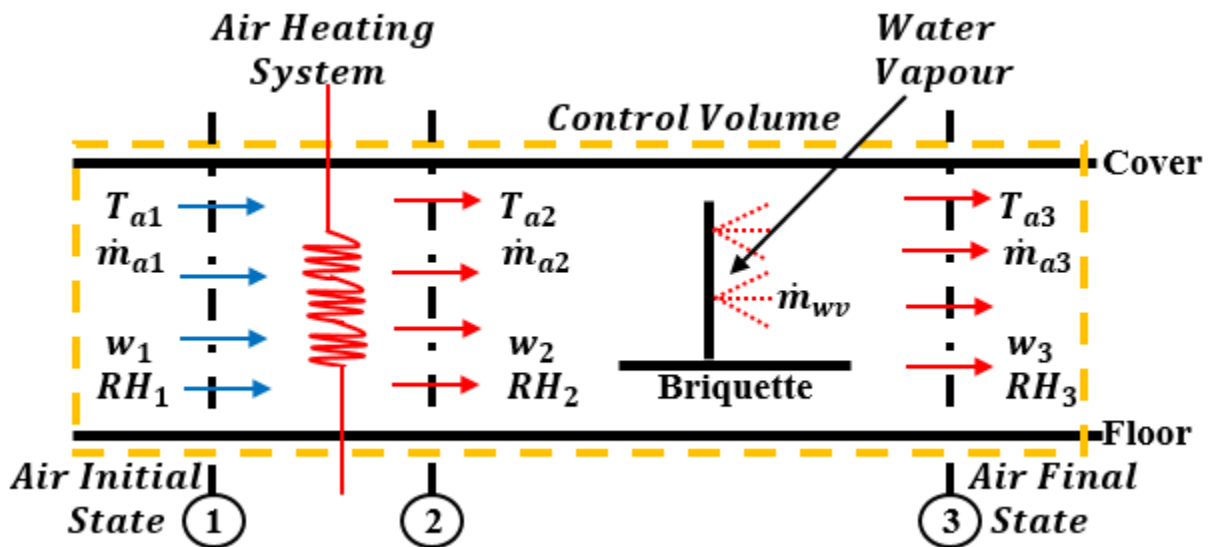


Figure 3.6: A Schematic Diagram of Drying Chamber with each Process involved

The properties of air stream in each state at a constant mass flow rate of air ($\dot{m}_a = \dot{m}_{a1} = \dot{m}_{a2} = \dot{m}_{a3}$), can be determined by using Psychrometric chart or analysis and by applying the principle of mass and energy balance on the control volume. (ANNEX C: Figure D-1).

@ **State 1:** is the initial state, where the properties of air stream are equal to the atmospheric or ambient air properties of Maputo city. Therefore, the annual average ambient air *dry bulb temperature (DBT)* is $T_{a1,d} = 23^\circ\text{C}$, the annual average ambient *relative humidity (RH)* is $RH_1 = 63.4\%$ and the value of *specific humidity (w)* and *wet bulb temperature (WBT)* can be determined from Psychrometric chart at corresponding $T_{a1,d}$ and RH_1 , which is equals to $w_1 = 0.011$ and $T_{a1,w} = 21^\circ\text{C}$.

@ **State 2:** is the second state, after the air stream is heated sensibly by heating systems up to a *DBT* of air equals to $T_{a2} = 60^\circ\text{C}$. There is no change in moisture content of air stream, which means the *specific humidity is constant* $w_1 = w_2 = 0.011$ and the *relative humidity* and *WBT* can be determined from Psychrometric chart at $T_{a2,d}$ and w_2 , where $RH_2 = 9\%$ and $T_{a2,w} = 28.5^\circ\text{C}$.

@ **State 3:** is the final state, after the adiabatic humidification processes, where the *WBT* is constant $T_{a3,w} = T_{a2,w} = 28.5^\circ\text{C}$ and *relative humidity* is equal to $RH_3 = 100\%$. The moisture content of air stream is increasing due to humidification process and the *WBT* is constant due to adiabatic process. The value of *specific humidity* and *DBT* can be determined from Psychrometric chart at $T_{a3,w}$ and RH_3 , which is equals to $w_3 = 0.025$ and $T_{a3,d} = 29.5^\circ\text{C}$.

3.7.1 Psychrometric Analysis for Adiabatic Humidification

The sensible heating process of air stream is from *state 1 up to state 2* and the adiabatic humidification process is from *state 2 up to state 3*, as shown on Figure 3.7.

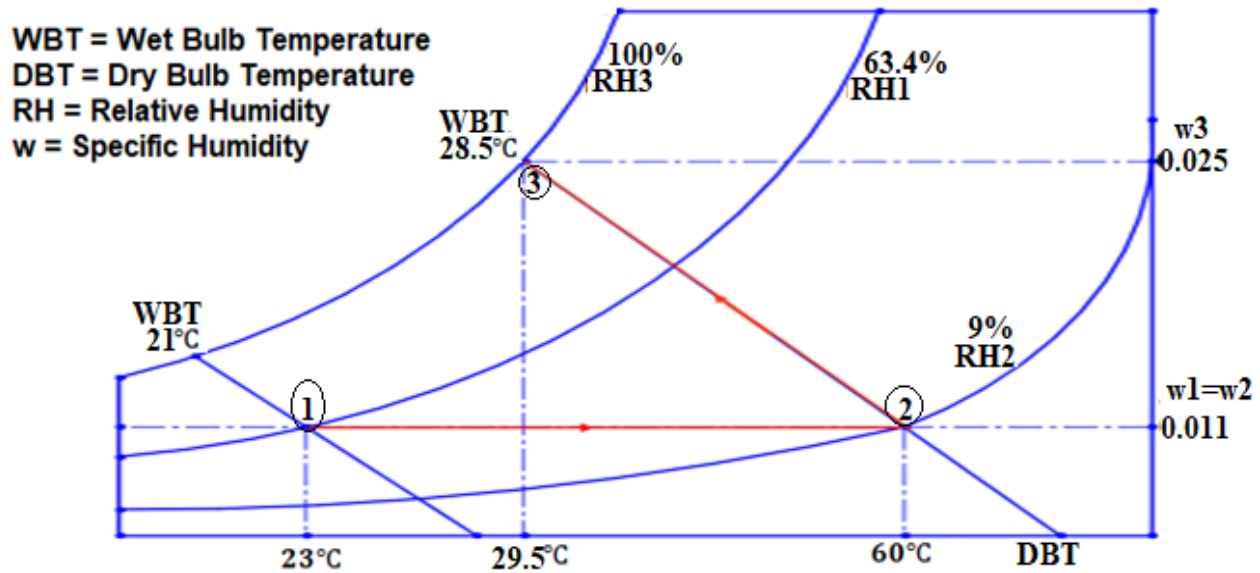


Figure 3.7: Psychrometric Chart of Adiabatic Humidification

Process (1-2): is a *sensible heating process*, where air stream heated at a constant moisture content. The dry bulb temperature of air increases from 23°C to 60°C, wet bulb temperature of air increases from 21°C to 28.5°C, the relative humidity decreases from 63.4% to 9% and the specific humidity is constant $w_1 = w_2 = 0.011$.

Process (2-3): is an *adiabatic humidification process*, where the moisture content of air stream increases. The dry bulb temperature of air decreases from 60°C to 29.5°C, wet bulb temperature of air remains constant $T_{a2,w} = T_{a3,w} = 28.5^\circ\text{C}$, the relative humidity increases from 9% to 90% and the specific humidity increases from 0.011 to 0.025.

Process (1-3): is a *sensible heating and adiabatic humidification process*, where both the temperature and moisture content of air stream inside the control volume (drying chamber) increases. The dry bulb temperature of air increases from 23°C to 29.5°C, the wet bulb temperature of air increases from 21°C to 28.5°C, the relative humidity increases from 63.4% to 100% and the specific humidity increases from 0.011 to 0.025.

3.7.2 Psychrometric Analysis for Non-Adiabatic Humidification

Figure 3.8 presents Psychrometric analysis for non-adiabatic humidification process of drying chamber.

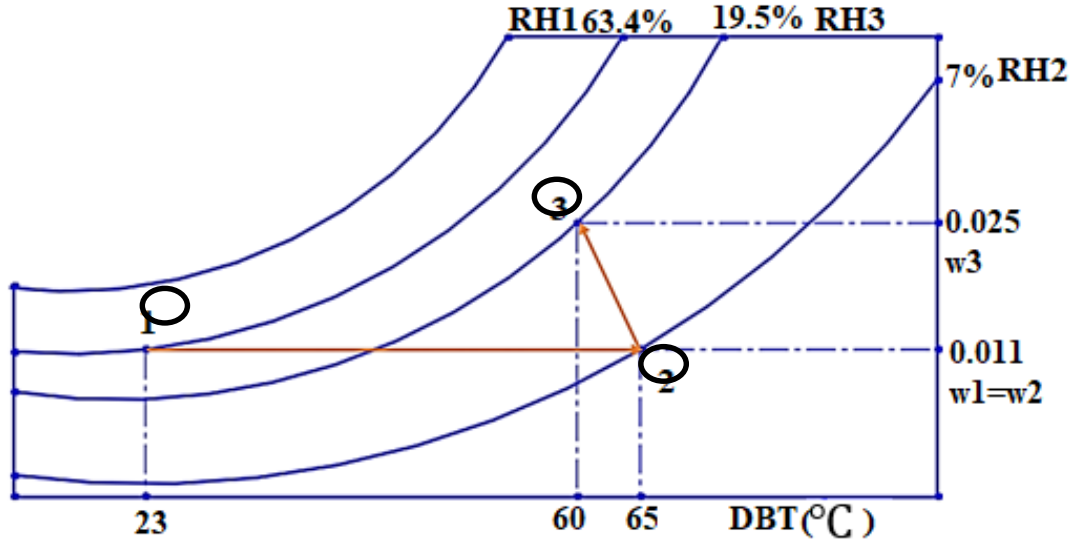


Figure 3.8: Psychrometric Chart of Non-Adiabatic Humidification

Process (1-2): is a *sensible heating process*, where air stream heated at a constant moisture content. The dry bulb temperature of air increases from 23°C to 65°C, wet bulb temperature of air increases from 21°C to 29.5°C, the relative humidity decreases from 63.4% to 7% and the specific humidity is constant $w_1 = w_2 = 0.011$.

Process (2-3): is *non-adiabatic humidification process*, where the moisture content of air stream increases. The dry bulb temperature of air decreases from 65°C to 60°C, wet bulb temperature increases from 29.5°C to 35°C, the relative humidity increases from 7% to 19.5% and the specific humidity increases from 0.011 to 0.025.

Process (1-3): is a *sensible heating and non-adiabatic humidification process*, where both the temperature and moisture content increases. The dry bulb temperature of air increases from 23°C to 60°C, the wet bulb temperature of air increases from 21°C to 35°C, the relative humidity decrease from 63.4% to 19.5% and the specific humidity increases from 0.011 to 0.025.

3.8 Estimation of Air Mass Flow Rate

The drying air flows over the product inside the STD, to remove or to carry moisture from its surface, which increases the drying or moisture removal rate of the system.

3.8.1 Estimation of Air Mass Flow Rate for Adiabatic Humidification

Mass flow rate of drying air mainly depends on the initial and the final humidity ratio or specific humidity, the constant drying rate, drying time, the amount of air and the amount of moisture inside the chamber. The mass flow rate of air can be determined by applying a mass balance principle on the system, assuming the drying chamber as a control volume, as shown on figure 4.5. Based on the principle of mass balance, the mass of vapor inside the drying chamber (control volume) is equal to the sum of mass of water vapor entering to the chamber through; 1) moist air and 2) evaporation, which is expressed as:

$$\dot{m}_{v3} = \dot{m}_{v2} + \dot{m}_f \quad \text{-----} \quad (3.25)$$

Where: $\dot{m}_{v3} = \dot{m}_a w_3$ is the amount of mass flow rate of water vapor inside the drying chamber, $\dot{m}_{v2} = \dot{m}_a w_2$ is the amount of mass flow rate of water vapor entering through moist air and \dot{m}_f is a constant drying rate of the product. Substituting the value of \dot{m}_{v3} and \dot{m}_{v2} into equation (3.25) and equating for mass flow rate of air will give as:

$$\dot{m}_a w_3 = \dot{m}_a w_2 + \dot{m}_f$$

$$\dot{m}_a = \frac{\dot{m}_f}{(w_3 - w_2)} \quad \text{-----} \quad (3.26)$$

Where: w_3 = is specific humidity at station 3 and w_2 = is specific humidity at station 2. *Drying Rate* (\dot{m}_f) of the product can be determined as:

$$\dot{m}_f = \frac{m_{wr}}{t_d} \quad \text{-----} \quad (3.27)$$

$$\dot{m}_f = \frac{497.8 \text{ kg}}{(7.31 * 3600)\text{s}} = \mathbf{0.019 \text{ kg/s}}$$

Finally, *mass flow rate of air stream inside the drying chamber* will be:

$$\dot{m}_a = \frac{0.019 \text{ (kg/s)}}{(0.025 - 0.011)} = \mathbf{1.3572 \text{ kg/s}}$$

3.8.2 Estimation of Air Mass Flow Rate for Non-Adiabatic Humidification

The estimation of mass flow rate air for non-adiabatic humidification or a sensible heating process presented by the red line between state 1 and state 2 in figure 3.6, is calculated based on the energy

balance principle. Assuming the drying chamber as a control volume (CV), the incidence solar radiation and thermal energy of air at state 1 and state 2 are shown by figure 3.9:

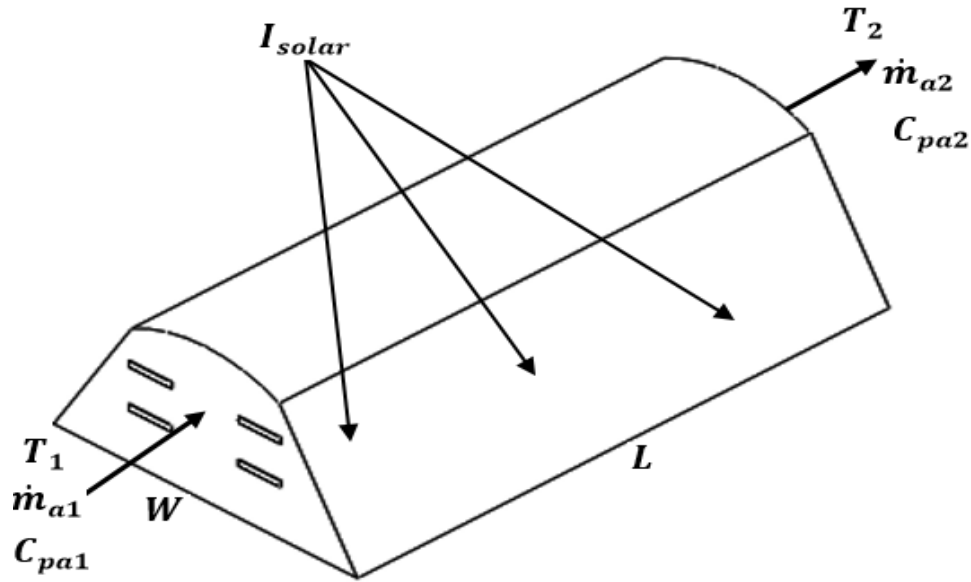


Figure 3.9: Schematic Diagram of Energy Balance of STD

Applying an energy balance principle on the CV, the intensity of useful solar radiation on the projected area is equal to the difference of the final (state 2) and initial (state 1) thermal energy of the air stream, which is expressed by equation (3.28).

$$E_{solar} = E_{air2} - E_{air1} \text{ ----- (3.28)}$$

Where: $E_{solar} = \eta I A_p$ is the *Useful Solar Radiation*, $E_{air2} = \dot{m}_{a2} h_2$ is the *final thermal energy* of air stream and $E_{air1} = \dot{m}_{a1} h_1$ is the *initial thermal energy* of air stream and substituting each expression into equation (3.28), will give us:

$$\eta I A_p = \dot{m}_{a2} h_2 - \dot{m}_{a1} C_{pa1} h_1 \text{ ----- (3.29)}$$

The mass flow rate of the air stream inside the CV is *constant*, where $\dot{m}_{a2} = \dot{m}_{a1} = \dot{m}_a$:

$$\eta I A_p = \dot{m}_a (h_2 - h_1) \text{ ----- (3.30)}$$

The expression of air mass flow rate for non-adiabatic humidification can be determined by rearranging equation (3.30) and equating it to \dot{m}_a the mass flow rate of air, as:

$$\dot{m}_a = \frac{\eta I A_p}{h_2 - h_1} \text{ ----- (3.31)}$$

Where: $\eta = 45\%$ assumed thermal efficiency of STD, $I = 779.8 \text{ W/m}^2$ is the average incidence solar irradiance, $A_p = W * L = A_{floor} = 70 \text{ m}^2$ is the projected area which is equal to the floor area of the chamber, $h_2 = 131.5 \text{ KJ/Kg}$ is the final enthalpy of moist air at $T_2 = 60^\circ\text{C}$ and final specific humidity $w_1 = 0.025$ and $h_1 = 95 \text{ KJ/Kg}$ is the initial enthalpy of moist air at $T_1 = 65^\circ\text{C}$ and initial specific humidity $w_1 = 0.011$ from Psychrometric chart. Therefore, \dot{m}_a will be:

$$\dot{m}_a = \frac{0.45 * 779.8 \text{ W/m}^2 * 70 \text{ m}^2}{(131.5 - 95)[\text{KJ/Kg}]}$$

$$\dot{m}_a = \mathbf{0.673 \text{ Kg/s}}$$

Generally, the estimated value of *mass flow rate of air stream: 1)* for the *Non-Adiabatic Humidification Process* is 0.6433 Kg/s (*state 1 → state 2*), and *2)* for the *Adiabatic Humidification Process* is 1.3572 Kg/s (*state 2 → state 3*).

3.9 Useful Energy Output

The total useful energy output of a drying chamber area (A_c) is the difference between the final and the initial thermal energy states of the moist air stream, which is defined as:

$$Q_u = \dot{m}_a(h_f - h_i)t_d \text{ ----- (3.32)}$$

Where: $\dot{m}_a = 1.3572 \text{ Kg/s}$ is air mass flow rate, $h_f = 131.5 \text{ KJ/Kg}$ and $h_i = 95 \text{ KJ/Kg}$ is the final and initial enthalpy of moist air and $t_d = 7.31 \text{ hr}$ is drying time. Therefore, the useful thermal energy of moist air Q_u will be:

$$Q_u = \left(1.3572 \frac{\text{Kg}}{\text{s}}\right) * \left[(131.5 - 95) \frac{\text{KJ}}{\text{Kg}}\right] * (7.31 \text{ h})$$

$$Q_u = \mathbf{362.12 \text{ KWh}}$$

The total useful energy received from drying air is 362.12 KWh .

3.10 Description of the Drying Chamber

A typical forced convection drying system mainly consists of a drying bed, fans, and a semi-cylindrical pipe structure covered with U.V. stabilized Polyethylene sheet of 200-micron thickness [52]. Mostly, the orientation of the drying chamber is arranged in the East-West direction, due to

its many advantages. This way of orientation is most efficient and appropriate than any other way of orientation since the solar radiation or light transmittance was high in this direction and maximum exposure to solar radiation was possible [53]. Due to the abovementioned advantages of East-West orientation, the proposed drying chamber will be arranged in this direction.

The designed drying chamber is a forced convection solar tunnel drying system, for charcoal dust briquette industrial products on large scale at moderate temperature, pressure, and humidity in Maputo city. The main components included in the design are a moveable drying bed, axial fans, a trapezoid with semi-cylindrical frame structure to stretch the cover, a transparent Polyethylene sheet cover, a double opening door, and a concrete foundation; to increase the productivity of the company and to simplify the working principle of the drying system. The overall schematic diagram of the designed drying chamber with main components is shown in figure 3.10.

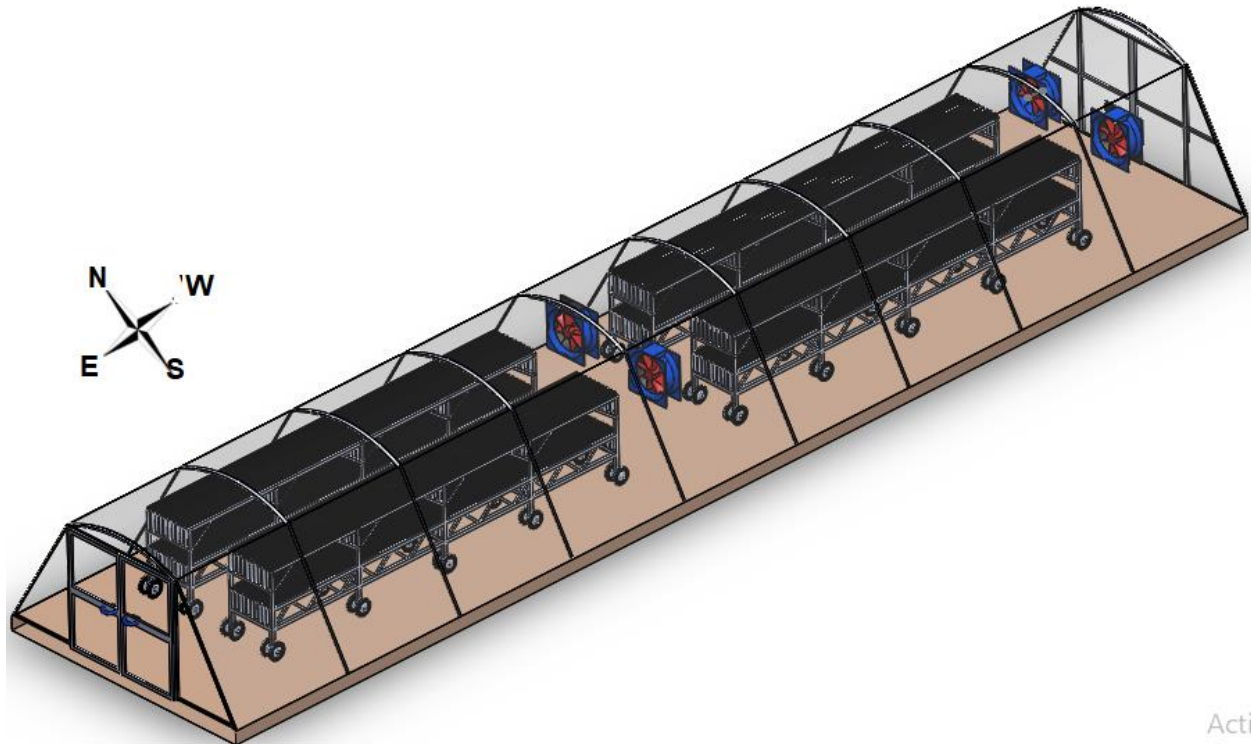


Figure 3.10: Schematic Diagram of the Designed Drying Chamber

The overall size of the drying chamber is $17.5\text{ m} \times 4\text{ m}$, with a height of 2 m . The overall collector area of the system is covered by a UV Polyethylene sheet with 200-micron thickness, that supported by a frame structure as shown in Figure 3.10. The front side of the system consists of axial fans to supply dry air to the chamber from the ambient and a double opening door with

1.75 m height and 1.94 m width, which is made up of a mild steel frame and the other part is covered by Polyethylene sheet. The double opening door provides an easy movement for the drying bed during the loading and unloading of the product. The backside of the chamber has axial fans to reject the humid air (water vapor) from the chamber to the surrounding air that maintains the relative humidity or specific humidity inside the dryer. A concrete foundation is used to anchor the frame structure, to support other components, and mostly to strengthen the stability of the drying chamber.

3.10.1 Drying Bed

Drying bed is a stable structure with different shape, used to load and support the weight of trays arranged in different patterns and the drying product. *4 movable drying beds with a fixed double layer* were considered, depending on the amount of the product per batch, properties of the product and the design result of drying chamber, as shown on figure 3.10, to make the loading and unloading process much easier and flexible. The main advantage of the movable drying bed is: *1)* the product is loaded inside the production unit which is easily transported to the drying chamber and *2)* after the drying process the bed will be transported toward the packaging unit to unload the dried product, which minimizes time, cost and energy required for the transportation of the product.

The total holding capacity of the bed is approximately 1200 kg of the product, which is 3200 pieces of charcoal dust briquette and its overall dimension is $L = 12\text{ m}$, $W = 0.77\text{ m}$ and $H = 1.3\text{ m}$. Hence the capacity of a single drying bed is 300 kg with both bed layer and the dimensions is $L = 6\text{ m}$, $W = 0.77\text{ m}$ and $H = 1.3\text{ m}$. For each drying bed, the number of tiers used is 20, and support structure used is 10 as shown in figure 3.11. A double tier per support structure is used to increase the stability of the bed, resist the weight of the product before drying, and optimize its motion flexibility during the loading period.

The model diagram of the movable drying bed and the arrangement of the bed inside the drying chamber are shown in figure 3.11.

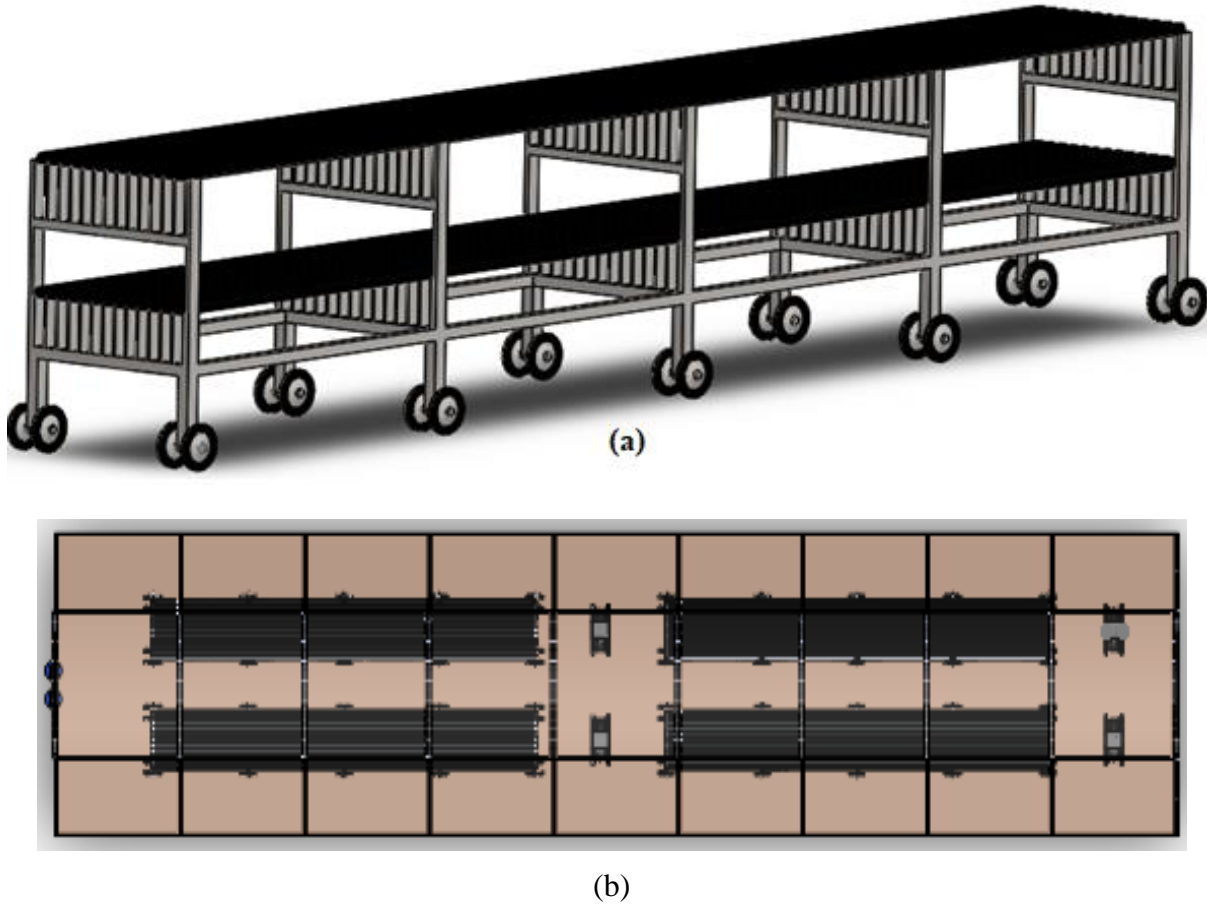


Figure 3.11: (a) Model Diagram of Drying Bed and (b) Layout of Drying Bed

The material used for the construction of the drying bed is aluminum, due to their lightweight and strong meshes, availability with low price, simplicity to weld, and mostly their significant resistance of rust and corrosion in a humidified environment.

3.10.2 Arrangement of Charcoal Briquette

The arrangement of charcoal briquette mainly depends on the physical property (its shape), heat transfer surface area, and type of convection (forced or natural). The face of the drying product is a hexagonal shape, which has a circular hole with a diameter of 1.5 cm and the overall dimension is shown in figure 3.5. The drying chamber operates based on the forced convection principle, where the hot air stream is forced to flow from the rare side toward the front side of the chamber, due to the arrangement of fans and drying bed as shown in figure 3.12 (a). The model diagram of charcoal briquette arrangement inside the chamber and on the bed is shown in figure 3.12.

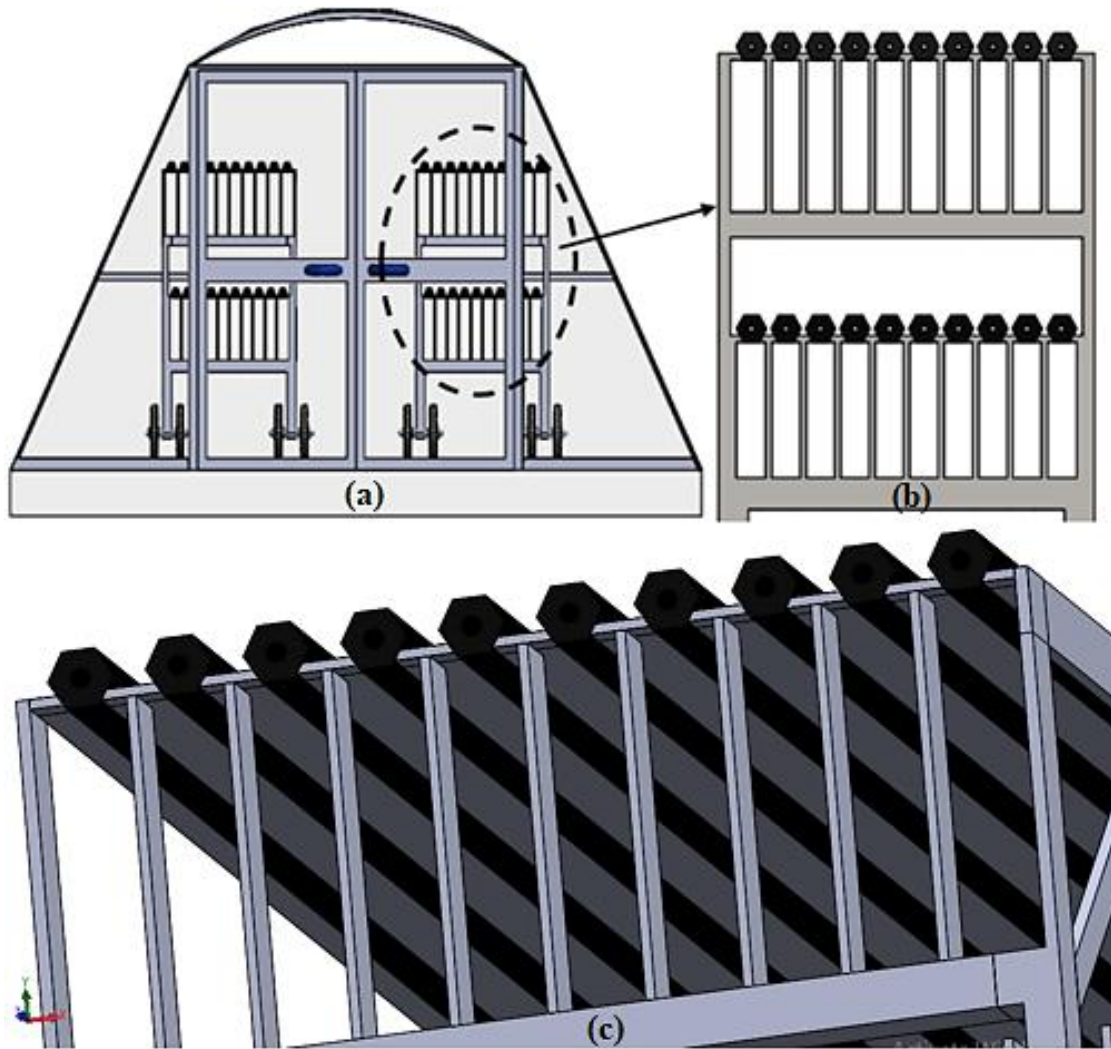


Figure 3.12: Arrangement of Charcoal Briquette

Due to this reason and the shape of the charcoal briquette, they will be arranged east-west direction, to maximize the surface contact of the hot air stream and the drying product. In a single drying bed, 800 pieces of charcoal briquette were arranged in two rows and ten columns, which aligned subsequently under each row and 2 cm gap between two columns. To maximize the heat transfer surface area and to minimize the surface contact area with support structure, all rows of the briquette were lifted and hung on a T-shaped framed structure as shown in figure 3.12 (b) and (c).

3.10.3 Frame Structure

The main purpose of the frame structure of the drying chamber is to support and stretch a polythene sheet cover for trapping the desired thermal energy of the sun and to maintain a constant solar

collector area. Among different shapes of a frame structure, a trapezoid with semi-cylindrical frame structure type is used to define the shape of the drying chamber, to prevent the problem of a semi-cylindrical shape oriented in East-West direction. The proposed frame structure receives solar radiation approximately 95% of the collector surface area during the sunshine hours of the site and its shape is shown in figure 3.9. The distance between the two structures is 1.75 m and the frame developed through 11 support structures. The material used for the construction of frame structure is Aluminum, due to their lightweight and strong meshes, availability with low price, simplicity to weld, and mostly their significant resistance of rust and corrosion in a humidified environment.

3.11 Design Dimensions

Designed dimensions of selected drying system will be summarized in table 3.4 as:

Table 3.4: Summary of Design Dimensions

Technical Design Dimensions	
Parameters	Technical Specifications
Drying System	Solar Tunnel Dryer
Type	Walk-In
Shape	Hemi-Cylindrical
Drying Bed	Fixed Double Layer
Bed Type	Movable
Number of Bed	4
Shape of Bed	T-Shape Framed Structure
Orientation	East-West
Design Parameters	
Drying Capacity per Batch (m_{bi})	1,120 kg
Amount of Water Removed (m_{wr})	448 kg
Initial Moisture Wet Base (M_i)	50 %
Final Moisture Wet Base (M_f)	10 %
Final Temperature of product (T_{bf})	50 °C
Final Temperature of Air (T_{af})	60 °C
Ambient Temperature (T_{am})	23 °C
Efficiency (η)	45 %

Sensible Heat for Charcoal Briquette ($Q_{s,b}$)	18.33 MJ
Sensible Heat for Water ($Q_{w,b}$)	63.504 MJ
Latent Heat for water ($Q_{l,w}$)	1,125.03 MJ
Total Heat Energy (Q_t)	1,206.86 MJ
Rate of Heat Energy (Q_r)	45.861 KW
Useful Thermal Energy (Q_u)	362.12 Whr
<i>Dimension and Area of Drying Chamber</i>	
Length (L_{dc})	17.5 m
Width (W_{dc})	4 m
Height or Radius ($H_{dc} = R_{dc}$)	2 m
Area (A_{dc})	110 m ²
Floor Area (A_{fac})	70 m ²
<i>Dimension and Area of Drying Bed</i>	
Length (L_{db})	6 m
Width (W_{db})	0.77 m
Height (H_{db})	1.3 m
Area (A_{db})	12 m ²
Briquette Surface Area (A_{bs})	99.5 m ²
<i>Psychrometry Operation Conditions</i>	
Initial Specific Humidity (w_i)	0.011
Final Specific Humidity (w_f)	0.025
Initial Relative Humidity (RH_i)	63.4 %
Final Relative Humidity (RH_f)	100 %
Air Flow Rate for Adiabatic Humidification (\dot{m}_a)	1.3572 kg/s
Air Flow Rate for Sensible Heating (\dot{m}_a)	0.6433 kg/s
Drying Rate	0.019 kg/s

CHAPTER 4

MATHEMATICAL MODELING AND ANSYS SIMULATION

The proposed drying system has two main sub-systems, the solar air heater to heat the air and the solar tunnel dryer (greenhouse effect) to dry charcoal dust briquette. The simulation of this drying system includes two parts; *part 1*: presents the mathematical modelling of SAH and *part 2*: presents the ANSYS Fluent Simulation of STD. The main input parameters for both systems are ambient temperature, which was determined from NASA data on the internet and solar radiation, which was estimated by using Angstrom-Prescott Empirical Model. Also, the geographical location and weather condition of the site was used.

4.1 Mathematical Modeling of SAH

The transient thermal performance of the solar collector is evaluated by applying energy balance on its components. The year-round transient analysis of the collector model is performed inserting given solar radiation data and solar collector parameters into the set of model equations described below. The temperature variations of the collector panel, the air stream leaving the collector and the glass cover are estimated for each representative day of each month [53-54]. (ANNEX (A))

4.1.1 Energy Balance of Glass Cover

The small thickness of the cover makes it reasonable to consider a uniform glass temperature distribution through the whole part of the glass cover. Also by considering constant properties of glass material, the governing equation can be derived from an energy balance in a differential volume of thickness (t_g), area (A_c) and time variation over period of the day. Thermal energy absorbed and lost by glass cover is shown by figure 4.1:

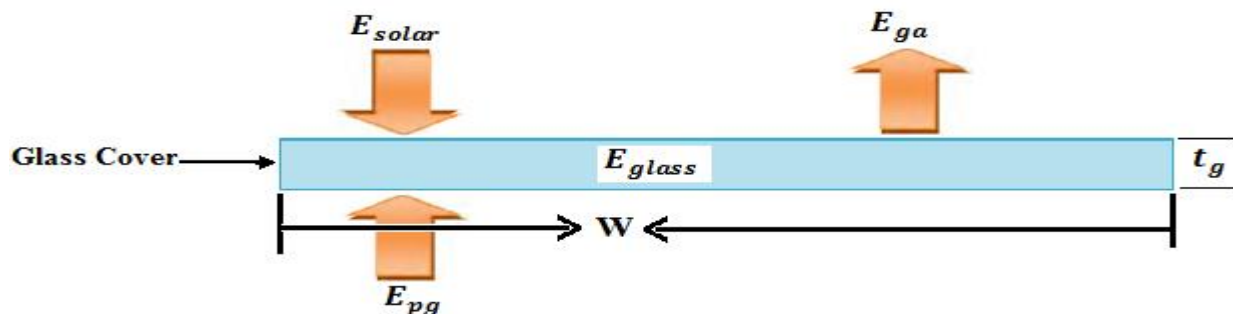


Figure 4.1: Heat Energy Balance of Glass Cover.

Making energy balance on the glass cover, assumed single glazed collector, its empirical equation at any time $(t + \Delta t)$ is determined from data at time (t) and energy absorbed and lost from the glass cover during the time interval (Δt) as follows:

$$(m_g C_{pg}) \frac{dT_g}{dt} = A_c I_N \alpha_g + A_c U_{pg} (T_{p0} - T_{g0}) - A_c U_{ga} (T_{g0} - T_{a0}) \text{----- (4.1)}$$

The temperature of glass cover derived from the energy balance of the glass zone at any time $(t + \Delta t)$, energy absorbed and lost from the glass cover during the given time interval (Δt) . Upon integrating energy balance equation (4.1), yields the equation of transient temperature (T_{g1}) variation of glass cover, after time interval of (Δt) is given as:

$$T_{g1} = \left[\begin{aligned} & \left[\frac{A_c I_N (1 - \tau_g) \Delta t}{(m C_p)_g} + \left\{ 1.0 - \left(\frac{A_c U_{pg}}{(m C_p)_g} + \frac{A_c U_{ga}}{(m C_p)_g} \right) \Delta t \right\} T_{g0} \right] \\ & + \left[\left(\frac{A_c U_{pg} \Delta t}{(m C_p)_g} \right) T_{p0} + \left(\frac{A_c U_{ga} \Delta t}{(m C_p)_g} \right) T_{a0} \right] \end{aligned} \right] \text{----- (4.2)}$$

Where: $\alpha_g = (1 - \tau_g)$, α_g and $\tau_g =$ is absorptivity and transitivity of glass.

4.1.2 Energy Balance on Absorber Plate

Applying the heat energy balance for the absorber plate zone; taking the constant thermo-physical properties of the absorber plate material and considering the solar irradiance on the absorber plate zone in the solar collector control volume, the radiation and convection heat transfer between the absorber and the glass cover, the conduction and convection heat transfer between the absorber and the insulation zone and the heat transfers by radiation and convection with the fluid flow (air stream), gives the relation below. Thermal energy absorbed and lost by absorber plate is shown by figure 4.2:

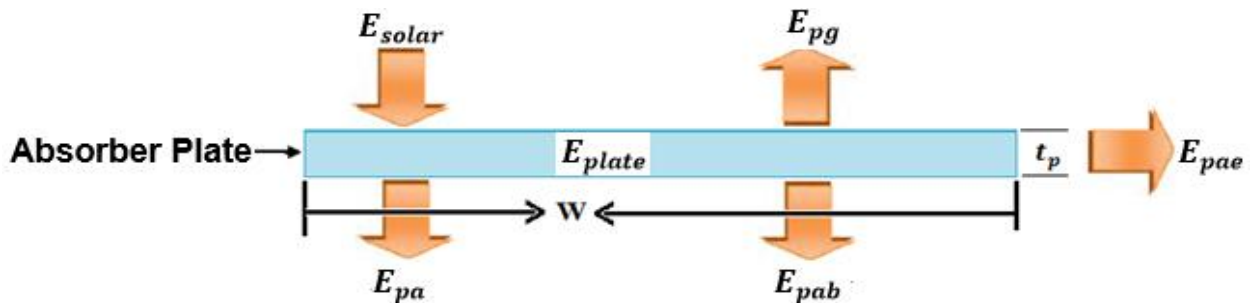


Figure 4.2: Heat Energy Balance of Absorber Plate.

The energy balance of plate at any time $(t + \Delta t)$ is estimated from energy absorbed during the time interval (Δt) and the energy losses at the same time interval given as:

$$(m_p C_{pp}) \frac{dT_p}{dt} = \left[A_c I_c - A_c U_{pg}(T_{p0} - T_{g0}) - A_c U_{pa} \left[T_{p0} - \frac{T_{ao0} + T_{ai0}}{2} \right] - [A_c U_{pab}(T_{p0} - T_{a0}) + A_l U_{pae}(T_{p0} - T_{a0})] \right] \quad (4.3)$$

The absorber plate temperature T_{p1} at any time $(t + \Delta t)$ can be determined from conditions at time t and energy absorbed during the time interval Δt and the energy losses at the same time interval (Δt) . Upon integrating energy balance equation (4.3), yields the equation of transient temperature (T_{p1}) variation of absorber plate, after time interval of (Δt) is given as:

$$T_{p1} = \left[\begin{aligned} & \left(\frac{A_c I_c \Delta t}{(m C_p)_p} \right) + \left(\frac{A_c U_{pg} \Delta t}{(m C_p)_p} \right) T_{g0} + \left(\frac{A_c U_{pa} \Delta t}{2(m C_p)_p} \right) T_{ao0} \\ & + \left(\frac{A_c U_{pab} \Delta t}{2(m C_p)_p} \right) T_{ai0} + \left(\frac{A_c U_{pab} \Delta t}{(m C_p)_p} + \frac{A_l U_{pae} \Delta t}{(m C_p)_p} \right) T_{a0} \\ & + \left\{ 1.0 - \left(\frac{A_c U_{pg} \Delta t}{(m C_p)_p} + \frac{A_c U_{pa} \Delta t}{(m C_p)_p} + \frac{A_c U_{pab} \Delta t}{(m C_p)_p} + \frac{A_l U_{pae} \Delta t}{(m C_p)_p} \right) \right\} T_{p0} \end{aligned} \right] \quad (4.4)$$

4.1.3 Energy Balance on Air Stream

Figure 4 shows the energy balance in a control volume of the working fluid (air) in a flat-plate solar air heater collector. Taking in consideration the change in total energy with time and the total heat transferred into the fluid control volume, the energy balance under constant properties of the working fluid can be written as:

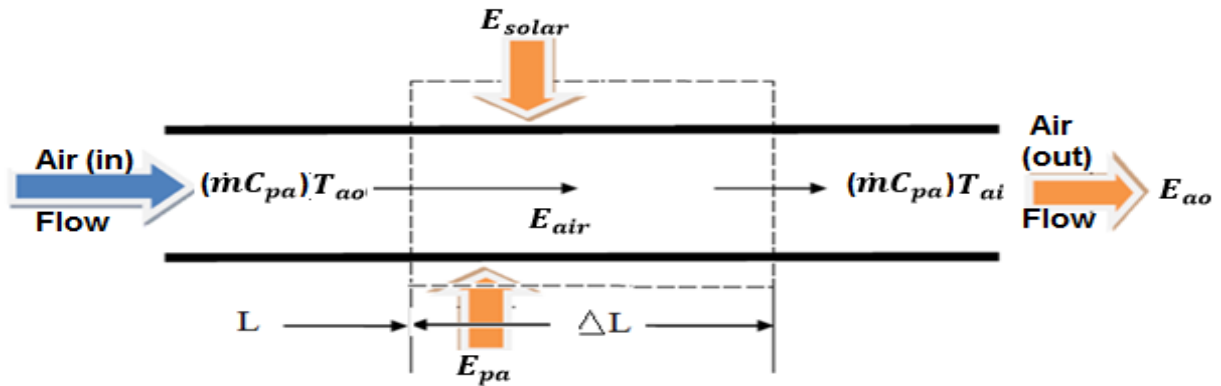


Figure 4.3: Energy balance of the working fluid in flat-plate solar collector

$$(mC_p)_a \frac{dT_{ao}}{dt} = A_a I_N \alpha_a \tau_g + A_a U_{pa} \left(T_p - \frac{T_{ao} + T_{ai}}{2} \right) - (mC_p)_a (T_{ao} - T_{ai}) \quad \text{--- (4.5)}$$

Air stream temperature (T_{ao1}) at any time ($t + \Delta t$) can be determined from data at time t and energy absorbed during the time interval (Δt). Upon integrating energy balance equation (4.5), yields the equation of transient temperature (T_{ao1}) variation of air stream, after time interval of (Δt) is:

$$T_{ao1} = \left[\left[\left(1.0 - \left(\frac{A_a U_{pa}}{(2mC_p)_a} + \frac{(\dot{m}C_p)_a}{(mC_p)_a} \right) \Delta t \right) T_{ao0} + \left(\frac{(\dot{m}C_p)_a}{(mC_p)_a} - \frac{A_a U_{pa}}{(2mC_p)_a} \right) \Delta t T_{ai0} \right] + \left[\frac{(A_a I_N \alpha_a \tau_g \Delta t)}{(mC_p)_a} + \left(\frac{A_a U_{pa} \Delta t}{(mC_p)_a} \right) T_{p0} \right] \right] \quad \text{--- (4.6)}$$

4.1.4 The Heat Transfer Correlations

At some typical location on the plate solar energy of amount (S) is absorbed by the plate is equal to the incident solar radiation reduced by optical losses. This absorbed energy (S) is distributed to thermal losses and to useful energy gain. Thermal losses from the plate through the glass cover and the insulation (edge and back losses) are take places through conduction, convection and radiation.

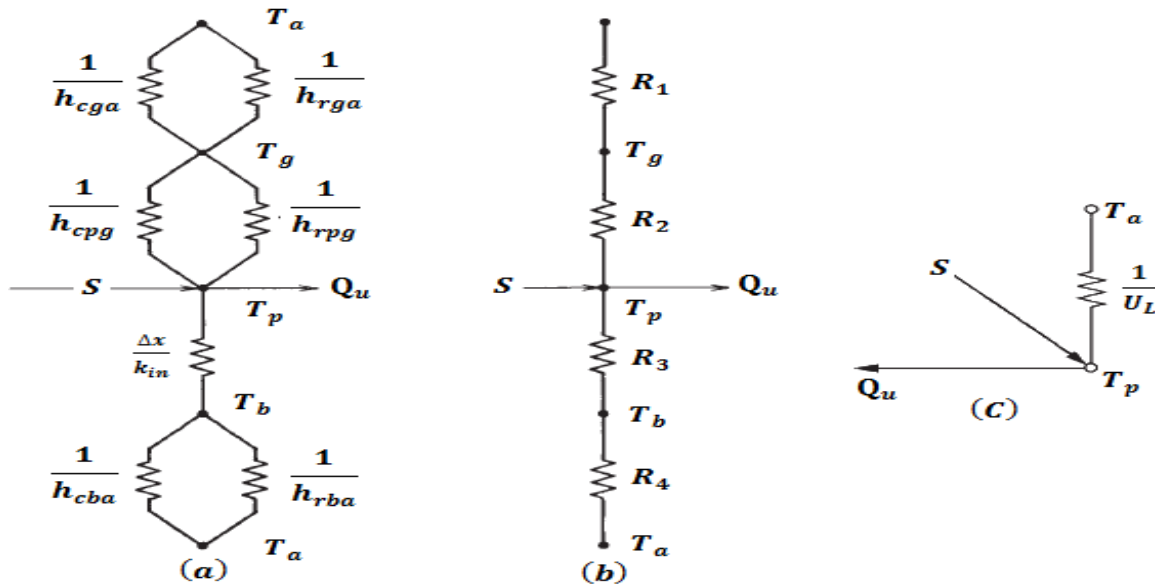


Figure 4.4: Thermal Resistance Networks of a Flat-Plate Collector

i) Top Loss Coefficients

The energy loss through the top is the result of convection and radiation from glass cover to the ambient and between absorber plate and glass cover. The steady-state energy transfer between the plate at (T_p) and the cover at (T_g) is equal to the energy lost to the surroundings from the top cover.

a) From Absorber Plate to Glass Cover

The heat transfer coefficient from absorber plate to the glass cover includes the thermal energy loss from plate to glass and to air stream.

⇒ **From plate to glass cover (U_{pg}):** the overall heat transfer coefficient from the plate to the glass by convection and radiation is given by:

$$U_{pg} = \left[0.06 - 0.017 \frac{\beta}{90} \right] \frac{K_a}{L} (G_{rL})^{\frac{1}{3}} + [\varepsilon_{pg} \sigma (T_p^2 + T_g^2) (T_p + T_g)] \text{ --- (4.7)}$$

⇒ **From plate to air stream (U_{pa}):** the heat transfer coefficient of the air is defined as:

$$U_{pa} = 0.664 \frac{K_a}{L} \left[\frac{P_r G_{rL} \cos \beta}{P_r + 0.9524} \right]^{0.25} \text{ --- (4.8)}$$

➤ The volume expansion coefficient β' is given by:

$$\frac{1}{\beta'} = \frac{(T_p + T_g)}{2} \text{ --- (4.9)}$$

➤ The Grashof number (G_{rL}) is defined by:

$$G_{rL} = \frac{g \beta' (T_p - T_g) L^3}{\nu^2} \text{ --- (4.10)}$$

➤ The overall emittance factor (ε_{pg}) for the absorber plate and the glass cover is obtained from the relation:

$$\varepsilon_{pg} = \left[\frac{1}{\varepsilon_p} + \frac{1}{\varepsilon_g} - 1 \right]^{-1} \text{ --- (4.11)}$$

➤ Prandtl number (P_r) is defined by:

$$P_r = \frac{\nu_a}{\alpha_a} = \frac{C_{pa} \nu}{K_a} \text{ --- (4.12)}$$

➤ All properties in the above equation are evaluated at the film temperature T_f given by:

$$T_f = \frac{(T_{ao} + T_{ai})}{2} \text{----- (4.13)}$$

⇒ **From glass to ambient air (U_{ga}):** the total heat transfer coefficient from collector cover to ambient includes losses by convection and radiation, can be simplified as:

$$U_{ga} = h_c + h_r \text{----- (4.14)}$$

→ *Convective heat transfer coefficient (h_c):* of convective heat loss from collector cover to the ambient can be expressed as:

$$h_c = 2.8 + 3V_w \text{----- (4.15)}$$

→ *Radiation heat transfer coefficient (h_r):* of radiation heat loss from collector cover to the ambient can be expressed as:

$$h_r = E_g \sigma \left\{ \frac{(T_g + 273)^4 - (T_{sky} + 273)^4}{T_g - T_a} \right\} \text{----- (4.16)}$$

The sky temperature T_{sky} is given by:

$$T_{sky} = T_a - 6 \text{----- (4.17)}$$

The effective top heat transfer coefficient from plate to ambient is given by:

$$U_t = U_{pg} + U_{pa} + U_{ga} \text{----- (4.18)}$$

ii) Back Loss Coefficient

The energy loss through the bottom and edge of the collector is represented by two series resistors, $R3$ and $R4$, in Figure 6, where $R3$ represents the resistance to heat flow through the insulation by conduction and $R4$ represents the convection and radiation resistance to the environment. Back heat loss from the plate to the surrounding through bottom and edge insulation.

⇒ **Bottom loss heat coefficient (U_{ba}):** the total heat transfer coefficient from bottom insulation to ambient, can be simplified as:

$$U_{ba} = \left[\frac{L_{in}}{K_{in}} + \frac{1}{h_b} \right]^{-1} \text{----- (4.19)}$$

Where: the value of radiation heat loss is neglected because, its value is much lower than the heat loss value by conduction and convection.

⇒ **Edge loss heat coefficient (U_{ea}):** Energy lost from the side of the collector casing may be taken to have exactly the same value as that from the back, if the thickness of the edge insulation is the same as that of the back insulation (Tabor, 1958). The edge loss is given as:

$$U_e = U_b \left(\frac{A_e}{A_c} \right); A_c = A_b \text{ ----- (4.20)}$$

The effective back heat transfer coefficient from plate to ambient is given by:

$$U_b = U_{ba} + U_{ea} \text{ ----- (4.21)}$$

4.1.5 Useful Energy Output

The useful energy output per unit time of a collector area (A_c) is the difference between the final and the initial thermal energy states of air stream, which defined as:

$$Q_u = \dot{m}_a C_{pa} (T_f - T_i) \text{ ----- (4.22)}$$

Where: mass flow rate (\dot{m}_a) and specific heat capacity of air is constant and the temperature of air stream at final state (T_f) and at initial state T_i .

4.1.6 Thermal Efficiency

A measure of collector performance is the collection efficiency, defined as the ratio of the useful gain thermal energy to the incident solar radiation on the collector area over the same specified time period. Therefore the instantaneous efficiency is given by:

$$\eta = \frac{Q_u}{A_c I} \text{ ----- (4.23)}$$

Where, η = is collector efficiency, A_c = projected or absorber area and I = is incidence solar radiation of the site.

4.2 ANSYS Fluent Simulation of STD

4.2.1 Geometry Creation

The geometry of basic drying chamber was scale dawn by; 20% (width and height of face surface) and 50% (length of side surface) to minimize the challenge of meshing and fluent iteration. Three

models were developed using SOLIDWORKS 2018 and imported to ANSYS Fluent to simulate temperature, velocity and pressure distribution inside the drying chamber, as shown on figure 4.5. All models have equal sized four inlet (0.03 m long and 0.0042 m height), to supply hot air into the chamber and two outlet (0.03 m long and 0.0084 m height), to ventilate the humid air into the surrounding. The 3D geometry diagram of all drying chamber model with and without drying product is presented on figure 4.5

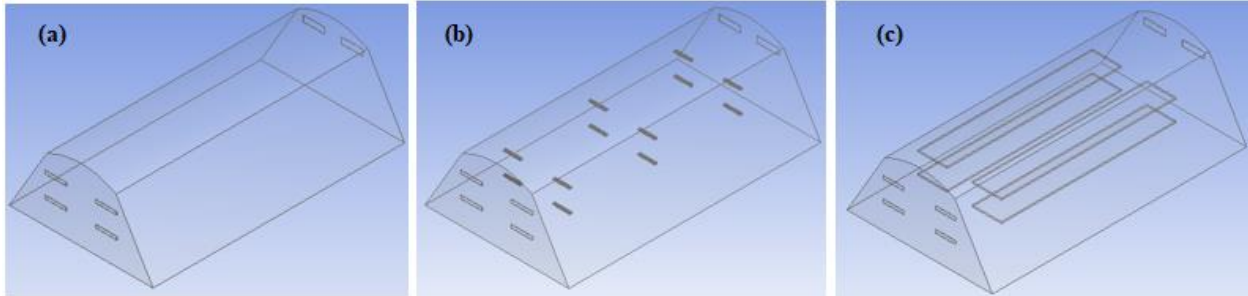


Figure 4.5: Model of the Drying Chamber

Model 1: on figure 4.5 (a) presents the STD without a drying product to evaluate the distribution of temperature, velocity and pressure inside the chamber and to use it as a reference for the simulation result analysis of other geometry's. Also, the result of this model will be the base to use it for other kind of drying product.

Model 2: on figure 4.5 (c) presents the STD and the overall amount of drying product, where its shape replaced by a rectangular shape with equal dimension of heat transfer surface area to reduce the challenges on meshing and fluent simulation. There are four rectangular geometry inside the drying chamber and arranged on both drying beds.

Model 3: on figure 4.5 (b) presents the STD and few number of drying product sample with a real shape. The sample includes 120 charcoal briquettes and organized into 12 rows with equal size. Inside the chamber, the rows arranged at the front, middle and back side of each layers of both drying beds.

All geometry have four hot air inlets and two humid air outlets with the same size and the final dimension applied for the simulation is presented by table 4.1. The preceding step is mesh generation.

Table 4.1: Final Dimension of Drying Chamber and Drying Product

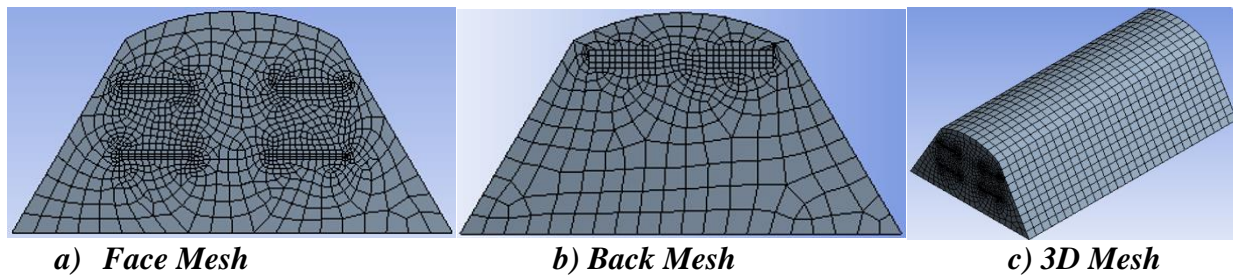
Scaled Dimension of Drying Chamber and Drying Product			
Geometry	Dimension		
	Length (m)	Width (m)	Height (m)
Drying Chamber	0.35	0.2	0.1
Drying Product on Fig. 4.1 (b)	0.003	0.025	0.002
Drying Product on Fig. 4.1 (c)	0.24	0.04	0.002

4.2.2 Meshing

The irregular shape of STD model can be converted into more recognizable elements or volumes using meshing techniques to improve the simulation quality. After the creation of each model geometry and differentiating fluid and solid domain under Design Modeler module, the computational domain was discretized by mesh generation. The linear Hex Dominant meshing method were selected and the element types are set to all Quad to maximize the accuracy of the final result. Simultaneously, edgy sizing and face meshing were applied to minimize the number of elements and nodes, as well as to improve the profile of the elements, which decreases the rate of convergence and gave a better simulation result.

Model 1 Meshing: presents the type of mesh generated for the STD geometry without the drying product and the heat transfer surface boundaries. The profile of the elements was refined by generating 4 different edgy sizing on all edgy based on their length and face meshing on the bottom and top surface of the model.

Figure 4.6 shows the final face meshing, back meshing and 3D meshing of model 1 (STD) used for the simulation:

**Figure 4.6:** Meshing of Model 1

The final result of meshing indicates that, the size of the element is 0.002m, the total number of elements are 13,916 and the total number of nodes are 11,758 with the maximum Skewness of 0.99994. The heat transfer surface boundaries of air domain are 4 inlet, 2 outlet, 5 cover walls and 1 floor wall.

Model 2 Meshing: presents the type of mesh generated for the drying chamber air domain geometry and the total number of drying product solid domain with rectangular geometry features and the heat transfer surface boundary of the overall system. Also, the elements profile of modified drying product (rectangular geometry) was refined only by generating 3 different edgy sizing on each edges, based on their length. In the case of this model 2, the mesh editing techniques used for the air domain drying chamber geometry, is similar to model 1. Figure 4.7 shows the final face meshing, side meshing and 3D meshing of model 2 (modified charcoal dust briquette geometry) used for the simulation:

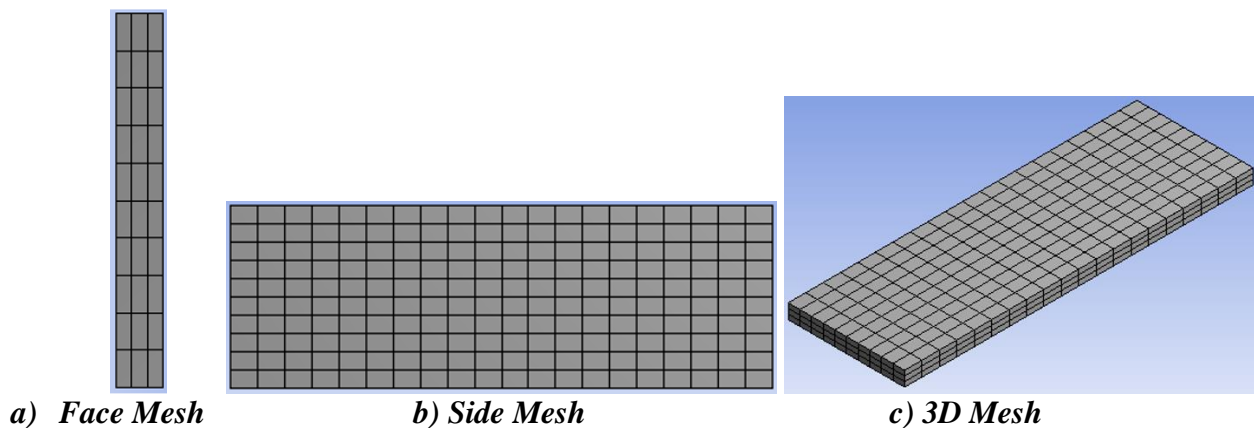


Figure 4.7: Meshing of Model 3

After editing and refining the mesh of modified drying product, the size of the element is 0.004m, the number of elements are 20,800 and the number of nodes are 27,848 with the maximum Skewness of 0.99978. For the overall model 2, the total number of elements are 34,716 and the total number of nodes are 38,606. The heat transfer surface boundaries are 4 inlet, 2 outlet, all modified briquette walls (front, back, top and bottom surfaces), 5 cover walls and 1 floor wall.

Model 3 Meshing: presents the type of mesh generated for the drying chamber air domain geometry and a sample of drying product (charcoal dust briquette) solid domain with its real geometry features and the heat transfer surface boundary of the overall system. The drying product elements profile was refined by generating 2 different edgy sizing depending on their length size

and face meshing on the front and back surface of the model. In the case of this model 3, the mesh editing techniques used for the drying chamber or air domain, is similar to model 1. Figure 4.8 shows the final face meshing, side meshing and 3D meshing of model 3 (charcoal duct briquette) used for the simulation:

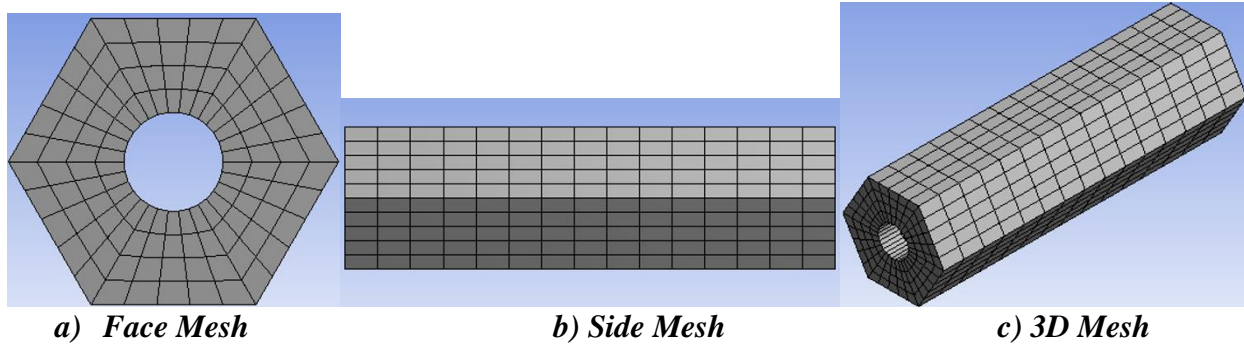


Figure 4.8: Meshing of Model 3

After editing and improving the mesh of drying product, the size of the element is 0.005m, the number of elements are 216,000 and the number of nodes are 288,000 with the maximum Skewness of 0.99983. For the overall model 3, the total number of elements are 229,916 and the total number of nodes are 299,758. The heat transfer surface boundaries are 4 inlet, 2 outlet, all briquette walls (outer and inner holes surfaces), 5 cover walls and 1 floor wall.

4.2.3 Analysis Setup

a) Operating Conditions

Turbulence Model: A forced convection flow field usually includes fans or blowers or ventilation systems to drive the fluid throughout the chamber, which creates a turbulence movement due to the high flow rate and the heat transfer interaction in the flow field. This indicates that, the proposed drying system categories under turbulence flow. A mathematical model selected to predict the effects of turbulence inside the drying chamber was **Realizable $k - \epsilon$ (epsilon)** (the transport model of turbulent kinetic energy (κ) and its dissipation speed (ϵ)) with **Enhanced Wall Treatment**, because of their high performance in more complex and main flow fields, accurately prediction of spreading rate, high convergence rate and comparatively low computational memory requirements.

Radiation Model: Solar radiation mainly depends on time, day and month of the year, the mean solar time (GMT), geographical location, weather conditions and STD or mesh orientation. The

DO model can solve the radiative transfer equation (RTE) for a finite number of discrete solid angles, each associated with a vector direction and solve the irradiance at semi-transparent walls. Due to this, the discrete ordinates (DO) radiation model was used to simulate the effect of solar radiation inside the drying chamber. In order to simulate solar radiation; longitude 32.6° , latitude -26° , +2 GMT and Fear weather condition of Maputo city is used. The orientation of the mesh is set as: **North** on *negative X-direction* and **East** on *positive Z-direction*. Solar radiation mainly depends on the season of the year, due to this the simulation was performed on two months with higher and lower monthly solar radiation for their representative days and also, for 12 hours of the day including the maximum and minimum radiation encounters.

Species Transport: Species transport model used to represent the mixture of two different types of fluid and to determine the mass fraction of each type inside the system. In this case, it is used to specify the mixture of dry air and water vapor. This simulation presents only heat transfer model, where mass transfer model is not included, because of this phenomenon there is no moisture transfer between the drying product and moist air. Due to this, the mass fraction of each species throughout the system is constant and there is no moisture diffusion on the solid walls. The mass fraction of moist air at the inlets of drying chamber is **0.0101**.

Table 4.2: The Summary of Operating Conditions

Summary of Operating Conditions	
Operating Conditions	Governing Equation
Solver	3D Simulation Implicit Formulation Pressure Based Absolute Velocity Formulation Steady State Analysis
Gravity	-9.81 m/s^2 ... <i>Y - axis</i>
Energy Equation	On
Viscose Model	Realizable $k - \varepsilon$ Model Enhanced Wall Treatment
Radiation Model	Discrete Ordinate (DO)
Species Transport	On

The executive summary of operating conditions of the analysis is discussed in table 4.2.

b) Boundary Conditions

In order to obtain the desired result of the simulation, the boundary condition of the system must be defined carefully. The type of heat interaction between the boundaries with its appropriate values, the thickness of each boundary and type of material with their respective property must be defined. Model 2 and model 3 contains inlet, outlet, briquette-wall, cover-wall and floor-wall boundary conditions. Finally, model 1 contains inlet, outlet, cover-wall and floor-wall boundary conditions.

Table 4.3: Summary of Boundary Conditions

Summary of Boundary Conditions			
Boundary Conditions	Parameters	Values	Material
Inlet	Mass Flow Rate	0.017275 Kg/s	Moist Air
	Temperature	338 K	
	Mass Fraction	0.0101	
Outlet	Pressure Outlet	0	Moist Air
	Mass Fraction	0	
Briquette-Wall	Wall Thickness	0.002m	Charcoal Dust Briquette
	Emissivity	0.96	
	Absorptivity	0.8	
	h	13.9 W/m ² · K	
Cover -Wall	Wall Thickness	0.0002m	Semi-Transparence Polyethylene
	Emissivity	0.94	
	Absorptivity	0.02	
	h	13.9 W/m ² · K	
Floor-Wall	Wall Thickness	0.015m	Concrete
	Emissivity	0.92	
	Absorptivity	0.65	
	h	13.9 W/m ² · K	

The executive summary of boundary conditions of the analysis, the parameters used to define the condition with their value and the type of material is discussed in table 4.3.

4.2.4 Solution Method

The solution method selected to perform the simulation is Pressure-Velocity Coupling method for all models. Also, the spatial discretization methods used for the analysis of pressure is Second Order, momentum, energy and water vapor (h₂o) is Second Order Upwind and turbulent kinetic energy, turbulent dissipation rate and discrete ordinate is First Order Upwind in each geometry models. The type of scheme, gradient and initialization applied for each model is summarized on the table 4.4.

Table 4.4: The Type of Scheme, Gradient and Initialization of each Model

Type of Scheme, Gradient and Initialization			
	Geometry Model		
	Model 1	Model 2	Model 3
Scheme	SIMPLE	SIMPLE	SIMPLIC
Gradient	Green-Gauss Cell Based	Green-Gauss Cell Based	Least-Squares Cell Based
Initialization	Standard	Standard	Standard

CHAPTER 5

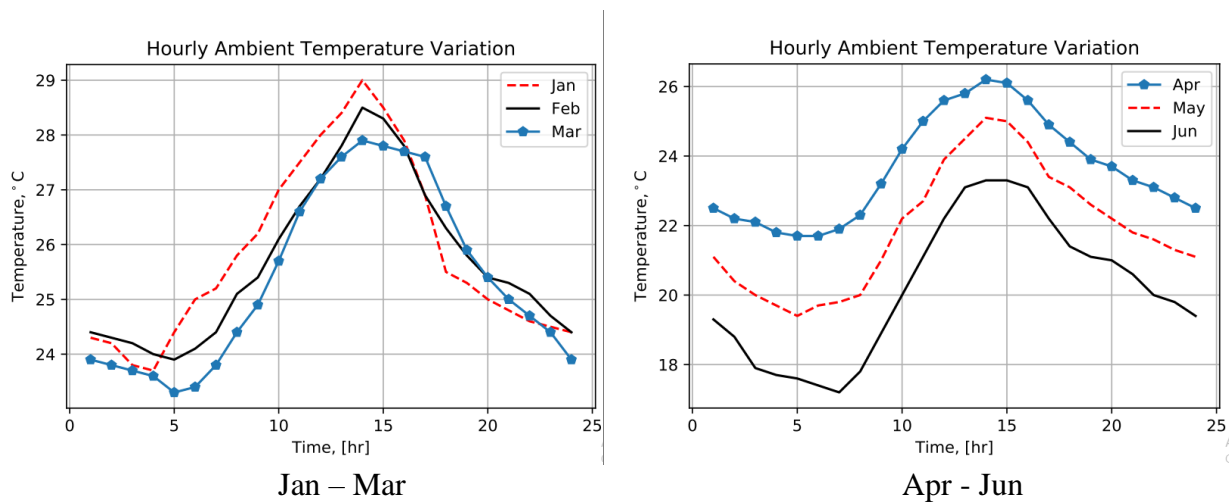
RESULT DISCUSSION

The computational fluid dynamics analysis of the proposed drying system includes ambient temperature variation, estimation of hourly solar radiation of the site, outlet air temperature of solar air heater, and the profile of temperature, velocity, and pressure distribution and variation inside the solar tunnel dryer. The result discussion of this CFD analysis includes three major parts. *Part 1:* is the result illustration of the weather condition of the location and the mathematical prediction model of monthly average hourly global radiation of Microsoft Excel analysis software. *Part 2:* is MatLab programming software simulation result discussion on a numerical model of SAH to determine the outlet air temperature. *Part 3:* is the discussion of the SOLIDWORK model result and ANSYS Fluent Simulation software result of temperature, velocity, and pressure distribution, and variation profile of STD.

4.1 Solar Radiation and Ambient Temperature

4.1.1 Ambient Temperature

The monthly average hourly ambient temperature data used for the Numerical (mathematical) Model Algorithm analysis of SAH of Maputo, Mozambique was determined from NASA data on the internet based on the geographical location of the site. Figure 5.1 presents the hourly variation of average ambient temperature throughout 24 hours of the day, for each month's representative day of the year. Ambient temperature is used as input parameters of SAH, because of thermal interaction with the surrounding.



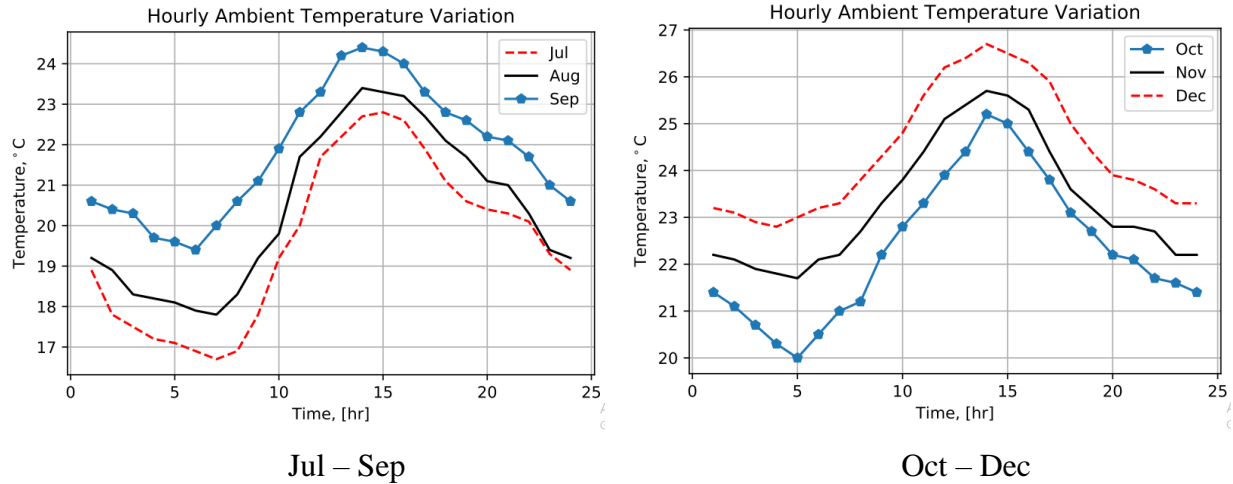


Figure 5.1: Hourly Ambient Temperature Variation

Figure 5.1 indicates that the maximum ambient temperature is found between 10 AM up to 4 PM and the minimum value is observed at a sunrise, a sunset, and throughout night hours of the day for each month. The profile of hourly variation shows that, the value of temperature increases from morning up to mid-day, where it reaches the maximum point and then decreases until sunset. The higher value is countered in January and the lower value is countered in June month. Throughout the year the hourly variation of ambient temperature lays in the range of 16°C and 30°C, which indicates that *the rate of variation* between each hour of the day, starting from sunrise up to sunset is *very low*.

4.1.2 Estimated Hourly Solar Radiation

The monthly average hourly global, beam, and diffuse radiation data used for the Mathematical Model Algorithm analysis of SAH and ANSYS Fluent simulation of STD is estimated using Angstrom-Prescott Empirical Model. The solar radiation is predicted based on monthly average daily sunshine hours of Maputo from NASA data available on the internet. The estimation analysis is modeled and analyzed using Microsoft Excel and the graphs are plotted using Python Programming software. The graphical result of solar radiation prediction for 24 hours on the representative day of each month is displayed in figure 5.2.

The Result of the monthly average hourly global radiation estimation model reveals that the maximum values of global radiation are counter in the range of 11 AM up to 1 PM and the minimum values on night hours of the day for each month. The profile of hourly variation of solar

radiation indicates that its value increases starting from a sunrise hour up to the maximum point at mid-day and then decreases up to sunset hour.

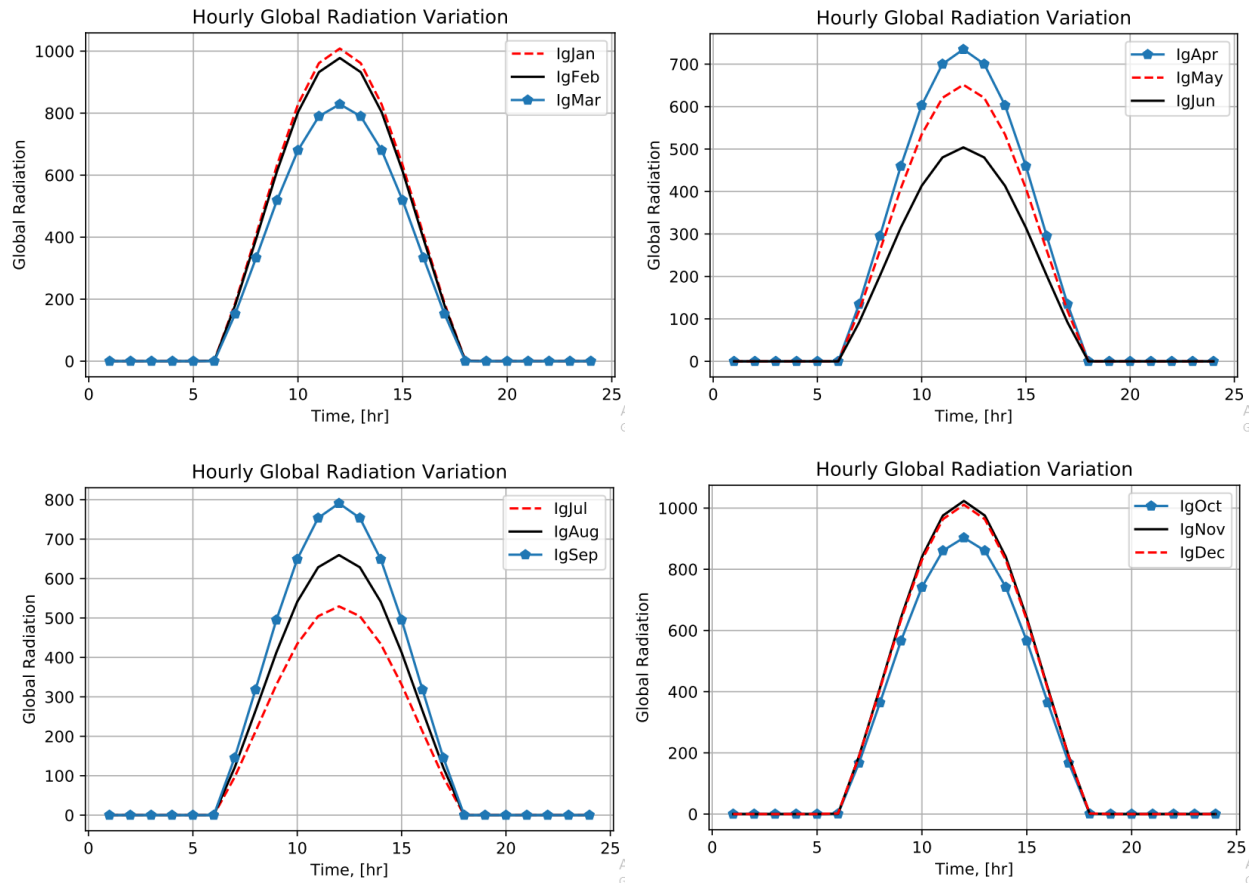


Figure 5.2: Hourly Global Radiation Variation

As figure 5.2 presents, the higher value of global radiation is in countered in November month, where the daily maximum is 1023.55 W/m^2 at 12 PM and the minimum is 188.33 W/m^2 at 7AM and the lower value is in countered on June month, where the daily maximum is 503.98 W/m^2 at 12 PM minimum is 91.6 W/m^2 at 7AM. For 6 months of the year, the values of global radiation are greater than 800 W/m^2 for 5 hours in January, February and from October up to December as well as in March for 3 hours. Also, in June and July, its value is below 550 W/m^2 throughout the day and the rest of months lay between these two values.

4.2 Result of MatLab Simulation of SAH

The MatLab code was written for a single air pass SAH mathematical model developed based on the forward difference method. The result of the estimated global, beam (direct), and diffuse

radiation and the NASA data of ambient temperature is used as thermal source input parameters. The material property of the selected SAH, calculated values of solar angles, collector dimensions, and air mass flow rate, was considered based on the value of outlet air temperature. The result discussion of MatLab Simulation includes *Hourly Variation of Temperature, Useful Energy Output, and Efficiency*.

4.2.1 Hourly Temperature Variation

The constant mass flow rate of air 1.3572 Kg/s, time step per iteration is 60 and the initialization temperature of plate $T_p = T_{am} + 1$, outlet air $T_{ao} = T_{am} + 0.5$, glass cover $T_g = T_{am} + 0.25$ and inlet air $T_{ai} = T_{am}$ for 10,000 iterations is used in the simulation. The graphical result (exit air temperature in Celsius Vs time in hours) of MatLab simulation for 24 hours on the representative day of each month is displayed in figure 5.3.

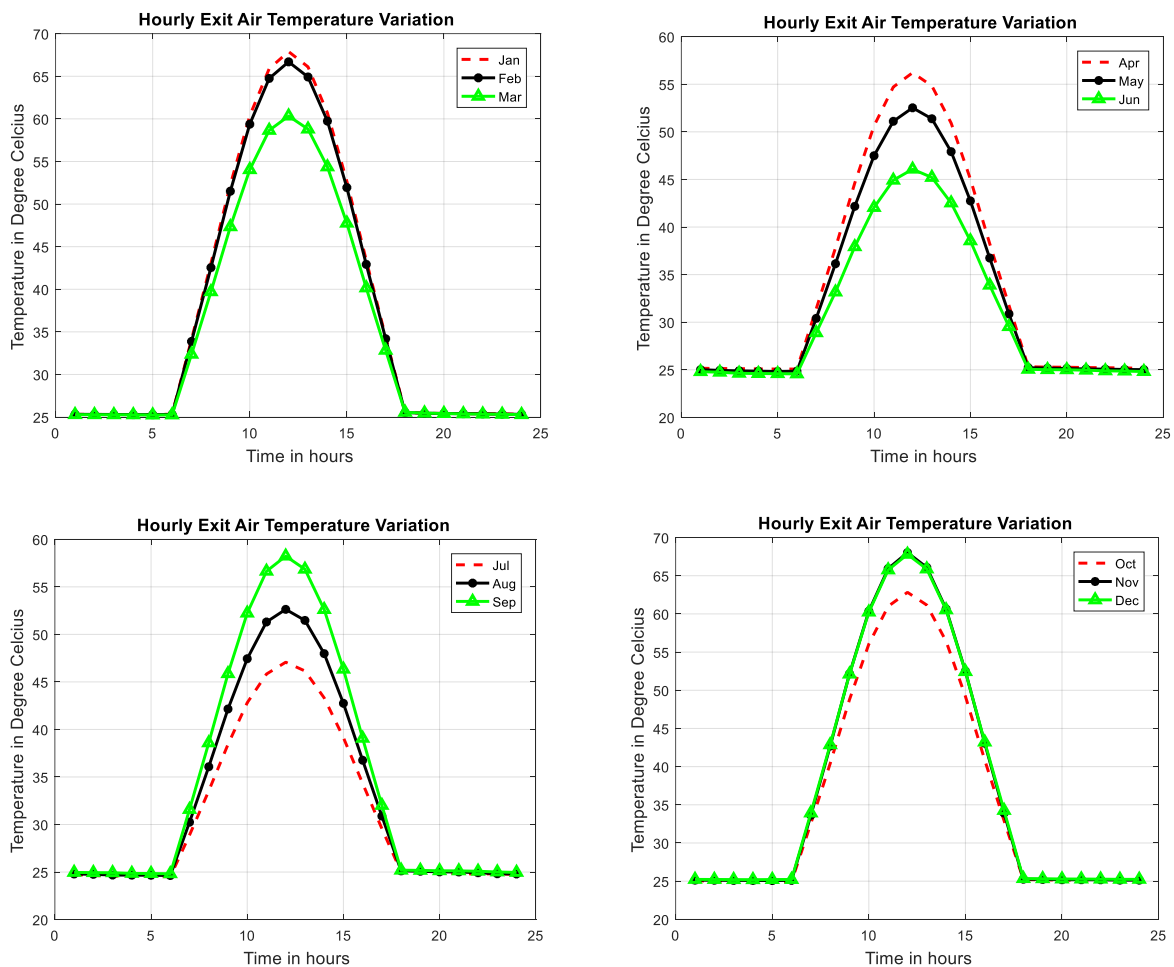


Figure 5.3: Hourly Global Radiation Variation

The simulation result of SAH reveals that, the highest value of air temperature at the collector outlet is achieved in November, which is around 68°C and the lowest value is achieved in June, which is around 46°C. Comparatively, at the corresponding hours of the day, the values of collector exit air temperature decrease from the highest point in November up to the lowest point in June and then start increasing. For 5 months of the year, the value of temperature is above 60°C for 5 hours, but in October month only for 3 hours and below 50°C for June and July for 24 hours of the day. As, figure 5.3 displays, the value of air temperature inside the collector mainly depends on the value of ambient temperature and solar radiation variation throughout the day and the year (season). The simulation result of the outlet air temperature of SAH is used as an input parameter for the fluent simulation of STD.

4.2.2 Hourly Variation of Useful Energy Output

The simulation of hourly useful solar thermal energy gained by the SAH was done for the time range of [7AM: 5PM]. Also, The constant mass flow rate of air 1.3572 Kg/s and specific heat capacity of air 1.005 Kg/s, inlet hourly ambient temperature, the simulation result of outlet temperature, and estimated hourly solar radiation is used as input parameters. MatLab simulation result of hourly variation of useful heat gain for November 14 is shown in figure 5.4:

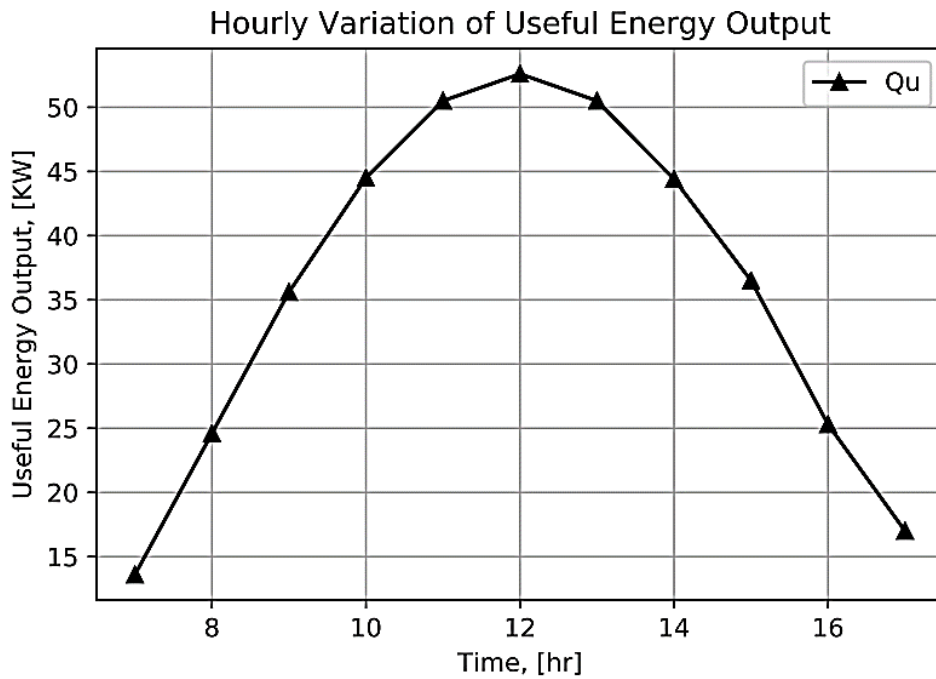


Figure 5.4: Hourly Variation of Useful Energy Gain

Figure 5.4 indicates that, the highest value of useful energy is gained at mid-day around 52.6 KWh and the lowest value is gained at sunrise hour around 13.6 KWh and at sunset hour around 17 KWh. The simulation result reveals that the daily average value of hourly useful energy output is around 35.87 KWh and the daily total value of hourly useful energy output is 403.51 KWh. The result of the simulation indicates, the variation of hourly useful solar thermal energy gain mainly depends on the available solar radiation and ambient temperature, the amount of air mass flow rate, and thermal property of collector material.

4.2.3 Hourly Variation of Thermal Efficiency

The simulation analysis of hourly thermal efficiency variation of SAH was done for the time range [7AM: 5PM] of the day. The input parameters used for the analysis were constant air mass flow rate 1.3572 Kg/s, a constant specific heat capacity of air 1.005 Kg/s, simulation result of hourly useful energy output, estimation result of hourly solar radiation and projection area of the collector 12 m². The result of hourly useful heat gain variation on November 14 is shown in figure 5.5:

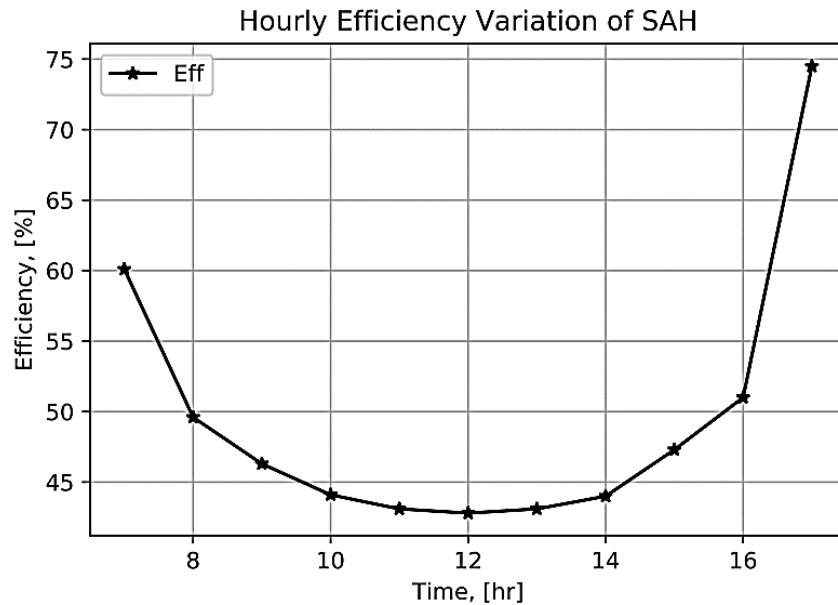


Figure 5.5: Hourly Variation of Thermal Efficiency of SAH

Figure 5.5 indicates that the highest value of thermal efficiency of SAH is encountered at sunset hour around 74.5% and at sunrise hour around 60.1% and the lowest value is encountered at mid-day time around 42.8%. The simulation result reveals that the daily average value of hourly thermal efficiency is around 49.6%. Also, the variation of thermal efficiency throughout the day

mainly depends on the amount of solar radiation, ambient temperature, and air mass flow rate and also, material thermal property and surface area of the collector.

4.3 Result of ANSYS Fluent Simulation of STD

The computational fluid dynamics analysis of the proposed drying system was done using ANSYS Fluent 19.2 (RELEASE). A series of 3D simulations were performed for each model to evaluate the thermal efficiency of the drying system, to study the behavior of the air domain in terms of temperature, velocity, and pressure distribution inside the drying chamber, and to observe the hourly variation of temperature throughout the day. The estimation result of solar radiation (Hourly Diffuse Radiation) and simulation result of SAH (Hourly Outlet Temperature) was used as input parameters. The discussion of ANSYS Fluent result has three main sections, Model 1, Model 2, and Model 3 simulation result.

4.3.1 Simulation Result of Model 1

The simulation analysis of model 1 (*drying chamber without charcoal dust briquette*) was done only for the highest solar radiation in November and the lowest solar radiation in June. This section presents the discussion of hourly average temperature variation, velocity vector, streamline, velocity contour and pressure contour for November, and temperature contour for both November and June.

a) Hourly Temperature Variation

The simulation result of air temperature at the outlet of SAH was used as air input for STD and the estimation result of diffusion radiation was used as input for the analysis of the radiation model. The input parameters used are listed in table 5.1.

Table 5.1: Hot Air Inlet Temperature and Diffuse Radiation on November 14

Inlet Temperature and Diffuse Radiation on November 14												
Time (hr)	AM						PM					
	7	8	9	10	11	12	1	2	3	4	5	6
HAIT (°C)	33.7	42.85	52.3	60.5	66.1	68.2	66.3	60.8	52.6	43.2	34.1	25.6
DR (W/m^2)	120	230	320	390	440	450	441	192	324	231	123	1
<i>HAIT = Hot Air Inlet Temperature and DR = Diffuse Radiation</i>												

The hourly temperature value of the air at the outlet of STD was determined by performing a series of simulations for 12 sunshine hours of the day. Figure 5.6 is a graphical representation of the simulation result of hourly temperature of the air at the outlet of the drying chamber and it demonstrates how the outlet temperature is affected by solar radiation and inlet temperature.

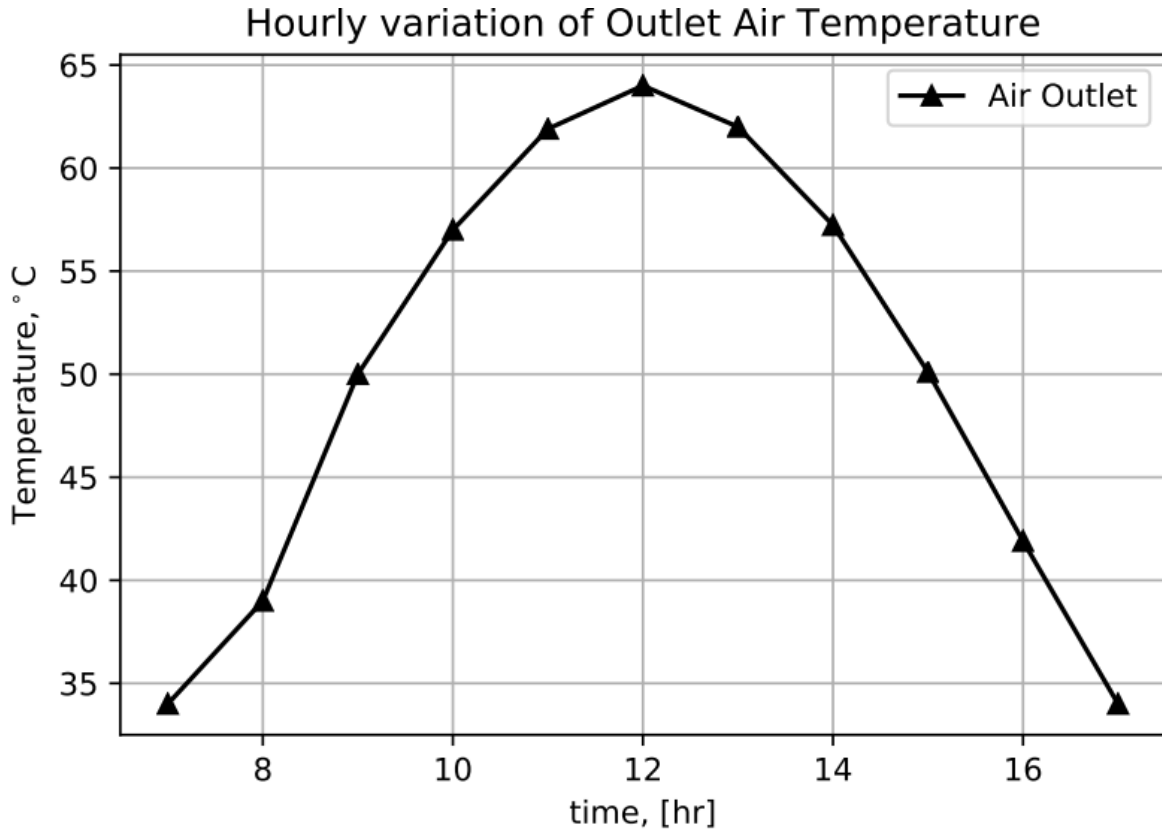


Figure 5.6: Hourly Variation of Outlet Air Temperature

The result indicates that the maximum and the minimum temperature encountered at the outlet is 64°C at 12 PM and 26.82°C at 6 PM respectively. The temperature of the air at the outlet is above 50 for 7 hours of the day. The temperature increases starting from sunrise up to mid-day at 12 PM, which is the maximum point, and decreases up to sunset. This graphical result of the hourly simulation of model 1 clearly shows, the temperature value around the outlet varies due to the changes in solar radiation and inlet temperature.

Figure 5.7, is a pictorial presentation of a simulation result of hourly temperature distribution of air domain at the middle plane inside the STD for different hours, which demonstrates the distribution of temperature at the selected plane is affected by solar radiation due to the location

of the site and the orientation of the drying chamber. The highest value of the result is represented by red while the lowest value is shown by a dark blue and also, green, yellow, orange, and the rest lies in the middle. This figure shows 12 pictures of the simulation result which represents the corresponding 12 sunshine hours of the day starting from 7AM up to 6PM.

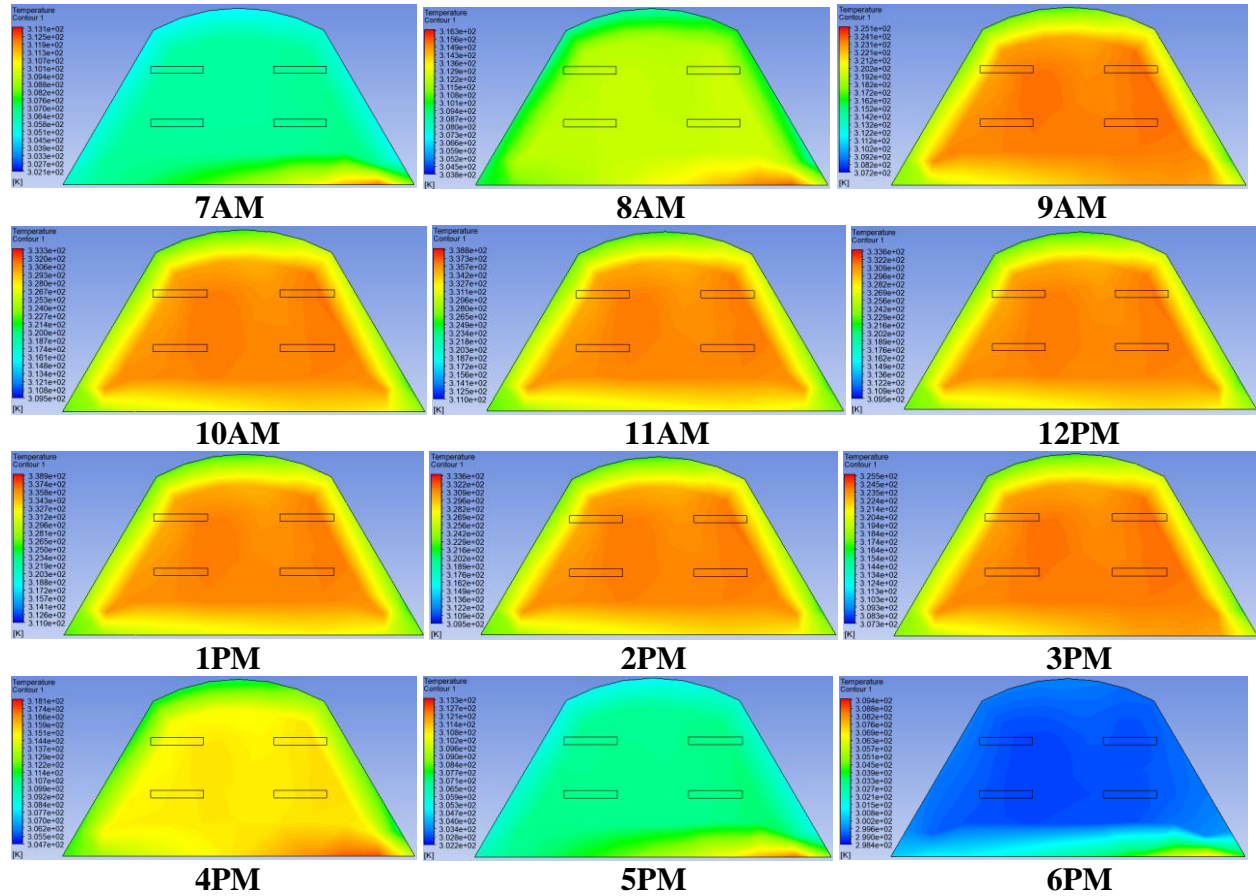


Figure 5.7: Hourly Temperature Variation of Air

The result reveals that there is a uniform temperature distribution on the selected plane for all hours with a different value. In all pictures, the temperature on the right side (southern side) is higher than on the left (northern side). This is due to the East-West orientation of the system and the location of the site which is found on the southern side of the equator. Figure 5.7 clearly shows that the temperature is higher at the center of the plane and gradually decreases toward cover and floor wall boundaries between 9 AM – 3 PM and for the rest of hours the higher temperature is encountered on the floor wall boundary, where gradually decreases up to cover wall boundary.

b) Temperature Distribution

Figure 5.8 shows the temperature distribution of air throughout the chamber on November 14 and June 11. The input parameters used for June is, 46.22°C for inlet air temperature and 170 W/m² for diffuse radiation at 12PM and for November are listed in table 5.1 and a constant inlet mass flow rate of 0.017275 Kg/s was used for every four inlets. Other parameters such as boundary conditions, governing equation, viscous model, and species transport are similar for both months.

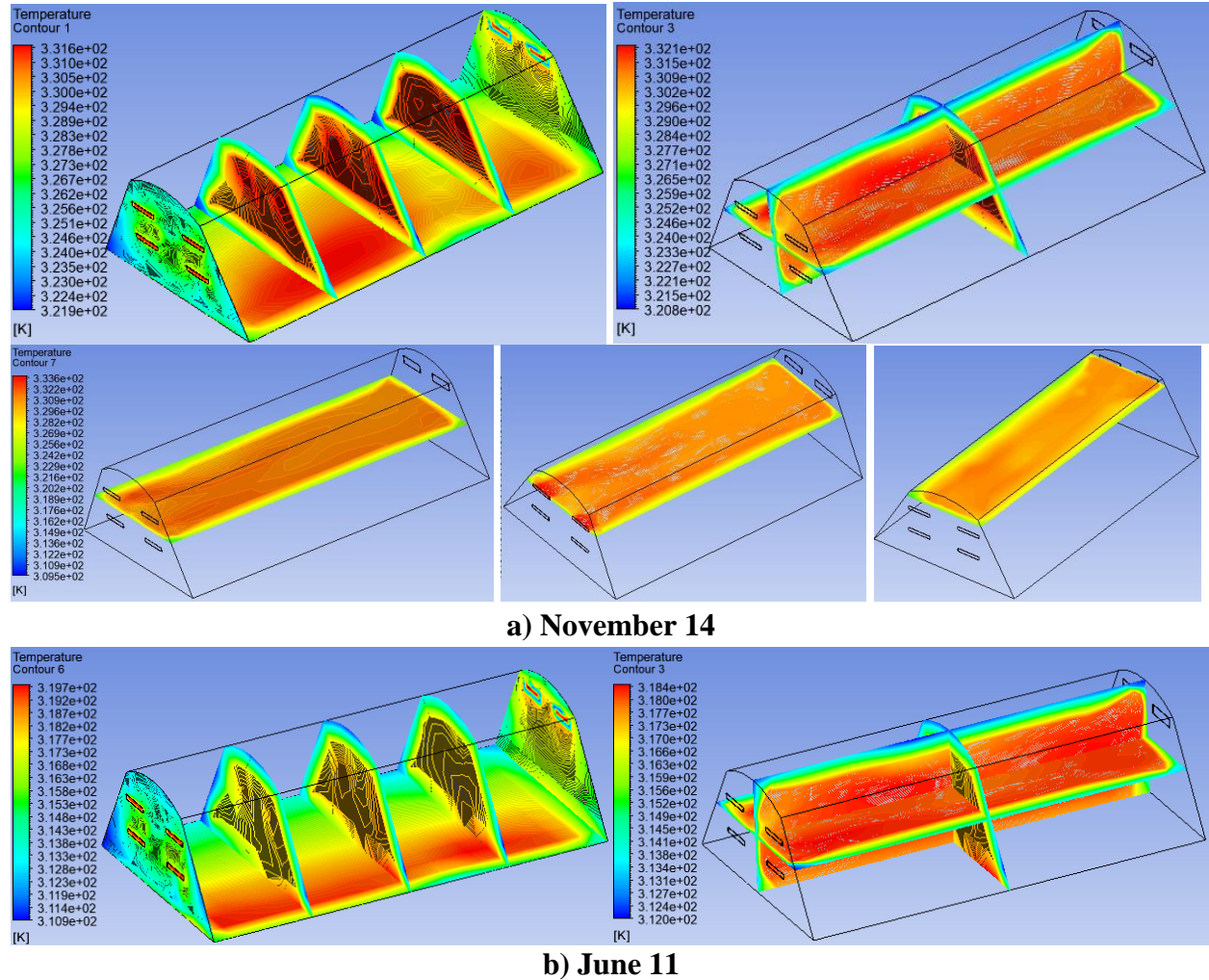


Figure 5.8: Simulation Result of Temperature on a) November 14 and b) June 11

The higher temperature of the air is encountered in November while the lowest in June and the other months lie in between duo to the seasonal variation of solar radiation and inlet temperature. The temperature profile shows, the uniformity of distribution on the floor wall is better for November. The obtained result indicates that for both months the temperature distribution is

almost uniform around face and back walls. This result is similar to the simulation result of Monish. M et.al. (2018) [19] and Yen H. P. et.al. (2021) [54].

Figure 5.9 presents the temperature variation of air on a line drawn between a) North-South, b) East-West, c) Top-Bottom and d) Inlet-Outlet walls. The straight line used to plot graphs a, b and c passes through the center of STD and to plot graph d an inclined line starting from the center of the inlet up to the center of outlet.

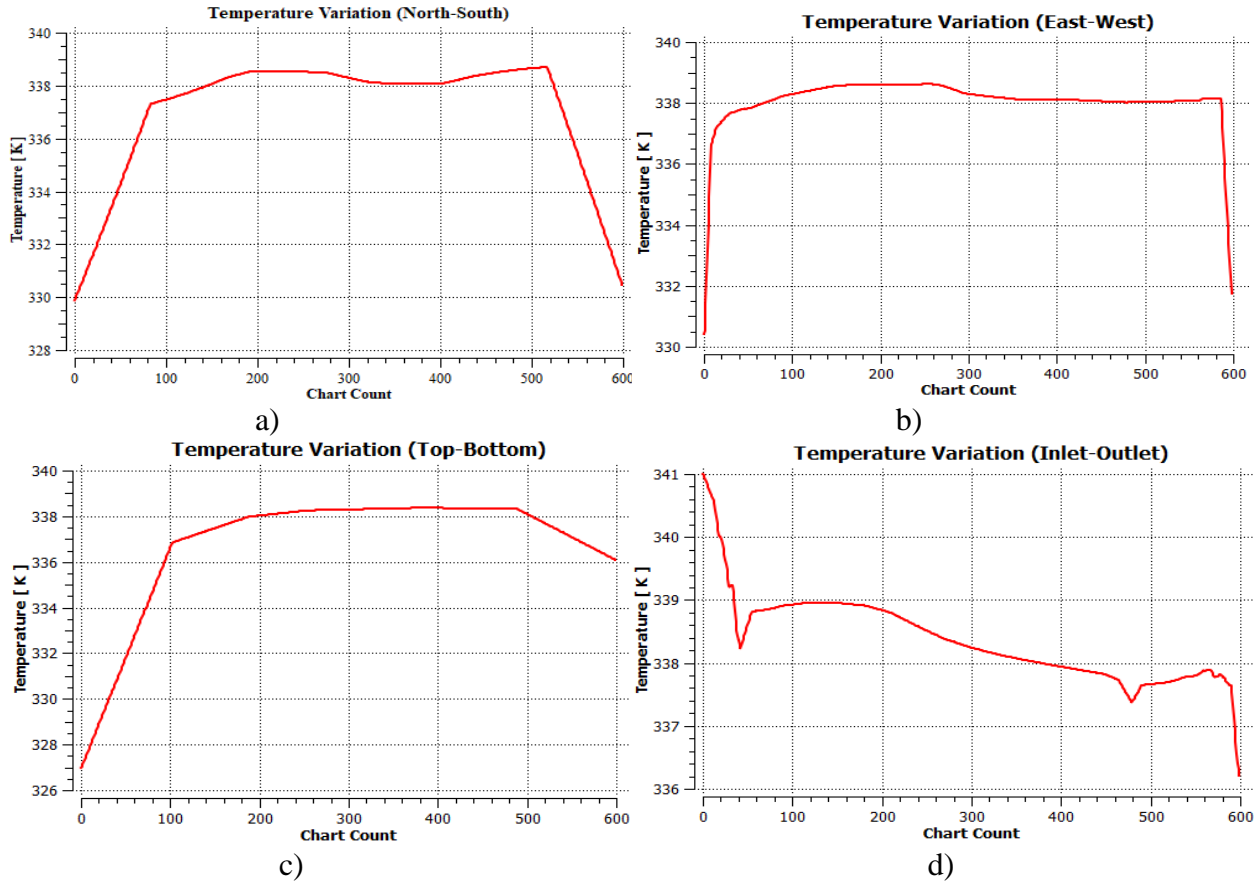


Figure 5.9: Graph of Temperature Variation inside STD on November 14

The result of the simulation reveals that the value of temperature inside the chamber is maximum at the inlet section of the chamber which is around 65°C, the minimum value is around 36.5°C at the outlet section and the average temperature value throughout the drying chamber is 57.71°C. This result of maximum temperature encountered is similar to the simulation result of Yen H. P. et.al. (2021) and the minimum value has a small variation due to the weather condition difference of locations and dimensions of the model [54].

The result of graphs a, b and c indicates that temperature is higher at the center of the drying chamber and lower around the walls. The value of temperature is higher around the south wall and lower around the north wall shown on graph (a), due to the location of the site where the ray of the sun incidence on the horizontal surface is tilted toward the north direction and East-West orientation of the chamber. The result of graph (b) demonstrates, the temperature of the air is higher around the west side of the wall and lower around the east wall, due to the velocity gradient between these two walls, where the velocity is high around the east wall which causes low thermal diffusion and low velocity around the west wall, due to turbulence effect between the walls.

The result of graph (c) illustrates that the temperature of the air is higher around the bottom (floor wall) than the top (cover wall), due to the type of material used for the walls, where the floor wall has higher absorptivity and thermal conductivity while cover wall has lower and also has higher transmissivity. Graph (d) indicates that the temperature of the air is higher at the inlet and gradually decreases toward the outlet which is a minimum point, due to thermal loss with the boundary walls and to surrounding through the cover wall.

c) Velocity and Pressure Profile

For initialization of the fluent simulation, the input parameters temperature and diffusion radiation used are listed in table 5.1 at 12 PM, on November 14, and inlet mass flow rate is 0.017275 Kg/s for each inlet. The result of velocity and pressure variation and distribution is presented in figure 5.10, as well as the velocity streamlines by figure 5.11 and the velocity vector by figure 5.12.

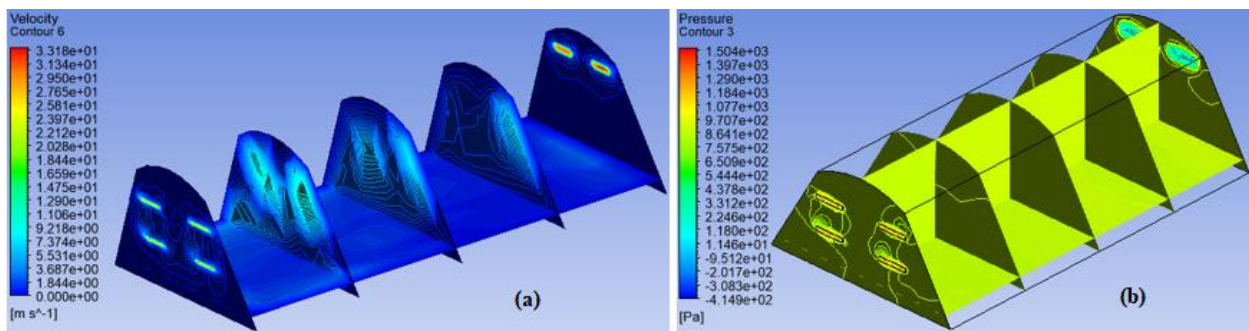


Figure 5.10: Contour Profile of (a) Velocity and (b) Pressure

The result of the simulation reveals that the maximum value of velocity is 33.5 m/s at the outlet section, the minimum value is 0 m/s around the solid wall boundaries and the average value of velocity throughout the drying chamber is 6.93 m/s. Also, the value of pressure is maximum at

the inlet section which is 1521 Pa , the minimum value is -414.85 Pa at the outlet and the average value of pressure throughout the drying chamber of model 1 is 852.41 Pa , this pressure difference between the inlet and outlet section indicates that there is a continuous flow of air inside the chamber.

The result of average velocity and pressure is similar to the simulation result of Monish. M et.al. (2018) [19] and Yen H. P. et.al. (2021) [54], but the result of maximum and minimum value of both parameters are different, because of inlet mass flow rate variation and the different value of dimension, shape, size, number and position of air inlet section and air outlet section of the drying chamber in each of the models. Figure 5.11 presents 3D, top, right side and front view descriptions of velocity streamline throughout the drying chamber.

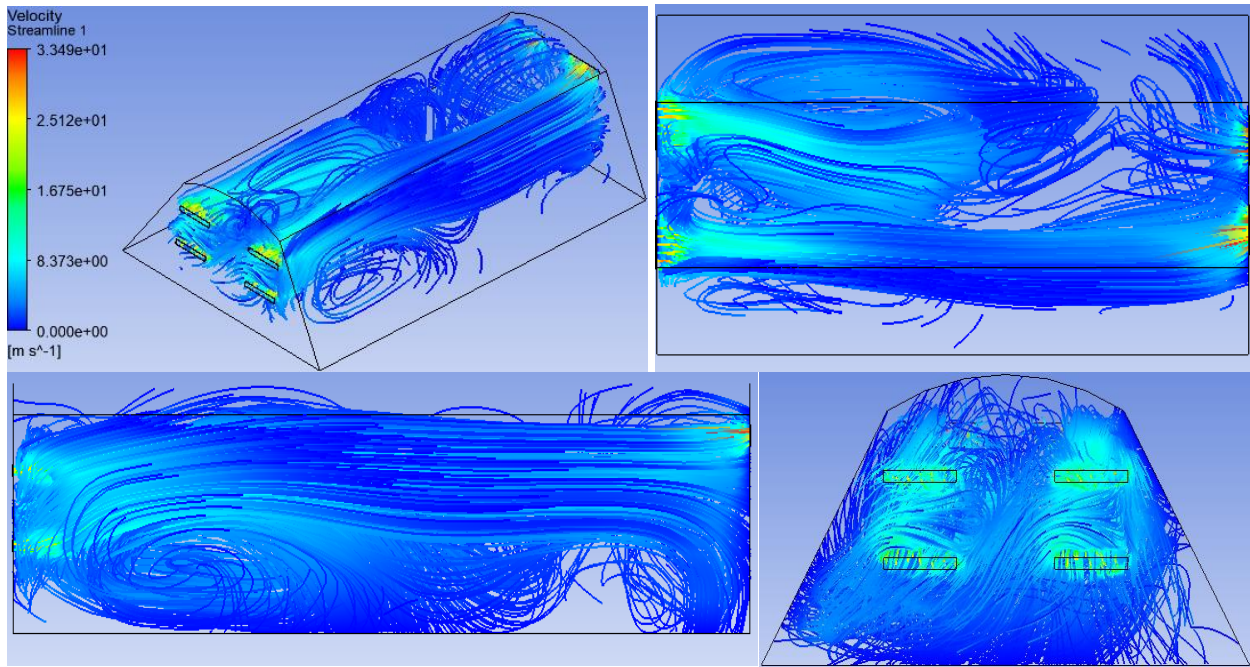


Figure 5.11: Velocity Streamline of Model 1

Figure 5.12 presents 3D, top and front view descriptions of velocity vector throughout the drying chamber.

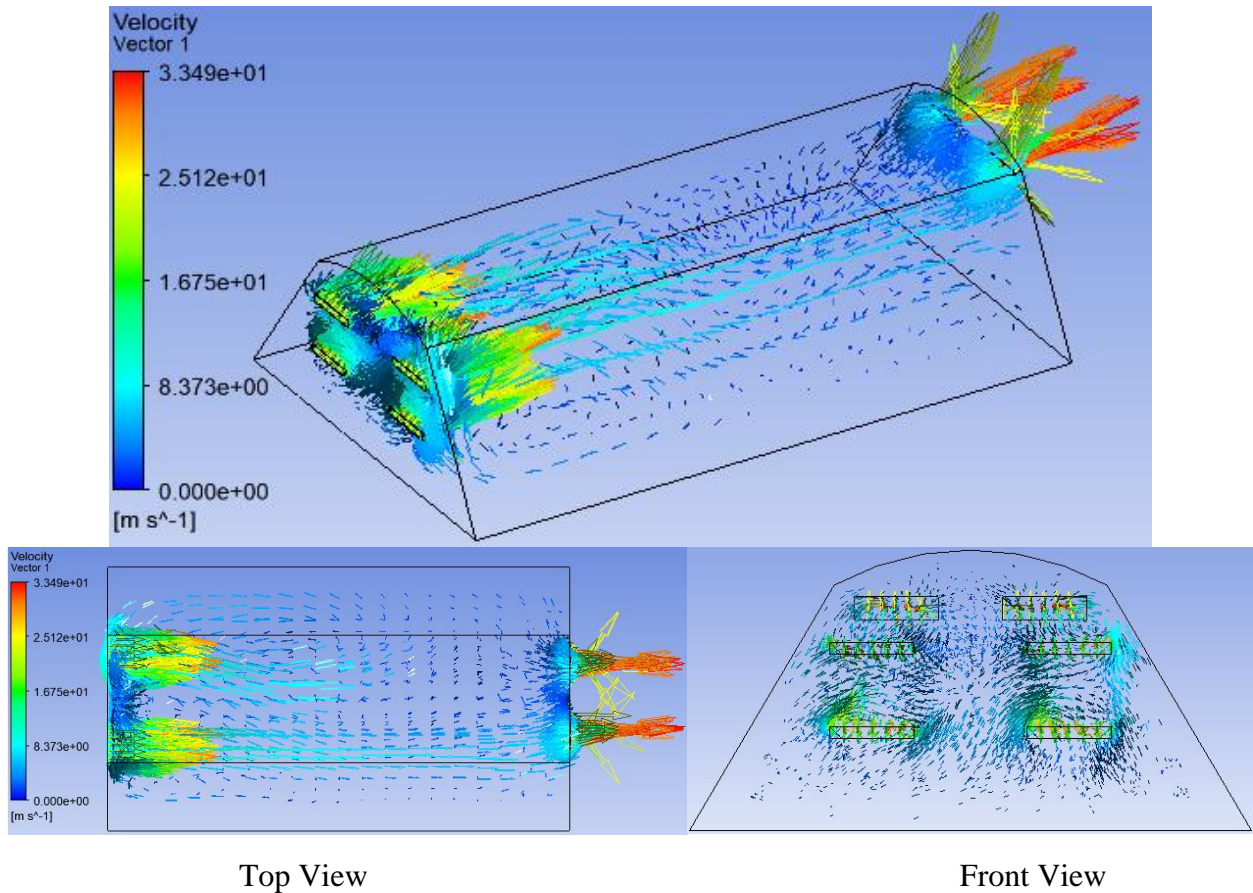


Figure 5.12: Velocity Vector of Model 1

The result of velocity streamlines functions in figure 5.11 and velocity vector in figure 5.12, reveals that the higher turbulence observed around the inlet and outlet section of the chamber, due to the higher velocity encountered and the cross-sectional area difference and also, the value of turbulence is lower in the other cross-section, due to velocity drop and pressure drop around the boundary surface of the solid domain (cover and floor inner wall). Pressure drop occurs due to the high viscosity of air domain on the surface of solid boundaries.

d) Hourly Variation of Useful Energy Output

Figure 5.13 presents the simulation result of hourly useful solar thermal energy gained by the STD for the time range of [7AM: 5PM]. The constant mass flow rate of air 1.3572 Kg/s, the simulation result of air temperature at the outlet of SAH, and estimated hourly solar radiation was used as input parameters. ANSYS Fluent simulation result of hourly variation of useful heat gain for November 14 is shown in figure 5.13:

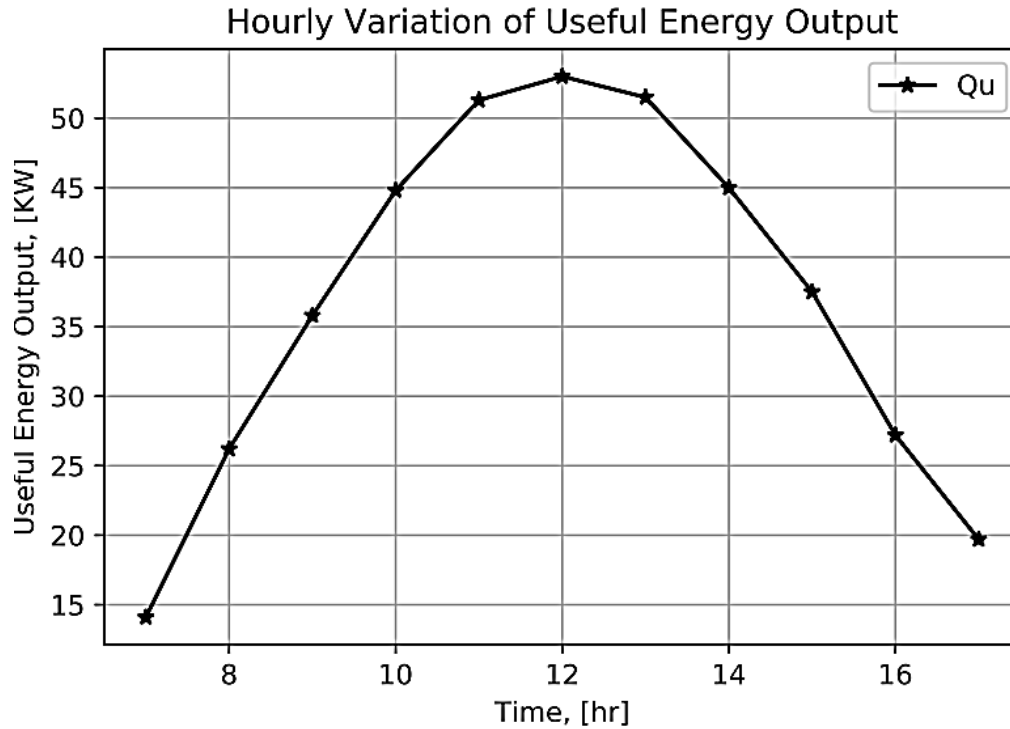


Figure 5.13: Hourly Variation of Useful Energy Gain of STD

Figure 5.13 indicates that the highest value of useful energy is gained at mid-day around 53 *KWh* and the lowest value is gained at sunrise hour is about 14.1 *KWh* and at sunset hour around 19.7 *KWh*. This clearly indicates, the variation of hourly useful solar thermal energy gain mainly depends on the available solar radiation and ambient temperature, the amount of air mass flow rate and thermal property of collector material. The simulation result reveals that the daily average value of hourly useful energy output of STD is around 36.86 *KWh* and the daily total value of useful energy output is 418.1 *KWh*. Comparatively, this total useful energy gained from the simulation result is higher than the required useful energy received from drying air, which is 362.12 *KWh* which suggests that the charcoal briquettes are expected to dry within a day.

e) Hourly Variation of Thermal Efficiency

The simulation analysis of hourly thermal efficiency variation of STD was done for the time range [7AM: 5PM] of the day. The input parameters used for the analysis were constant air mass flow rate 1.3572 *Kg/s*, the simulation result of hourly useful energy output, estimation result of hourly solar radiation, and projected area of the collector 0.07 *m*². The result of hourly useful heat gain variation on November 14 is shown in figure 5.14.

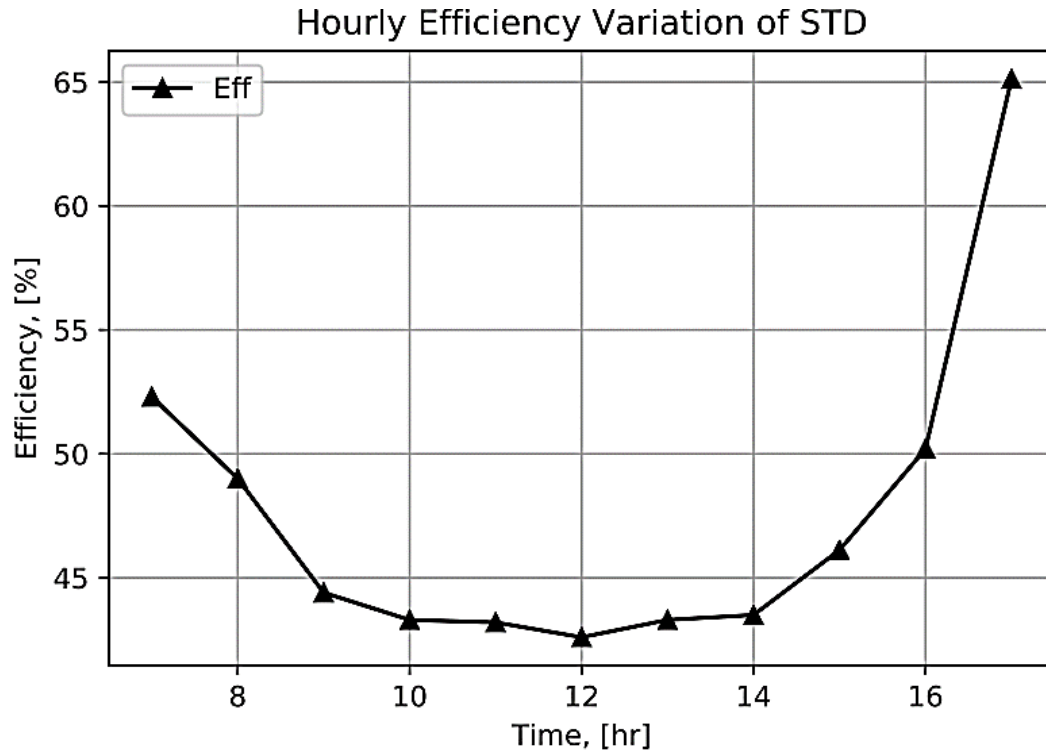


Figure 5.14: Hourly Variation of Thermal Efficiency of STD

Figure 5.14 indicates that the highest value of thermal efficiency of STD is encountered at sunset hour around 65.12% and at sunrise hour around 52.25% and the lowest value is encountered at mid-day time around 42.6%. The simulation result reveals that the daily average value of hourly thermal efficiency is around 47.54%. Also, the variation of thermal efficiency throughout the day mainly depends on the amount of solar radiation, ambient temperature, and air mass flow rate and also, material thermal property and surface area of the collector.

4.3.2 Simulation Result of Model 2

The simulation of model 2 was done for the drying chamber with charcoal dust briquette for the highest solar radiation month of the year, on the representative day, which is November 14 at 12PM. The input parameters hot air inlet temperature and diffusion radiation at noon, used for the fluent simulation are similar to model 1, which is listed in table 5.1, and the constant value of inlet mass flow rate for each inlet of the chamber. The result discussion of model 2 includes temperature contour, temperature graph, pressure contour, velocity contour, velocity streamline, and velocity vector analysis.

a) Temperature Profile

For initialization of the fluent simulation, the input parameters temperature of the hot air inlet is 68°C, diffusion radiation is 450 W/m² at 12 PM, on November 14 and the constant value of hot air inlet mass flow rate is 0.017275 Kg/s for each of four inlet sections of the chamber. The result of temperature variation and distribution of charcoal dust briquette and drying chamber was presented in figure 5.15, as well as temperature graph of briquette on all beds at different sections was illustrated in figure 5.16.

Where; figure 5.15, (a) demonstrates the temperature profile of briquette, (b) at the center of the chamber on z – x plane, (c) at the center of the chamber on x – y plane and (d) at the center of the chamber on z – y plane.

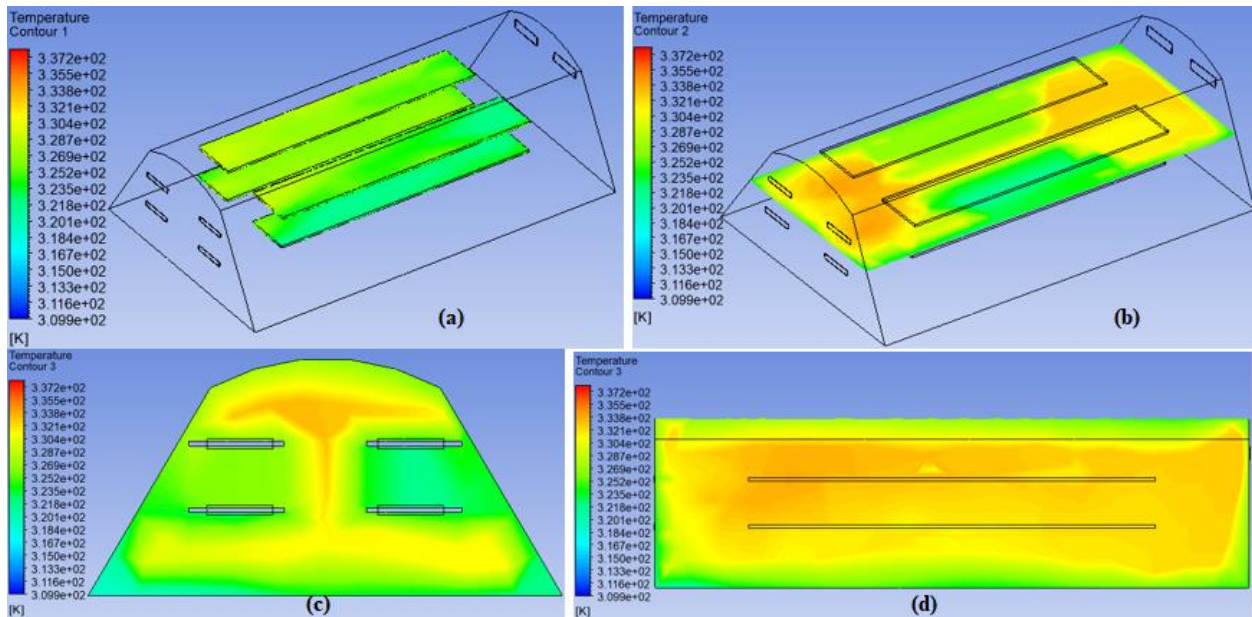


Figure 5.15: Temperature Profile of (a) Briquette Wall and (b, c and d) Drying Chamber

Figure 5.16 presents the temperature variation on the surface of the briquette wall; on the upper bed and lower bed of both left and right side drying bed. All graph has three different lines which present a different cross-section of briquette, the red solid line is at the left edge side, the blue dash line is at the center and the green dot line is at the right edge side on the outer surface of drying product.

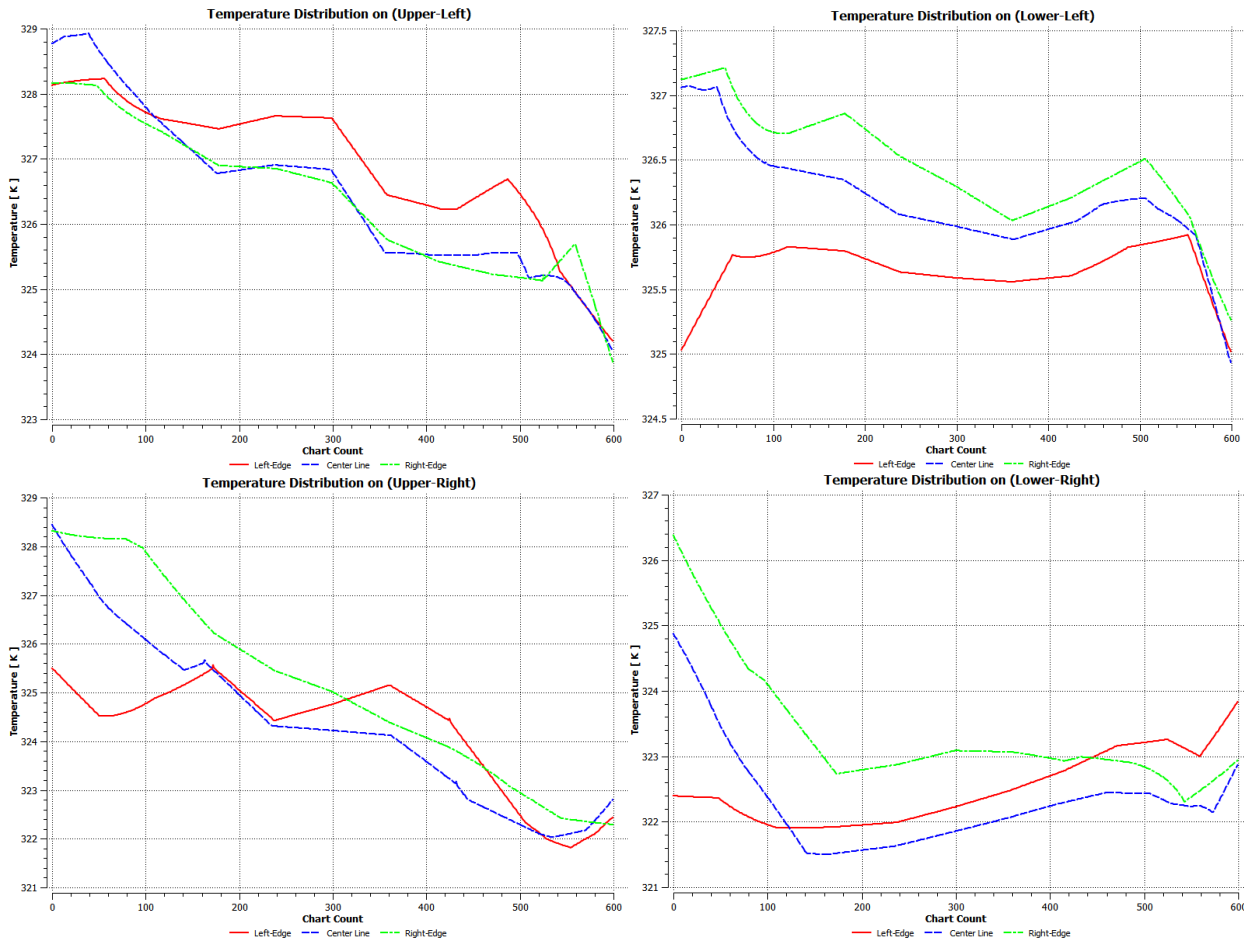


Figure 5.16: Temperature distribution on the Surface of Briquette Wall

The result of the simulation reveals that the maximum value of the briquette temperature is 57°C on the upper bed of the left side drying bed, the minimum value is 49°C on the lower bed of the right side drying bed and the average value of temperature on the surface of briquette is 52°C. Furthermore, the value of temperature inside the chamber is maximum at the inlet section which is 65°C, the minimum value is 36°C at the outlet and the average value throughout the drying chamber of model 2 is 58.5°C. Figure 5.15 displays almost a uniform temperature distribution on the surface of the briquette under both drying beds, where the higher distribution is around the left side (north) and the lower distribution is around the right side (south). Also, inside the chamber, there is a uniform temperature distribution between the drying beds at the center in figure 5.15 (d), below every four beds, and above the upper beds in figure 5.15 (c).

The temperature variation on the surface of the briquette wall and inside the drying chamber is illustrated in figure 5.15 and on graph 5.16, where a higher value is found around the inlet due to

higher hot air inlet temperature and left (north) side of the chamber due to the location of the site (north-facing), while the lower value is around the outlet due to temperature interaction of air domain and solid domain inside the chamber and right (south) side of the chamber due to the shading of the left side drying bed, because of north-facing.

a) Velocity and Pressure Profile

For initialization of the fluent simulation, the input parameters temperature of the hot air inlet is 68°C, diffusion radiation is 450 W/m² at 12 PM, on November 14 and the constant hot air inlet mass flow rate in every of four inlet sections of the drying chamber is 0.017275 Kg/s. The result of velocity and pressure variation and distribution profile inside the chamber and on the outer surface of the briquette wall is presented in figure 5.17, as well as the velocity streamlines and velocity vector by figure 5.18.

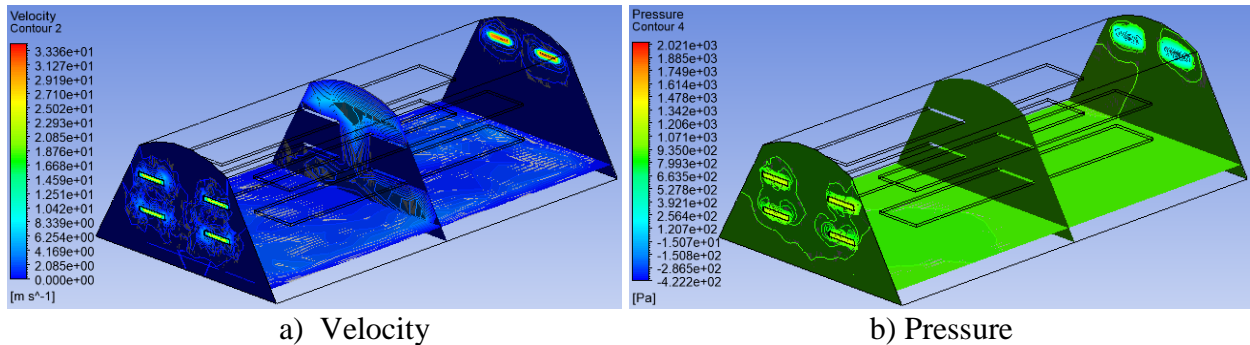


Figure 5.17: Contour Profile of (a) Velocity and (b) Pressure

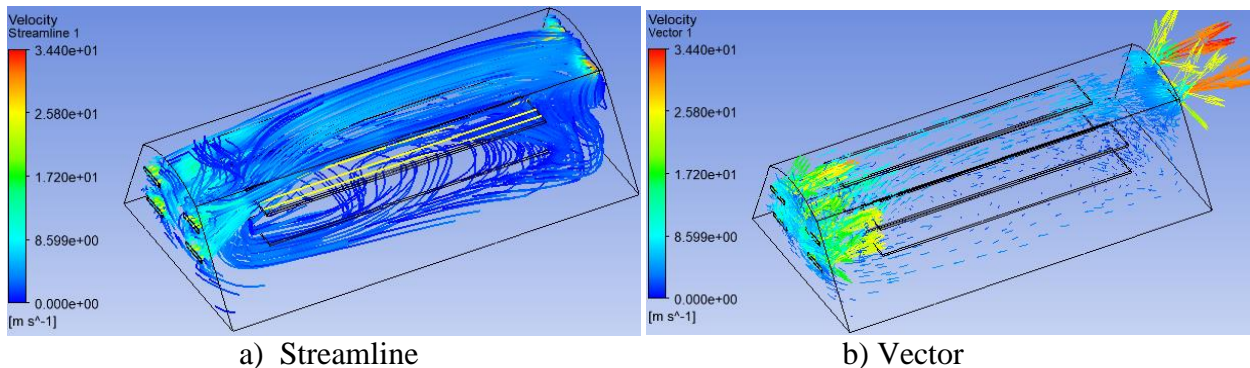


Figure 5.18: Velocity Streamline and Vector of Model 2

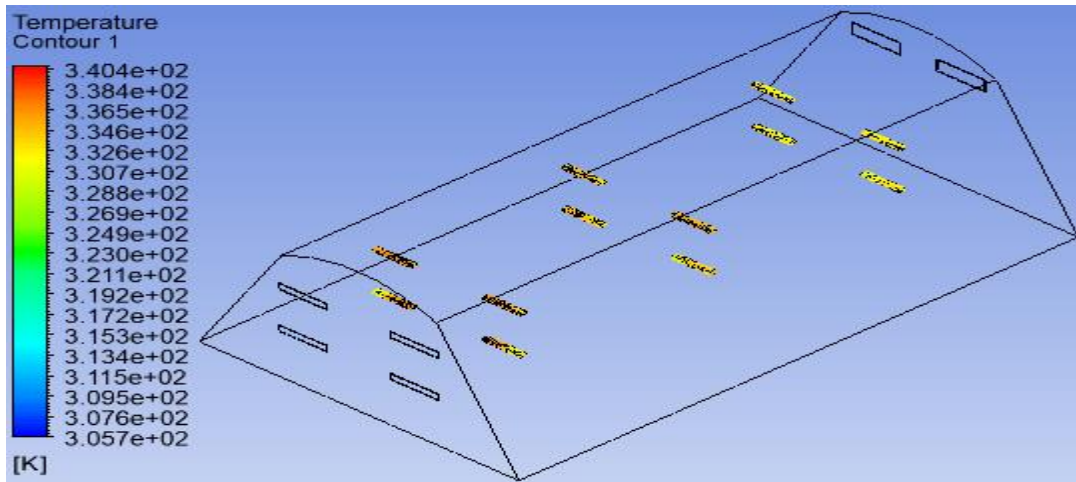
The result of the simulation reveals that the maximum value of velocity is 34.4 m/s at the outlet section, the minimum value is 0 m/s around the briquette, cover and floor wall boundaries and the average value of velocity throughout the drying chamber is 6.02 m/s. Also, the value of

pressure is maximum at the inlet section which is $2043.4 Pa$, the minimum value is $-422.24 Pa$ at the outlet and the average value of pressure throughout the drying chamber of model 2 is $886 Pa$, this pressure difference between the inlet and outlet indicates that there is a continuous flow of air inside the chamber.

The result of velocity streamlines function and velocity vector in figure 5.17, shows that the higher turbulence is observed around the inlet and outlet section of the chamber and also at the front and back surface of briquette walls, due to the higher velocity encountered and the cross-sectional area difference and also, the value of turbulence is lower in the other cross-section of the chamber and briquette walls, especially on the upper bed the flow of air is very smooth. Compared to model 1, the value of the velocity at the air outlet and the value of pressure is higher in model 2, but the average velocity is higher in model 1, due to the flow stream disturbance of briquette geometry addition inside the chamber.

4.3.3 Simulation Result of Model 3

The simulation of model 3 was done for the drying chamber and 120 samples of charcoal dust briquette with real shape from Verde Africa Company and with real arrangement inside the chamber for the month with the highest solar radiation of the year, on the representative day, which is November 14 at 12 PM. The fluent simulation result discussion of model 3 presents the figure of temperature contour of charcoal dust briquette, to describe the profile of temperature variation and distribution on the outer surface and inner surface (inside cylindrical hole) of briquette. The values of input parameters are the temperature of the hot air inlet which is $68^{\circ}C$, diffusion radiation is $450 W/m^2$ and a constant inlet mass flow rate is $0.017275 Kg/s$ for each inlet.



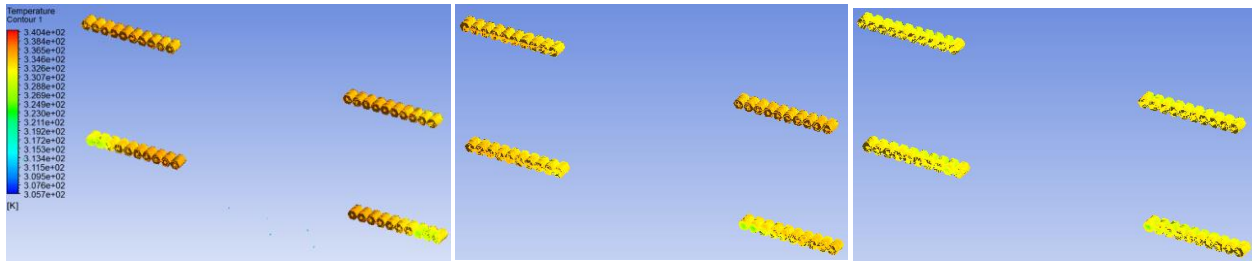


Figure 5.19: Temperature Contour of a) Model 3 and b) Front, c) Middle and d) Back Rows

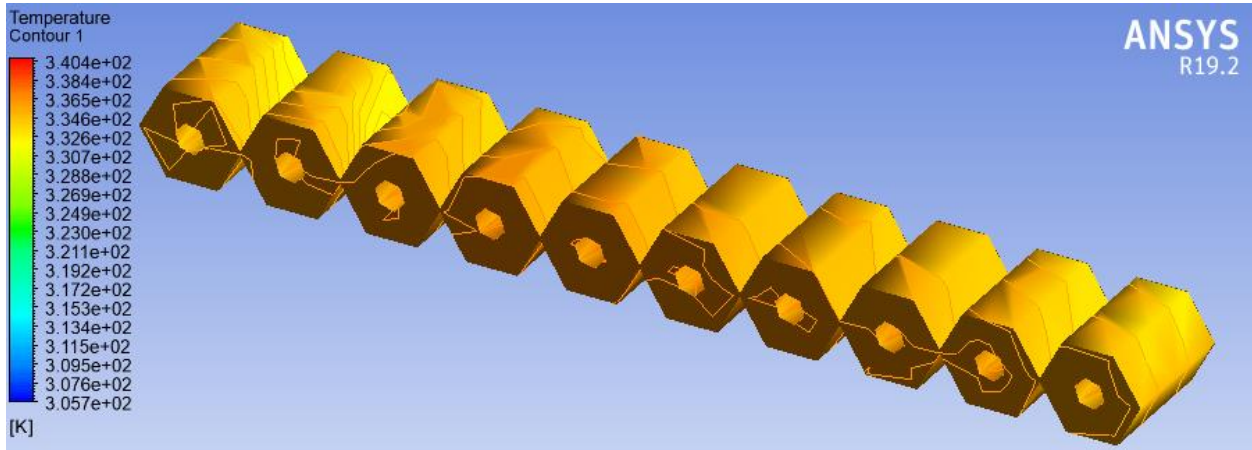


Figure 5.20: Temperature Contour on Upper Front Row of Briquette

The result of the simulation reveals that the maximum value of the temperature of briquette is 64.2°C on the upper front row of the left side drying bed, the minimum value is around 43.3°C on the lower back row of the right side drying bed and the average value of temperature on the surface of briquette is 60.1°C. Also, the value of temperature inside the chamber is maximum at the inlet section which is 65°C, the minimum value is 32.7°C at the outlet and the average value throughout the drying chamber of model 3 is 64.2°C.

Figure 5.20 displays that there is a uniform temperature distribution on the outer surface and inside the cylindrical hole surface of the briquette on each row. Similarly, the variation of temperature is illustrated in figure 5.19, where the higher temperature is observed at the upper front row of the left side (north), due to higher hot air inlet temperature and the location of the site (north-facing), while the lower value is at the lower back row of the right side (south), due to temperature interaction between air domain and solid domain (briquette, cover and floor surface) inside the chamber and north-facing orientation of the chamber because of the location of the site.

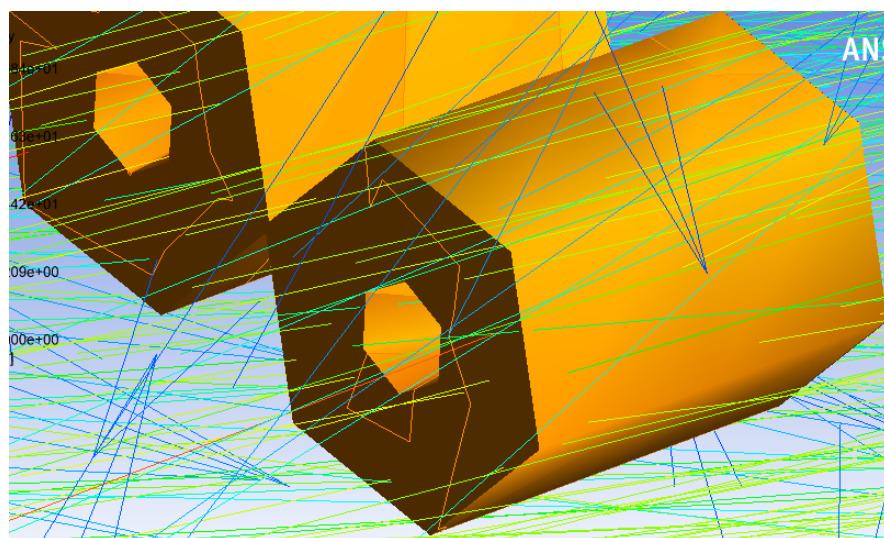
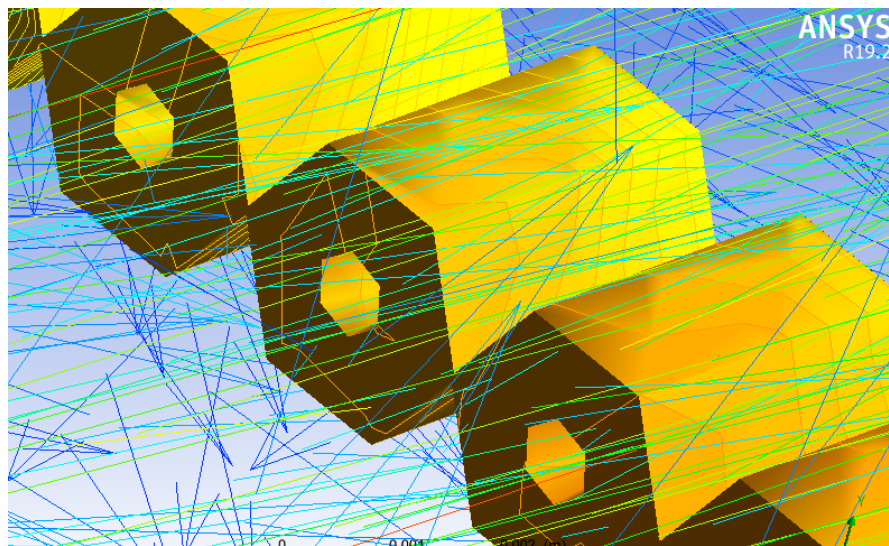
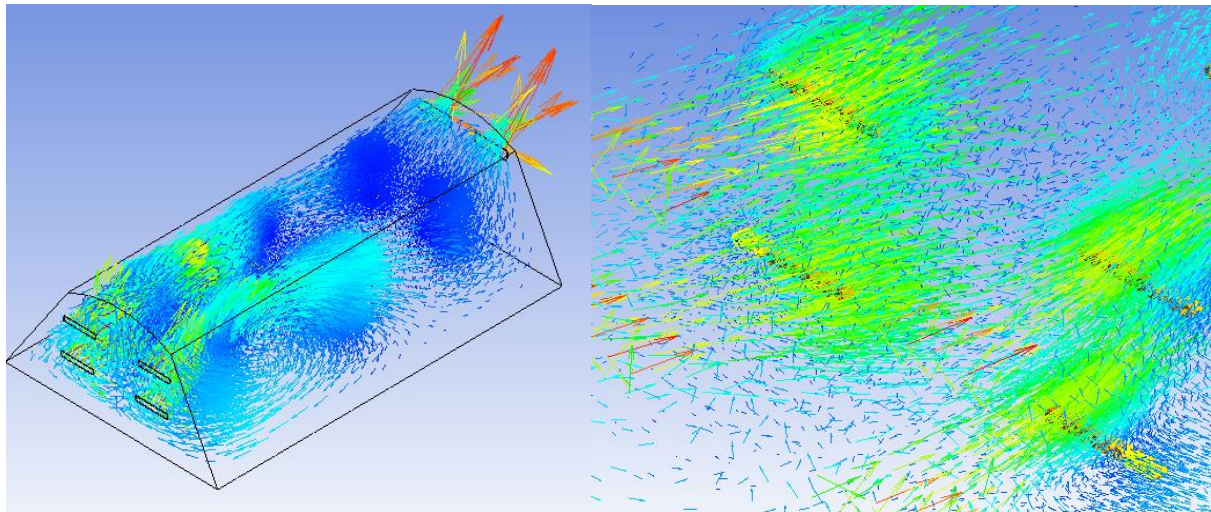


Figure 5.21: Velocity Vector of Model 3

CHAPTER 6

CONCLUSION AND RECOMMENDATION

6.1 Conclusion

A solar tunnel drying system with forced convection was designed and optimized to dry a charcoal dust briquette product of Verde Africa Lda in Mozambique, Maputo province. The proposed system consists of two main units namely solar tunnel greenhouse and solar air heater. The overall size of the drying chamber is $17.5\text{ m} \times 4\text{ m} \times 2\text{ m}$, length, width, and height respectively and the overall surface area of the collector is 10m^2 .

The simulation result of SAH reveals that the highest value of air temperature is achieved in November, around 68°C and the lowest value is achieved in June, around 46°C . For 5 months of the year, the value of temperature is above 60°C for 5 hours, but in October only for 3 hours and below 50°C for June and July for 24 hours of the day. This, outlet air temperature was used as the input temperature for the solar tunnel dryer simulation.

The CFD simulation of the STD without briquette shows, the maximum temperature inside the chamber of 65°C and the minimum value of 36.5°C with an average of 57.71°C . The temperature of the air inside the chamber is above 50°C for 7 hours of the day. For a constant mass flow rate of 1.3572 Kg/s , it was observed a maximum velocity of 33.5 m/s and an average of 6.93 m/s . The daily average thermal efficiency of the drying system is 47.54% .

Uniform temperature distribution was found on the surface of the briquette and almost throughout the chamber, except at the inlet and outlet section. The daily average temperature of the briquette wall and drying air temperature is similar to the initial design temperature for all months except June and July. This clearly indicates that one batch of the charcoal dust briquette can be dried within one day for ten months of the year and only for June and July additional drying period will be required. In general, the value of daily total useful energy received from the drying air is greater than the amount of thermal energy required for the drying process. From this result, it can be concluded that the proposed drying system will reduce the drying period of briquette from 7 to 1 day comparing with open sun drying consequently making briquette alternative renewable energy for conventional charcoal.

6.2 Recommendation

The following points can be recommended for future work, to maximize the overall efficiency of the solar tunnel dryer.

- Experimental investigations are needed to confirm the performance and efficiency of the proposed model, by validating the simulation result.
- The simulation of STD can be done for both heat transfer and mass transfer analysis to study moisture removal rate, drying time, and water vapor distribution throughout the chamber.
- It is also suggested to evaluate the performance of STD under different geographical locations and for a different type, shape, weight, and size of biomass fuel briquette.
- To improve the STD through the integration of a backup heating source of energy to fulfill the season and days with low incidence solar radiation.
- Economical benefits of the system for the briquette factories as well as for the end-users have to be evaluated.

REFERENCE

- [1] WHO (World Health Organization) (2018). Household air pollution and health, www.who.int/news-room/fact-sheets/detail/household-air-pollution-and-health (accessed 07 December 2020);
- [2] Njenga M., Gitau, J., Liyama M., Jamnadassa R., Mahmoud Y., and Karanja N., C. (2019) Innovative biomass cooking approaches for sub-Saharan Africa. *J Clean Prod*, 121, 208 -217.
- [3] International Energy Agency (IEA). (2006) *World Energy Outlook*. IEA/OECD, Paris, France;
- [4] Njenga M., Karanja N., Karlsson H., Jamnadass R., Iiyama M., Kithinji J. and Sundberg C. (2014) Additional cooking fuel supply and reduced global warming potential from recycling charcoal dust into charcoal briquette in Kenya. *J Clean Prod*, 81, 81-88
- [5] World Health Organization (WHO). (2006) *Global WHO Air Quality Guidelines, for Particulate Matter, Ozone, Nitrogen, Dioxide and Sulfur Dioxide*. Global Update 2005;
- [6] Mwampamba H., Owen M., Pigah M., (2013) Opportunities, challenges and way forward for the charcoal briquette industry in Sub-Saharan Africa. *Energy for Sustainable Development* 17 (2013) 158–170;
- [7] Cuilas C.A., Jirjis R., Lucas C., Energy situation in Mozambique: A review, (2010) *Renewable and Sustainable Energy Reviews* 14. 2139–2146;
- [8] Luz A. C., Fisher J., Baumert C., Grundy I., (2015) Charcoal production and trade in southern Mozambique: historical trends present scenarios. XIV World Forestry Congress, Durban, South Africa;
- [9] Madyira D. M. and Gibson J., (2010). Biomass briquette drying process using solar energy, *Journal of the Technical Association of the Pulp and Paper Industry of South Africa*, vol. 4;
- [10] Bhattacharya S.C., (2009) Biomass energy and densification: A global review with emphasis on developing countries;
- [11] Da Silva I.P., Dold F., Kakooza M., Bgumisa E, Wassleer S., Kossakowski P., Abbo M., Lsoto D., (2014) Increased production of charcoal briquettes through solar drying. Center for Research in Energy & Energy Conservation, Mekerere University, Uganda;
- [12] Arisaka, J., (2019). Recycled charcoal briquettes in Mozambique - Affordable and quality energy for all. Verde Africa, Lda, Mozambique;
- [13] Monish. M, Ramnath. S, Manojkumar. S, Jeeva S., (2018) solar tunnel air dryer: a computational fluid dynamics investigation for the flow path design with the temperature distribution. *International Journal of Mechanical and Production*, Vol. 8, Special Issue 7, 263-273;
- [14] Saravanapriya, G., Mahendiran, R., Kamaraj, S and Karthik, C., (2016) Copra drying in the solar and biomass integrated dryer. *International Journal of Agricultural Science*, vol. 8, pp.3218-3221;
- [15] S.C. Prashant, K. Anil, and G. Bhupendra, (2017). A review of thermal models for greenhouse dryer, *Renewable and Sustainable Energy Reviews*, vol.75, pp. 548-558;
- [16] Ayyapan, S., Mailsam, K., (2010), Experimental investigation of solar tunnel dryer for copra drying. *Journal of scientific and industrial research*, vol.69;

- [17] Tawonusab, charoenporn, Lertsatitthanakorn, NattapolPoom, LamulWiset ,LifengYang, Siriamornpun S., (2008), Experimental performance of a solar tunnel dryer for drying silkworm pupae, biosystem engineering IOI,209-216;
- [18] Kagande, L., Musoni S. & Madzore J. (2012) Design and performance evaluation of solar tunnel dryer for tomato fruit drying in Zimbabwe. IOSR Journal of Engineering. Vol. 2, Issue 12
- [19] Minag. Ministry of Agriculture. (2007).Mozambique, Maputo.
- [20] Matthew G. Green Dishna Schwarz (GTZ-GATE), Solar Drying Technology for Food Preservation, August 2001, Eschborn, Germany
- [21] Amin, A. Z. (2013). Mozambique Renewable Readiness Assessment 2012. Ed. by IRENA;
- [22] Hammar, L. (2011). Distribution of Wind and Solar Energy Resources in Tanzania and Mozambique, p.8. [url:http://publications.lib.chalmers.se/records/fulltext/local_150046.pdf](http://publications.lib.chalmers.se/records/fulltext/local_150046.pdf);
- [23] Alfayo R., Uiso C.B.S. (2002) Global Solar Radiation Distribution and Available Solar Energy Potential in Tanzania. Physica Scripta. 97: 91 -98
- [24] Madyira D. M. and Gibson J., (2010). Biomass briquette drying process using solar energy, Journal of the Technical Association of the Pulp and Paper Industry of South Africa, vol. 4;
- [25] Udomkun P., Romuli S., Schock S., Mahayothee B., Sartas M., Wossen T., Njukwe E., Vanlauwe B., Müller J., (2020). Review of solar dryers for agricultural products in Asia and Africa: An innovation landscape approach. Journal of Environmental Management. <http://www.elsevier.com/locate/jenvman>;
- [26] Arisaka, J., (2019). Recycled charcoal briquettes in Mozambique - Affordable and quality energy for all. Verde Africa, Lda, Mozambique;
- [27] Njenga M., Karanja N., Karlsson H., Jamnadass R., Iiyama M., Kithinji J. and Sundberg C. (2014) Additional cooking fuel supply and reduced global warming potential from recycling charcoal dust into charcoal briquette in Kenya. J Clean Prod, 81, 81-88
- [28] Arata, A., Sharma, V.K., Spagna, G., Performance evaluation of solar assisted dryers for low temperature drying application-II Experimental results. Energy Convers Manage. 34(5): 417–426. doi: 10.1016/0196- 8904(93)90091-N. (1993).
- [29] Megha S. Sontakke¹, Prof. Sanjay P. Salve. (2015) “Solar. Drying Technology”, International Refereed. Journal Of Engineering And Science (IRJES). Volume 4, Issue 4.
- [30] C.L. Hii, S.V. Jangam, S.P. Ong and A.S. Mujumdar, Solar drying: Fundamentals, applications and innovations. (ISBN: 978-981-07-3336-0, 2012)
- [31] Cuilas C.A., Jirjis R., Lucas C., Energy situation in Mozambique: A review, (2010) Renewable and Sustainable Energy Reviews 14. 2139–2146;
- [32] Patil, R., Gawande, R.. (2016) A review on solar tunnel greenhouse drying system. Renewable and Sustainable Energy Reviews 56, 196– 214. Nagpur, India
- [33] Bux, M., Muhlbauer, W., Bauer, K., Kohler, B. (2002). Solar crop drying in developing countries, Berne.

- [34] R. J. Fuller, 'SOLAR DRYING - A TECHNOLOGY FOR SUSTAINABLE AGRICULTURE AND FOOD PRODUCTION', in *Solar Energy Conversion and Photoenergy Systems*, vol. III, Encyclopedia of Life Support Systems (EOLSS), 2002, p. 12.
- [35] Weiss, J. and Buchinger, J. *Solar Drying*. Training Course within the Scope of the Project Establishment of a Production, Sales and Consulting Infrastructure for Solar Thermal Plants in Zimbabwe. Australian Development Cooperation, Institute of Sustainable Technologies, Australia, 2012.
- [36] Johannes P. Angula and Freddie Inambao, Computational Fluid Dynamics in Solar Drying. *International Journal of Mechanical Engineering and Technology* 10(11), 2019, pp. 259-274.
- [37] Jasim Ahmed and Mohammad Shafi ur Rahman. (2012). *Hot Air Drying Design: Tray and Tunnel Dryer*. Handbook of Food Process Design, First Edition. Blackwell Publishing Ltd.
- [38] Kiranoudis, C.T., Marouliqa, Z.B., Marinou-Kouris, D. and Tsampanlis, M. (1997) Design of tray dryers for food dehydration. *Journal of Food Engineering* 32: 269–291.
- [39] M. A. Leon, S. Kumar, and S. C. Bhattacharya, 'A comprehensive procedure for performance evaluation of solar food dryers', *Renew. Sustain. Energy Rev.*, vol. 6, no. 2002, pp. 367–393, 2001.
- [40] Johannes P. Angula and Freddie Inambao, Computational Fluid Dynamics in Solar Drying. *International Journal of Mechanical Engineering and Technology* 10(11), 2019, pp. 259-274.
- [41] Kumar, M., Sansaniwal, S. K. and Khatak, P. Progress in Solar Dryers for Drying Various Commodities. *Renewable and Sustainable Energy Reviews*, 55, 2016, pp. 346-360.
- [42] Ambesange, A. I. and Kusekar, S. K. Analysis of Flow Through Solar Dryer DUCT using CFD. *International Journal of Engineering Development and Research*, 5(1), 2017.
- [43] Rosli, I. M., Nasir, A. M. A., Takriff, S. M. and Chem, L. P. Simulation of a Fluidized Bed Dryer for the Drying of Sago Waste. *Energies*, 11(9), 2018, pp. 2383. DOI:10.3390/en11092383.
- [44] Jamaledine, T. and Ray, B. M. Application of Computational Fluid Dynamics for Simulation of Drying Processes: A Review. *Drying Technology*, 28, 2010, pp. 120-154.
- [45] Kumar A, Tiwari GN, Kumar S, Pandey M. (2006). Role of greenhouse technology in agricultural engineering. *Int J Agric Res*;1(4):364–72.
- [46] Janjai S. (2012) A greenhouse type solar dryer for small-scale dried food industries: development and dissemination. *Int J Energy Environ*;3(3):383–98
- [47] Janjai S, Khamvongsa V, Bala BK. (2007) Development, design, and performance of a PV-ventilated greenhouse dryer. *Int Energy J*;8:4
- [48] Janjai S, Srisittipokakun N, Bala BK. (2008). Experimental and modelling performance of a roof – integrated solar drying system for drying herbs and spices. *Energy*;33:91–3
- [49] Janjai S, Lamlert N, Intawee P, Mahayothee B, Bala BK, Nagle M, Muller J. (2009). Experimental and simulated performance of a PV-ventilated solar greenhouse dryer for drying of peeled longan and banana. *Sol Energy*;83:1550–65
- [50] Rathore NS, Panwar NL. (2010) Experimental studies on hemi cylindrical walk-in type

- [51] Saravanapriya, G., Mahendiran R. Design and Development of Solar Tunnel Dryer with Control System For Large Scale Drying of Agro Products. International Journal of Agriculture Sciences ISSN: 0975-3710&E-ISSN: 0975-9107, Volume 9, Issue 40, 2017, pp.-4626-4631.
- [52] Garg, H.P. and Kumar R. (2000) Renewable Energy, 13(3), 393 – 400.
- [53] Kalogirou, S.A. Solar thermal collectors and applications. Prog. Energy Combust. Sci. 2004, 30, 231–295.
- [54] Duffie, J. A. Beckman, W. A. Solar Engineering of Thermal Processes, Fourth Edi. New York: Wiley.
- [55] Yen, H. P., Duong, Nhan T.Vo, Phung T. K Le, Viet T. Tran, Three-Dimensional Simulation of Solar Greenhouse Dryer *VOL. 83, 2021* ISBN 978-88-95608-81-5; ISSN 2283-9216
- [56] Lelise, T.D., Werner, H., Albert, E., Oliver, H. Experimental evaluation of drying kinetics of tomato (*Lycopersicum Esculentum L.*) slices in twin layer solar tunnel dryer. Energy for Sustainable Development. 61 (2021) 241-250.
- [57] Sekhar, Y.R., Pandey, A.K., Mahbubul, I.M., Sai Avinash, G.R., Venkat, V., Pochont, N.R. Experimental study on drying kinetics for zingiber officinale using solar tunnel dryer with thermal energy storage. <https://doi.org/10.1016/j.solener.2021.08.011>.

APPENDIX

ANNEX A: MATLAB PROGRAM CODE

ANNEX (A-1): Transient Analysis of SAH

```

%%%%%%%%%%%%%%%%%%%%%%%%%%%%%%%%%%%%%%%%%%%%%%%%%%%%%%%%%%%%%%%%%%%%%%%%
% Hourly Temperature variation of air stream for Solar Heater
% Given Radiation and ambient temperature values for a year
% Consider a single glass cover and absorber plate
% Design Parameters %
Ac=10.0;           %Collector Area [ m2 ]   [L = 2 m, W=1 m]
P=8.0;            %Collector Perimeter [ m ]
tbe=0.03;         %Back Insulation Thickness [ m ]
te=0.03;          %Edge Insulation Thickness [ m ]
de=0.05;          %Depth of Edge [ m ]
Ep=0.10;          %Emissivity of Plate
Eg=0.88;          %Emissivity of Glass
L=2;              %Length of Collector [ m ]
Ki=0.035;         %Thermal Conductivity of Insulation [ W/m2 K ]
rho=0.2;          %Ground Reflectivity Factor
cpa=1000;         %Heat Capacity of Air [ J/kg K ]
Ka=0.0257;        %Thermal Conductivity of Air [ W/m2 K ]
mue=1.81e-5;      %Dynamic Viscosity of Air [ kg/m s ]
Adens=1.2;        %Density of Air [kg/m^3]
sigma=5.67e-8;    %Boltzmann Constant [ W/m2 K4 ]
Pabso=0.95;       %Absorptivity of Plate
Aabso=0.01;       % Absorptivity of Air
Gtrans=0.96;      %Transmissivity of Glass
S12=0.025;        %Distance b/n Glass and Plate [ m ]
mcpp=16500;       %Mass * Specific Heat of Plate [ J/K ]
mcpa=10050;       %Mass * Specific Heat of Air [ J/K ]
mcpg=18200;       %Mass * Specific Heat of glass [ J/K ]
mac=1.3572;       %Mass Flow Rate of Air [ Kg/s ]
Vw=3.5;           %Wind speed [ m/s2 ]
beta=pi/12;       %Collector slope (south facing) [ rad ]
phi=-26*pi/180;   %Latitude of Maputo [ rad ]

%%%%%%%%%%%%%%%%%%%%%%%%%%%%%%%%%%%%%%%%%%%%%%%%%%%%%%%%%%%%%%%%%%%%%%%%

% Simulation Initialization
Ta0=10.0+273;     %Initial Ambient Temperature [ K ]
Taoi=Ta0;         %Initial Inlet Air Temperature [ K ]
Tg0=Ta0+0.25;    %Initial glass temperature [ K ]
Tp0=Ta0+1.0;     %Initial plate temperature [ K ]
Tao0=Ta0+0.5;    %Initial Air Temperature at Exit [ K ]
deltt=60;         %Time Step
Al=2*L*de;       %Collector Perimeter*Depth of the Edge [ m2 ]
Upab=Ki/tbe;     %Bottom Heat Transfer Coefficient [ W/m2K ]
Upae=Upab*(Al/Ac); %Edge Heat Transfer Coefficient [ W/m2K ]
hc=2.8+3*Vw;     %Convective Heat Transfer b/n Glass and Ambient [ W/m2K ]
Adens=1.226;     %Density of Air [ Kg/m3 ]
nue=mue/Adens;   %Kinematic Viscosity of Air [ m2/s ]
Pr=0.7;          %Prandtl Number Taken at the Initial Condition

```

```

%%%%%%%%%%%%%%%%%%%%%%%%%%%%%%%%%%%%%%%%%%%%%%%%%%%%%%%%%%%%%%%%%%%%%%%%
% Solar Radiation Input
load SolDat.m;
data1=zeros(24,3);
for j=1:365
    data1(:,j)=SolDat(j+(23*(j-1)):j*24,:);
end
%%%%%%%%%%%%%%%%%%%%%%%%%%%%%%%%%%%%%%%%%%%%%%%%%%%%%%%%%%%%%%%%%%%%%%%%
% Sun Basic Angles
% Declination Angle(Deltt)of the sun every day over the year
for j=1:365
    decl(j)=(pi/180)*(23.45*sin((2*pi/365)*(284+j)));
end
% Calculation of the hour angle for each hour of the day.
for i=1:24
    omega(i)=(i-12)*pi/12;
end
% Incidence angle of the sun every hour and day of the year
IA=((cos(phi)*cos(beta)+(sin(phi)*sin(beta))*cos(decl(j))*...
    cos(omega(i)))+(sin(decl(j))*(sin(phi)*cos(beta)-...
    (sin(beta)*cos(phi)))));
% Zenith angle of the sun every hour and day of the year
ZA=(cos(phi)*cos(decl(j))*cos(omega(i)))+(sin(decl(j))*sin(phi));
%%%%%%%%%%%%%%%%%%%%%%%%%%%%%%%%%%%%%%%%%%%%%%%%%%%%%%%%%%%%%%%%%%%%%%%%
%This approximates the plate, glass, and exit temperature
for i=1:365
    Grr=data1(:,1,i);
    Drr=data1(:,2,i);
    Taa=data1(:,3,i);
    for j=1:24
        Gr=Grr(1);
        Dr=Drr(2);
        T=Taa(3);
        Ta=T+273;
        Ta0=Ta;
        Ta0i=Ta0;
        Tg0=Ta0+0.25; %Initial glass temperature [ K ]
        Tp0=Ta0+1.0; %Initial plate temperature [ K ]
        Tao0=Ta0+0.5; %Initial air temperature at exit [ K ]
        Rb=((cos(phi+beta))*cos(decl(i))*cos(omega(j)))+(sin(decl...
            (i))*sin(phi-beta))/((cos(phi)*cos(decl(i))*cos(omega(j))...
            +(cos(phi)*cos(decl(i))*cos(omega(j))+sin(decl(i))*sin(phi)));
        In=Rb*(Gr-Dr)+(Dr*0.5*(1+cos(beta)))+(0.5*rho*(1-cos(beta))*Gr);
        Ic=In*(Pabso*Gtrans);
        Tf=(Tao0+Ta0)/2;
        Vbeta=2/(Tao0+Ta0);
        GrL=(9.81*Vbeta*abs(Tp0-Tg0)*(S12^3))/(nue^2);
        Ua=0.664*(Ka/S12)*((Pr*GrL*cos(beta))/(Pr+0.9524))^0.25;
        Upg=((0.06-(0.017*(2*beta/pi)))*(Ka/S12)*(GrL^(1/3)))+(Epg*sigma*...
            ((Tp0^2)+(Tg0^2))*((Tp0)+(Tg0)));
        Tsky=Ta0+6;
        hr=Eg*sigma*((Tg0^4)-(Tsky^4))/(Tg0-Tsky);
        Uga=hc+hr;
        UL=6;
    end
end

```

```

%Plate Temperature
    Tp1=(deltt*Ac*Ic/mcpp)+(Tp0)-((deltt*Ac*Upg/mcpp)*(Tp0-Tg0))-
        ((deltt*Ac*Ua/mcpp)*((Tp0)-((Taoi+Tao0)/2)))-...
        ((Ac*Upab/mcpp)*(Tp0-Ta0)*deltt)-((Al*.5*Upae/mcpp)*(Tp0-
            Ta0)*deltt);
%Exit Air Temperature
    Ta01=(deltt*Ac*Ic/mcpa*Aabso)+(1-((deltt/(2*mcpa))*((Ac*Ua)+
        (mac*cpa))))*(Tao0)+(((deltt/(2*mcpa))*((mac*cpa)-(Ac*Ua)))
        *(Taoi))+(((Ac*Ua*deltt*(Tp0))/(mcpa)));
%Glass Temperature
    Tg1=((deltt*Ac*In*(1-Gtrans))/mcpg)+((1-((deltt/mcpg)*
        (Ac*Upg+Ac*Uga)))*(Tg0))+((deltt*Ac*Upg/mcpg)
        *(Tp0))+((Ac*Uga/mcpg)*deltt*(Ta0));
end
end
=====Main Program=====
% Average Temperature Initialization
Tp0=(Tp1+Tp0)/2;
Tg0=(Tg1+Tg0)/2;
Tao0=(Tao1+Tao0)/2;
%This approximates the plate, glass, and exit temperature
for i=1:365
    Grr=data1(:,1,i);
    Drr=data1(:,2,i);
    Taa=data1(:,3,i);
    for j=1:24
        Gr=Grr(j);
        Dr=Drr(j);
        T=Taa(j);
        Ta=T+273;
        Ta0=Ta;
        Rb=((cos(phi-beta))*cos(decl(i))*cos(omega(j)))+
            ((sin(decl(i))*sin(phi-beta)))/((cos(phi)*
                cos(decl(i))*cos(omega(j)))+(sin(decl(i))*sin(phi)));
        In=Rb*(Gr-Dr)+(Dr*.5*(1+cos(beta)))+(0.5*rho*((1-cos(beta))*Gr));
        Ic=In*(Pabso*Gtrans);
        for jj=1:10000 % Total Number of Iteration
            Tf=(Tao0+Ta0)/2;
            Vbeta=2/(Tao0+Ta0);
            GrL=(9.81*Vbeta*abs(Tp0-Tg0)*(S12^3))/(nue^2);
            Ua=0.664*(Ka/S12)*((Pr*GrL*cos(beta))/(Pr+0.9524))^0.25;
            Upg=((0.06-(0.017*(2*beta/pi)))*(Ka/S12)*(GrL^(1/3)))+
                (Epg*sigma*((Tp0)^2+((Tg0)^2))*((Tp0)+(Tg0)));
            Tsky=Ta0+6;
            hr=Eg*sigma*((Tg0)^4-((Tsky)^4))/(Tg0-Tsky);
            Uga=(hc+hr);
            UL=6;
        %Plate Temperature
            Tp1=(deltt*Ac*Ic/mcpp)+(Tp0)-((deltt*Ac*Upg/mcpp)*(Tp0-Tg0))-
                ((deltt*Ac*Ua/mcpp)*((Tp0)-((Taoi+Tao0)/2)))-...
                ((Ac*Upab/mcpp)*(Tp0-Ta0)*deltt)-((Al*.5*Upae/mcpp)*(Tp0-
                    Ta0)*deltt);
        %Exit Air Temperature
            Ta01=(deltt*Ac*Ic/mcpa*Aabso)+(1-((deltt/(2*mcpa))*((Ac*Ua)+
                (mac*cpa))))*(Tao0)+(((deltt/(2*mcpa))*((mac*cpa)-(Ac*Ua)))
                *(Taoi))+(((Ac*Ua*deltt*(Tp0))/(mcpa)));
        end
    end
end

```

```

%Glass Temperature
    Tg1= ((deltt*Ac*In*(1-Gtrans))/mcpG)+(1-((deltt/mcpG)*(
        Ac*UpG+Ac*Uga)))*(Tg0))+((deltt*Ac*UpG/mcpG)
        *(Tp0))+((Ac*Uga/mcpG)*deltt*(Ta0));
    Tp0=Tp1; Tg0=Tg1; Ta00=Ta01;
    end
% The daily plate, glass and exit air temperature of the year are stored as;
    Tp11(j,i)=Tp1-273; Tg11(j,i)=Tg1-273; Ta011(j,i)=Ta01-273;
    end
end
% This stores for the selected day for plotting.
Ta01Jan17=Ta011(:,1);Ta01Feb16=Ta011(:,2);Ta01Mar16=Ta011(:,3);
Ta01Apr15=Ta011(:,4);Ta01May15=Ta011(:,5);Ta01Jun11=Ta011(:,6);
Ta01Jul17=Ta011(:,7);Ta01Aug16=Ta011(:,8);Ta01Sep15=Ta011(:,9);
Ta01Oct15=Ta011(:,10);Ta01Nov14=Ta011(:,11);Ta01Dec10=Ta011(:,12);
% hours of the Day
jj=1:24;
% Plots exit air stream temperature for Jan - Mar
plot(jj,Ta01Jan17,'r--',jj,Ta01Feb16,'k-*',jj,Ta01Mar16,'g-^','linewidth',2)
xlabel('Time in hours','fontsize',12)
ylabel('Temperature in Degree Celcius','fontsize',12)
title('Hourly Exit Air Temperature Variation','fontsize',12)
legend('Jan','Feb','Mar')
grid on
pause
clf
% Plots exit air stream temperature for Apr - Jun
plot(jj,Ta01Apr15,'r--',jj,Ta01May15,'k-*',jj,Ta01Jun11,'g-^','linewidth',2)
xlabel('Time in hours','fontsize',12)
ylabel('Temperature in Degree Celcius','fontsize',12)
title('Hourly Exit Air Temperature Variation','fontsize',12)
legend('Apr','May','Jun')
grid on
pause
clf
% Plots exit air stream temperature for Jul - Sep
plot(jj,Ta01Jul17,'r--',jj,Ta01Aug16,'k-*',jj,Ta01Sep15,'g-^','linewidth',2)
xlabel('Time in hours','fontsize',12)
ylabel('Temperature in Degree Celcius','fontsize',12)
title('Hourly Exit Air Temperature Variation','fontsize',12)
legend('Jul','Aug','Sep')
grid on
pause
clf
% Plots exit air stream temperature for Oct - Dec
plot(jj,Ta01Oct15,'r--',jj,Ta01Nov14,'k-*',jj,Ta01Dec10,'g-', 'linewidth',2)
xlabel('Time in hours','fontsize',12)
ylabel('Temperature in Degree Celcius','fontsize',12)
title('Hourly Exit Air Temperature Variation','fontsize',12)
legend('Oct','Nov','Dec')
grid on
pause
clf

```

ANNEX B: PROPERTIES OF VARIOUS MATERIALS
Table (B-1): Thermal Conductivities of Absorber Materials

		Properties at 300 K				Property of K/C_p [W/Km]/[J/KgK]
Substance	Melting point[K]	ρ [Kg/m ³]	C_p [J/KgK]	K [W/Km]	$\alpha * 10^6$ [m ² /s]	At 400 K
Copper	1358	8933	385	401	117	393
Aluminium	933	2702	903	237	97.1	240
Mild Steel	1810	7832	434	63.9	18.8	58.7
Stainless steel	1670	7913	477	14.6	3.95	16.6
Lead	601	11,340	129	35.3	24.1	34
Nickel	1728	8900	444	90.7	23	80
Iron	1810	7870	447	80.2	23.1	69.5

Table (B-2): Properties of Cover Materials

Material	Transmittance (τ)	Absorption (α)	Emissivity (ϵ)
Crystal Glass	0.91	0.04	0.05
Window Glass	0.85	0.06	0.09
Polyamide	0.8	0.08	0.14
Low Iron Tempered Glass	0.94	0.02	0.04
Polyethylene	0.80	0.01	0.94
Polyvinyl fluoride	0.93	0.04	0.03
Fluorinated	0.96	0.03	0.01
Polymethyl	0.89	0.05	0.06

Table (B-3): Properties of Sealing Materials

Material	Working temp. Range (° c)		Elongation To Failure (%)	Resistance to Compression Set	Resistance to Creep	Resistance to Weather	Resistance to Water
	Min	Max					
Acrylic	-40	130	400	3	2	4	1
Butyl	-50	125	800	2 – 3	2	4	2 – 4
EPDM	-40	150	600	3 – 4	2	4	4
Fluroelastomers	-40	230	300	3 – 4	3	4	4

Silicone	-60	230	700	2 – 4	3	4	3 – 4
Urethanes	-50	100	700	1 – 4	3	4	1 – 2
(4=excellent, 3=good, 2=fair, 1=poor)							

Table (B-4): Properties of Insulation Materials

Materials	$K @ 25\text{ }^{\circ}\text{C}$ [W/Km]	Maximum Service Temperature ($^{\circ}\text{C}$)	ρ [Kg/m ³]	C_p [J/KgK]
Glass Fiber	0.032	343	56 – 72	38 – 39
Mineral Fiber	0.036 - 0.055	649 – 1037	4.8 - 32	710 – 960
Calcium Silicate	0.055 (@90°C)	649	2330	712
Perlite	0.048	816	16	1260
Foamed Glass	0.058	565	144	1000
Polystyrene Foam	0.029 - 0.039	74	16	1200
Polyurethane Foam	0.023	104	24 – 40	1600
Isocyanurate Foam	0.025	121	70	1045
Phenolic Foam	0.033	135	136	1000
Cellular Plastic	0.040	100	37 – 51	39 – 46

Table (B-5): Lists Properties of Some Selective Coatings

Coating	Type	Absorbance (α)	Emissivity (ϵ)
Black Chrome	Electroplated	0.96	0.10
Black Nickel	Electroplated	0.9	0.1
Black Copper	Copper oxide	0.87-0.92	0.07-0.35
Black Anodize	Aluminium oxide	0.94	0.07
Solar Foil	Black chrome over copper	0.96	0.10
Enersorb*	Urethane paint	0.97	0.90
Nextel*	Paint	0.98	0.89
* Non-Selective			

ANNEX C: VERDE AFRICA LDA BRIQUETTE PRODUCT



Figure (C-1): Charcoal Dust Briquette of Verde Africa Lda

ANNEX D: PSYCHROMETRIC CHART

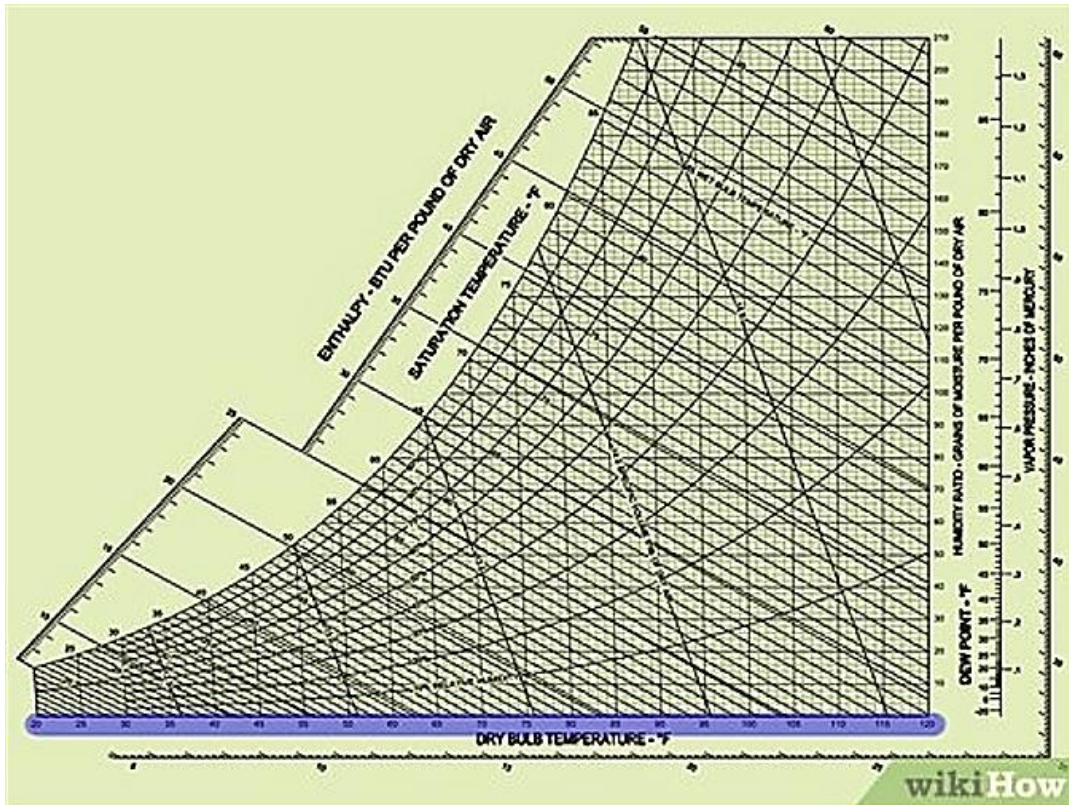


Figure (D-1): Psychrometric Chart